OPTICAL NEAR-FIELD ENHANCEMENT BY MICRO/NANO PARTICLES FOR NANOTECHNOLOGY APPLICATIONS

ZHOU YI

NATIONAL UNIVERSITY *of* SINGAPORE

2008

OPTICAL NEAR-FIELD ENHANCEMENT BY MICRO/NANO PARTICLES FOR

NANOTECHNOLOGY APPLICATIONS

BY

ZHOU YI (M. Eng)

Huazhong University of Science & Technology, Wuhan, China

A DISSERTATION SUBMITTED IN PARTIAL FULFILMENT

OF THE REQUIREMENT FOR THE DEGREE OF

DOCTOR OF PHILOSOPHY OF ENGINEERING

NATIONAL UNIVERSITY *of* SINGAPORE

2008

Acknowledgements

At first and most importantly, I would like to express my heartfelt appreciation and gratitude to my supervisors, Prof. Jerry Fuh, Prof. Lu Li and A/Prof. Hong Minghui for their invaluable guidance and great support throughout every stage of my research. A/Prof. Hong's acute sense in most recent development trends of nanotechnology and near-field optics science, and the patience and diligence in research work give me deep impression.

I am grateful to Prof. Boris Luk'yanchuk for his help in theoretical calculation for near-field problems. I learned a lot from him in mathematics and optics. A special thank goes to Dr. Wang Zengbo and Dr. Wang Haifeng for discussions and advices on theoretical calculation. Thanks Dr. Chen Guoxin for his assistance in experiments and taking AFM measurements. Members in Laser Laboratory, including Dr. Lin Ying, Mr. Lim Chin Seong, Ms. Doris Ng had helpful discussions with me during the research. Other research staffs and scholars in Data Storage Institute also shared their experience kindly during the past years.

Lastly, I deeply appreciate my parents, my wife and son for their cares and supports.

Table of Contents

Summary

Near-field optics (NFO) deals with optical phenomena involving evanescent wave which becomes significant when the sizes of the objects are in the order of wavelength or even smaller. Since this special electromagnetic wave makes diffraction limit less restrictive, it confines light in a volume sufficiently small for the nanotechnology applications. The future of NFO would be seen in extensions of integrated optics towards the nanoscale.

This thesis aims to understand several NFO fundamental issues. These problems are related to the optical near-field induced by small particles under laser irradiation: (1) optical resonance (Sphere Cavity Resonance) and near-field enhancement effects of dielectric particles for laser cleaning/nanopatterning applications, and (2) plasmonic resonance by metallic nanoparticles.

In the studies, nanopatterning beyond diffraction limit on transparent substrates was demonstrated by 800 nm /100 fs femtosecond laser irradiation of self-assembled micro-silica particles array. No cracks were found at edges of produced nanostructures on the glass surface due to two-temperature non-equilibrium state. At a low laser fluence, the nanostructure feature sizes were found from 200 to 300 nm with the average depth of 150 nm. Tri-hole structure was created when laser fluence is higher than 43.8 J/cm^2.

Mie theory calculation shows that for 1 μm particle, the focusing point is inside the particle which results in the explosion of microparticles and the formation of debris. While,

increasing the particle size, the focusing point can be outside of microparticles. Experimentally using 6.84 μm particles, these particles are in their integrity which verifies that the position of focusing point depends on particle size. For most cases, the experimental results are in good agreement with Mie theory simulation results.

Plasmonic resonance enhanced absorption of laser energy by metallic spherical nanoparticles was discussed. Calculations of the cross section efficiencies of 40 nm Au nanoparticles predict that at the resonance frequency, the absorption is the strongest, as verified experimentally.

In the dry laser cleaning, field enhancement and its consequences play major roles. For transparent particle and normal incidence, the near-field enhanced field near the centre produces a cylindrical convergent surface acoustic wave, which benefits the particle removal for sufficiently "big" particles (above 2 μm).

For metallic nanoparticles, the laser intensity under the particle typically diminishes, in contrast to transparent particles, which act as a near-field lens. Nevertheless, with light frequencies near surface plasmon resonance, the conditions for the efficient coupling of the light with metallic surface can be provided. This plasmonic effect can help clean metallic nanoparticles from metallic surface. The ability to clean 40 nm gold particles from the Si substrate was experimentally demonstrated.

List of Tables

List of Figures

List of Symbols

$\mathbf{E}$	Electric field	k	Wave vector
${}^{e}D$	Electrical Debye potential	$\mathbf{H}$	Magnetic field
ω	Angular frequency	${}^{h}D$	Magnetic Debye potential
ε_m	Dielectric permittivity of medium	ω_p	Plasma frequency
μ_m	Magnetic permeability of medium	ε_p	Dielectric permittivity of particle
λ	Laser wavelength	μ_p	Magnetic permeability of particle
$\boldsymbol{S}$	Ponyting vector	q	Size parameter
κ	Absorptive index; heat conductivity	n	Reflective index
I	Laser intensity	a	Radius of particle
Q_{sca}	Scattering coefficient	S_0	Enhancement factor at particle-substrate contacting point.
ρ	density; electron density	Q_{ext}	Extinction coefficient
T	temperature	Q_{abs}	Absorption coefficient
α	Incidence angle; absorption coefficient	c	Heat capacity; light speed
τ	electron relaxation time	t	time
γ_0	electron relaxation rate	m_e	free-electron mass
I_0	input laser intensity	A	particle geometrical cross section
ε'	real part of permittivity	ε''	image part of permittivity
v_F	Fermi velocity	p	pressure
$C_{t,l,R}$	propagation velocity of transverse, longitudinal and Rayleigh waves		

Chapter 1 Introduction

1.1 Introduction to near-field optics

In general, a near-field is referred to a region with distance in micro/nano scales. Near-field optics (NFO) deals with phenomena involving evanescent electromagnetic waves. This special electromagnetic wave becomes significant when the size of an object is in the order of incident wavelength or even smaller [3], where so-called Mie resonance or morphological resonance become important [4]. Nowadays, theory of electromagnetic waves describes satisfactorily their interactions with objects which are macroscopic relative to the incident wavelength. However, the theoretical knowledge about the scattering of electromagnetic waves by micro/nano-systems remains limited. Most approximations are not appropriate to study micro/nano-systems. These systems require the detail solutions of the full set of Maxwell equations. The main origin of these problems can be back to the crucial role played by the evanescent components of the field in the near-field zone close to micro/nano-particles.

According to Diao et al. [5], the optical scattering of a small particle can be classified into two categories: (1) sphere cavity resonance (SCR) in a dielectric particle and (2) plasmon resonance (PR) in a metal particle. Plasmons are defined as electromagnetic excitations coupled to the free charges of a conductive medium. In modeling, both SCR and PR can be satisfactorily described by Mie theory [6], which is an exact solution of Maxwell equations for an arbitrary sphere under the plane wave excitation.

Theoretically, the SCR resonance is very sharp. It means that the optical resonance produces high intensities in the near-field region and, naturally, it can lead to the formation of "hot points". Clearly, these "hot points" influence the laser cleaning efficiency and are responsible for surface nanostructuring applications as well.

Meanwhile, it is well known that a small metal particle, such as gold and silver nanoparticles, under direct laser irradiation can excite localized plasmonic effect [7], which is collective oscillations of free electrons confined inside the particles. These are two possible reasons why plasmonics is hot in recent years: (1) People cannot completely understand all the aspects of plasmonic effect. In other words, a large amount of unknown issues exist in the field, and (2) the promising applications in nanopatterning which can improve data storage density and in nanostructure characterization which can achieve the observation under molecular range.

1.2 Literature review

1.2.1 Overview of Mie theory

In a paper published in 1908, G Mie [6] obtained, on the basis of the electromagnetic theory, a rigorous solution for the diffraction of a plane monochromatic wave by a homogeneous sphere of any diameter and of any composition situated in a homogeneous medium. Mie theory is a separation of variables approach which gives an analytical equation for the Mie coefficients. The interesting early history of light scattering was

reviewed by Logan [8].

The optical scattering of a small particle can be classified into two categories: (1) sphere cavity resonance (SCR) in a dielectric particle and (2) plasmon resonance (PR) in a metal particle [5]. It is known for more than 50 years that the optical resonance is responsible to the ripple structure of the extinction [9]. The first analysis of the optical resonance was carried out with respect to conventional applications in colloid and aerosol physics. The new interest to optical resonance arises due to the studies of resonance phenomena in radiation pressure [10], optical levitation [11] and long-wave optical spectrum in ionic crystals. Traditionally, optical resonance is inspected in the far field by spectroscopic techniques, e.g. absorption/extinction spectra measurement [12], in which the electromagnetic field is dominated by the propagating mode. On the contrary, the peculiarities of the laser cleaning/nanopatterning problems are related to the near-field region where the evanescent wave is dominant instead of propagating wave [13, 14].

In sphere cavity resonance (SCR), the incident field excites resonance but undamped modes in dielectric spheres are distributed as evanescent waves around the sphere. In the near-field region of the sphere cavity, the field distribution is dominant with these evanescent waves, and is sensitive to the size parameter of the sphere. The SCR resonances are very sharp, and the efficient divergence of radiation for corresponding modes is very small. It means that optical resonance produces high intensities in the near-field region and, naturally, it can lead to the formation of “hot points”. In contrast to SCR, PR mode in a metal sphere is generated due to the oscillation of free electrons inside.

These PR modes are damping modes due to the high dissipative factor of metals.

Both SCR and PR can be satisfactorily described by Mie theory in modeling. The geometrical optics (for big particle with $a >> \lambda$) and dipole approximation (for small particle with $a << \lambda$) can be regarded as the two limiting cases of Mie theory. In near-field optics (NFO) where micrometer size particles are concerned, the simulation by dipole approximation could lead to inaccurate results due to the excitation of higher-order multipole resonance modes in particles. It needs detail theoretical analyses with sufficient number of mode terms. The inclusion of a small term in Mie series beyond dipole approximation could significantly distort the phase portrait of optical near field and produce a completely different near-field distribution.

The solution due to Mie theory, though derived for diffraction by a single sphere, also applies to diffraction by any number of spheres, provided that they are all of the same diameter and composition and provided also that they are randomly distributed and separated from each other at a distance that is large compared to the wavelength. Under these circumstances, there are no coherent phase relationships among the lights scattered by different spheres. The total scattered energy equals to the energy scattered by one sphere multiplying the total number of spheres. It is particularly in the connection that Mie solution is of great practical value and may be applied to a variety of problems: in addition to the question of colors exhibited by metallic suspensions. We may mention applications, such as the study of atmospheric dust [15], interstellar particles or colloidal suspensions [16], the theory of the rainbow, the solar corona, the effects of clouds and fogs on the

transmission of light [17].

Although the light scattering and absorption by a spherical particle (with any size and optical dielectric constant) were solved in 1908 by Mie, this theory (together with many of its extended theories) still remains its invaluable contributions today, especially in the NFO. In micro/nano-regions, most research interests in NFO could be approximately modeled by small particles, such as colloid, sharp tip, single molecule and bio-virus. The near field enhancement around such sub-micron particles is of immediate relevance to near-field optics microscopes [18] or, to some extent, pointed tips [19]. In the near field, for sufficiently small particles, only the lowest order solution, equivalent to dipole excitation, is of significance. The scattering efficiency is proportional to $(\varepsilon_p - \varepsilon_m)/(\varepsilon_p + 2\varepsilon_m)$ in this case, where $\varepsilon_p, \varepsilon_m$ are the dielectric constants of the particle and the surrounding medium, respectively.

1.2.2 Extensions of Mie theory

As Mie theory is restricted to spherical homogeneous spheres, there are many extensions of this theory covering different aspects. Some relevant aspects will be described in the following.

Shortly after Mie, P. Debye [20] published a paper concerned with light pressure induced by irradiation of particles, i.e. the mechanical force exerted by light, on a conducting sphere, the subject has been treated in different aspects by many researchers [21,22]. The plasmon resonance based optical trapping method is used to achieve stable

trapping of metallic nanoparticles. In all cases, the longitudinal plasmon mode of these anisotropic particles is used to enhance the gradient force of an optical trap, thereby increasing the strength of the trap potential [23]. While for this plasmonic effect, it can be readily extended from the Mie scattering theory. For small particles, the divergence in scattering efficiency at $\varepsilon_p + 2\varepsilon_m = 0$ is the condition for the lowest order plasmonic resonance. Upon approach if a third medium, ε_m becomes a weighted average of the dielectric constants of the second and the third medium. This modifies the resonance conditions, as a function of distance between the particle and the third medium [24]. An advanced algorithm was given by Toon and Ackerman [25]. An algorithm for a sphere with two coatings was given by Kaiser [26]. This has been used to compute the internal field of a particle at resonance. Such algorithms may help in identifying water droplets collecting dust or soot on the outer surface [27].

The electromagnetic Green's tensor approach is used to obtain the differential and total scattering cross sections of a finite size nanoparticle located at a metal surface [28]. The scattering process comprehends either elastic scattering of the incident surface plasmon into other surface plasmon propagating in different directions or scattering into field components propagating away from the surface, as well as the irradiation absorption by the meal nanoparticle. A scattering theory for magnetic spheres can easily be formulated [29]. This may be relevant for scattering at infra-red or microwave frequencies. The scattering theory of coated dielectric spheres was first derived by Aden and Kerker [29].

The scattering of light by particles of shapes other than spheres has been considered by

some authors [30,31], but in general the analytical properties of the corresponding wave functions are much more complicated, so that rigorous solutions are of limited practical value [32]. Gans [33] and other workers discussed the scattering of electromagnetic wave by ellipsoids with dimensions smaller compared to the wavelength; a rigorous solution for an ellipsoid of arbitrary size has been published by Moglich [34]. The scattering from long circular conducting cylinders was studied as early as 1905 by Seitz [35] and Ignatowsky [36]. The formulae obtained are similar to those of Mie relating to the sphere.

Another derivation from a Mie sphere is a just slightly non-spherical particle. This may be treated by a first-order perturbation approach [37]. In this case, the assumptions are: (1) the particle is homogeneous and (2) the deviations from sphericity are small and smooth, such as a droplet distorted by a fluid flow. There is also an extension of Mie theory to an anisotropic spherical shell [38] which is an appropriate model to study light scattering by a variety of biological systems.

Since metallic spheres are all absorptive materials, the calculations related are much more laborious and only a few special cases have been studied in detail. For larger spheres, asymptotic formulae due to Jobst [39], based on Mie's theory and Debye's asymptotic expansions of the cylinder functions may be used for calculation. Weakly absorbing spheres was studied by van de Hulst [40]. In the latter case, the general behaviors of the extinction curves are seen to be similar to those of dielectric spheres, but even a very small conductivity is sufficient to smooth out the small undulations completely. As the conductivity is increased further, the first minimum disappears altogether and the

extinction curve rises asymptotically from the origin to twice of this value. The absorption curves rise asymptotically from the origin to half of this value.

A number of theoretical groups began to work on the determination of exact near-field optical field distributions in 1990s [41, 42]. The task involves massive numerical computation and is the only way to gain deep insight into the peculiarities of optical near fields, in particular about their confinement and enhancement by spheres. Jaffe developed a creative algorithm to inversely calculate the internal electromagnetic field of a homogeneous sphere from the observation of its scattered light field [43]. There is a simple Fourier relationship between a component of the internal E-field and the scattered light in a preferred plane. The estimated values are shown to be accurate in the presence of moderate noise for a class of size parameters.

1.2.3 Experimental researches on Mie and its extended theory

1.2.3.1 Particles scattering

Mie theory may be tested experimentally by means of observations of light scattered either by a single spherical particle, or by many particles (cloudy media, colloidal solutions). Such tests may be carried out with relative ease when the particles are large, but are rather troublesome when the diameter of each particle is of the order of a wavelength or smaller. La Mer and collaborators [44, 45] succeeded in testing the theory from measurements of the angular distribution of scattered light as well as the total scattering from sulfur sols in water, of particle diameter from 300 nm to 500 nm. Light of

vacuum wavelengths in the range from 285 nm to 1000 nm was used and a fair agreement with the predictions of Mie theory was found.

Compared with dielectric particles, metallic nanoparticles exhibit promising properties for nanotechnology applications. Of the early workers who studied the optical properties of metallic particles, mention must be made of Maxwell Garnett [46]. He considered the passage of light through a dielectric medium containing many small metallic spheres in a volume of linear dimensions of a wavelength. With the help of the Lorentz-lorenz formula, Maxwell Garnett showed that such an assembly is equivalent to a medium of a certain complex refractive index $n_c = n + i\kappa$ and he found formula for n and κ in terms of the indices that characterize the metallic spheres. By means of these considerations, he was able to account for some of the observed features.

Metal nanoparticles find applications in numerous areas of science and technology, ranging from medicine to optics and biological labeling and imaging [47]. For example, silver and gold were used to enhance the non-linearities of molecular probes that are potentially useful for selectively imaging the structure and physiology of nanometric regions in cellular systems [48]. Magnetic metal nanoparticle that is critical to magnetic recording industry is an important class of metal nanoparticles. Co, Fe and Ni [49,50] nanoparticles can be made in with disk or rod shapes that can be used for magnetic recording applications.

In the mid-1970s, opticians were surprised by the high intensity Raman scattering from certain adsorbates on rough surfaces of copper, silver, or gold nanostructures [51, 52]. It

was soon found that field enhancement by plasmonic excitation plays an important role. The plasmons are localized at small protrusions and crevices of the rough surface. An individual protrusion can be modeled as a semi-ellipsoid on a plane. Laplace's equation can be solved analytically for this geometry [53, 54]. As a general result, several plasmon resonances of approximately equal strength were found.

Another type of surface plasmon polariton can be realized by making use of individual metallic nanoparticles arranged to form various structures, such as linear chains or two dimensional arrays. The surface plasmon polariton propagation along metallic nanoparticles chain could be comprehended with the quench of fluorescence. The fluorescence of a molecule can be quenched by placing a second molecule in its immediate proximity, if the second molecule absorbs light at the emission frequency of the first molecule. The quenching increases with decreasing distance according to an inverse sixth order power law. The transfer of excitation can be studied quantitatively if the second molecule is also fluorescent. This is a typical near field effect based on the well known characteristics of dipole antennas. Gersten and Nitzan [55] and van Labeke et al. [56] extended the above energy transfer considerations to the case of a fluorescent molecule near a small metallic particle. The fluorescence properties were found to vary drastically from those of the free molecules. This was confirmed by Leitner et al. [57], who studied the fluorescence of dyes adsorbed small silver islands. Experimental studies [58, 59] showed that nanoparticle which ensembles on metal surfaces can be used to create efficient micro-optical components for surface plasmon polartons, such as mirrors, beam splitters, and interferometers. Furthermore, periodic arrays of metal surface nanoparticles

have been shown to exhibit band gap properties for the propagation of surface plasmon polaritons [60, 61]. If such a band gap structure has narrow channels free from particles, surface plasmon polariton can be confined to and guided along these channels [62,63].

Superposition of the electromagnetic fields of neighboring plasmonic excited particles results in considerable modification of the resonance conditions. This is readily noticed in the reflection and absorption spectra of granular gold and silver films [64, 65]. Array of regular small metal structures on a dielectric substrate provides even more detail information.

Finally, the non-radiative plasmon modes on a metallic surface can be converted to a radiation field – emitted light – with the aid of metallic nanoparticles [66]. This is a consequence of the direct coupling between light and plasmon mode allowed in the particle-surface system.

1.2.3.2 Micro/nano-particles nanopatterning

The current trend towards sub-wavelength structures creates a need for new methods and technologies for surface nanostructuring. In most near-field techniques, the sub-wavelength resolution is achieved by placing a small aperture between the recording medium and light source. If the aperture-to-medium separation is controlled at a distance much smaller than the wavelength, the resolution is determined by the aperture size instead of the diffraction limit [67]. However due to sophisticated hardwares to control the near-field distance and low throughout, this approach is difficult to be implemented in industrial applications. Using particle masks [68], in near field to pattern a solid

substrate is a promising approach that could lead to parallel nanostructuring beyond diffraction limit [69, 70].

Microsphere lattice monolayer has been used to generate patterns on a substrate by irradiation of a nanosecond infra-red plane-wave to create submicron features on a glass substrate [71, 72]. Selective removal of individual silica microspheres and how field enhancement effects can contribute to the accuracy and resolution of the process were demonstrated, where ultrashort pulses were used because of their ability to produce well localized changes with low pulse energies.

A novel photolithographyic technique using periodic hexagonal closely packed silver nanoparticles to form a 2-dimentional array photomask has been demonstrated to transfer a nano-pattern onto a photoresist [73]. This method can be used to precisely control the spacing between nanoparticles by temperature. The high density nanoparticle thin film is accomplished by self assembly through the Langmuir-Schaefer technique [74] on a water surface and then transferring the particle monolayer to a temperature sensitive polymer membrane. This technique uses a colloidal dispersion of nanoparticles in an organic liquid, which has a controlled convex curvature on a water surface. A monolayer of metal nanoparticles nucleates at the raised center of the water surface and grows smoothly outwards, as the liquid evaporates. By bringing a smooth substrate down to the nanoparticles film, the monolayer can be transferred.

The nanosphere lithography technique employs colloidal self-assembly of 700 nm glass nanospheres that form hexagonal closely packed monolayers on Si surfaces. Directional

evaporation through the holes between the nanospheres yields honeycomb nanodot patterns, while sputtering deposition through the nanospheres leads to a thin film mesh that acts as a mask during subsequent anisotropic etching, which results in an array of inverted pyramid holes [75].

The recycling of microparticles arrays was investigated by D. Bauerle [76] with a spacer. A thin Au film was coated on microparticles arrays and femtosecond laser was applied to fabricate nano-apertures which could be explained by electromagnetic field interferences caused by the array of microspheres [77, 78]. Potentially applied in industry, these microparticles array requires to be modified as multi-lens array [79, 80]. Then the mask can be employed to create nanopatterns on a large area substrate surface effectively.

Current day research in sub-50 nm metallic nanoparticles near-field optics is strongly influenced by the development of scanning near-field optical microscopy, also called near-field scanning optical microscopy. This is a super-resolution optical microscopy which has enabled a variety of novel plasmonic experiments. This super-resolution, however, is limited by the probe aperture size. Ruppin [81] and Royer et al. [82] studied the influence of a nearby dielectric medium on the plasmonic resonances of a metallic sphere. The resonance frequency and width depend on the properties of the medium in a sensitive way. This may become relevance to apertureless SNOM. Fischer probably was the first to recognize the potential of small light scattering particles and sharp tips for truly super resolution microscopy. Plasmonic excitation increases the sensitivity of the process. A scattering tip in fact is a valid alternative to the aperture probe in SNOM.

The future of near-field optics and plasmonics may also be seen in extensions of integrated optics towards the nanoscale. Techniques known from radio wave technology might be scaled down to submicron dimensions. The optical antenna, the metallic optical waveguide, and optical tweezers capable of manipulating nanoscopic particles may be among the fruits of such attempts. The increasing mastery of nanometer scale structuring techniques may, further, allow the development of plasmonic functional elements, such as mirrors, filters, diffraction gratings, and modulators. Implemented in thin film structures, these elements may open new perspectives for integrated optical devices.

1.3 Objectives and contributions

1.3.1 Objectives

Near-field optical resonance and plasmonic effect have been predicted theoretically for about 100 years, but the physics of evanescent electromagnetic waves, which is the key concept used in near-field optics, was a poorly developed research area before the mid-1960s. Even now the interactions between the wave and the materials are not understood clearly.

The demand of high capability data storage devices has led to the rapid development of precision engineering and nanotechnology. One challenge in this field is to overcome the optical diffraction limit. Meanwhile, near-field effect must be considered. This task is believed to be accomplished while a variety of studies need to be carried out to understand

the mechanisms behind.

The main objectives of the research are as follows:

- To understand near-field optical scattering by micro/nano-particles and apply Mie theory for numerical simulation;
- To understand plasmonic effect by metallic nanoparticle in near field;
- To explore near-field optics application in nanotechnology;
- To carry out investigation on the various phenomena in laser nanopatterning.

1.3.2 Research contributions

- The simulation of intensity distribution reveals details on how a small particle absorbs light energy and consequently releases absorbed energy.
- The influence of various factors, such as laser fluence, light wavelength, incident angle, and particle size.
- Developed a method to obtain small size patterns overcoming optical diffraction limit.
- Tri-hole structure formation under high fluence femtosecond laser illumination.
- Extraordinary scattering diagram for nanoparticles with theoretically extreme conditions.
- Laser dry cleaning of 40 nm Au particles.

1.4 Thesis outline

Chapter 2 includes mainly the basic Mie theory background and its exact solutions for single spherical particle in a homogeneous medium under a plane monochromatic wave. The calculated distributions of light intensity passing through dielectric and metallic particles are shown in the chapter. Drude model will be introduced to determine optical constants of metallic nanoparticles.

Chapter 3 shows the experimental details. Sample preparation, experimental setup, laser sources employed in the research and characterization techniques.

Chapter 4 provides the application of Mie theory in nanopatterning of silica and silicon substrates with the assistance of dielectric glass microparticles array by femtosecond laser irradiation. The theoretical explanation will cover the diffraction of laser beam based on Mie calculation, the absorption of femtosecond laser pulse and the influence of particle size parameter. An novel tri-hole structure was found in the research at a high laser fluence. The mechanism of formation will be discussed. In the later part of this chapter, nanopatterning under oblique incident light is described to have the deeper understanding of Mie theory.

The Mie theory in metallic nanoparticle is shown in chapter 5, where the research focus is plasmonic effect with Au particles. Both experimental and theoretical research results will be provided including scattering at plasmonic resonance frequency and off-resonance frequency. Some consequent discussions of extraordinary scattering issues for

nondissipative nanoparticles are presented at the last section of the chapter.

Chapter 6 presents the application of laser dry cleaning of 1 μm transparent particles and 40 nm Au nanoparticles. For different material properties, various laser wavelengths should be considered. Surface acoustic wave and plasmonic resonance enhanced absorption are believed to play important roles.

Chapter 7 concludes the whole research results. The possible future works are recommended.

Chapter 2 Near-field light scattering of small particle

The optical scattering of a small particle can be classified into two categories: (1) sphere cavity resonance (SCR) in a dielectric particle and (2) plasmon resonance (PR) in a metal particle. In modeling, both SCR and PR can be satisfactorily described by Mie theory. The solution of Maxwell's equations describes the field arising from a plane monochromatic wave incident upon a spherical surface, across which the properties of the medium change abruptly.

2.1 Model and assumptions

The light scattering by a small sphere was described by Mie theory [6]. A rectangular system of coordinates with origin at the centre of the sphere (z axis in the direction of wave propagation and x axis in the direction of its electric vector) was taken. The model in Fig. 2.1 considers the diffraction of a linearly polarized, monochromatic plane wave by a sphere of radius a which is immersed in a homogeneous and isotropic medium. The amplitude of the electric vector of the incident wave is normalized to unity, i.e. $\left|E^{(i)}\right| = 1$. The medium is assumed to be non-conductive and both the medium and the sphere are non-magnetic [9]. The time dependence of the involved fields can be assumed to be harmonic and more complicated time dependent fields can be written as superposition of the fields with Fourier synthesis.

The fields vectors both outside and inside the sphere satisfy Maxwell's equations without free charges.

$$\nabla \times H = -i\omega\varepsilon E, \qquad \nabla \times E = i\omega\mu H \tag{2.1}$$

where ω is angular frequency, ε permittivity, μ permeability, H magnetic field, and E electric field. The boundary conditions on the surface of sphere include continuity of tangential components of **E** and **H**, and radial components of **D** =ε **E** and **B** = μ **H**. Quantities which refer to the medium surrounding the sphere will be denoted by subscript *m*, those referring to the sphere by subscript *p*. As the medium surrounding the sphere is assumed to be non-conducting, $\sigma_m = 0$.

The first modern outline of the Mie theory in terms of spherical vector wave functions was given in the classical book by Stratton in 1941 [83]. Spherical coordinates are *r*, θ and φ, where θ is the azimuthal angle between the radius vector ***r*** and *z* axis, φ polar angle at *x*-*y* plane. In spherical polar coordinates, Maxwell equations together with the boundary conditions are separated into a set of ordinary differential equations, which are then solved for the two sub-fields in the form of infinite series. The boundary conditions now are

$$\left.\begin{array}{l} E_\theta^m = E_\theta^p, E_\phi^m = E_\phi^p \\ H_\theta^m = H_\theta^p, H_\phi^m = H_\phi^p \end{array}\right\} \text{ for } r = a \tag{2.2}$$

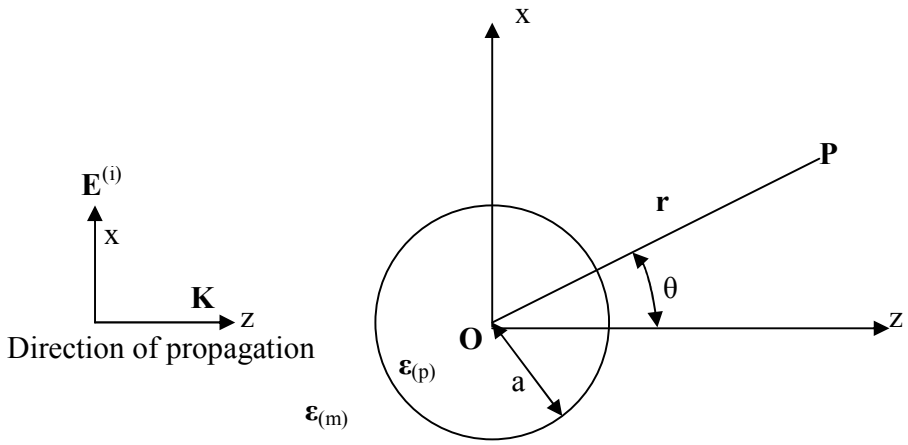

Figure 2.1 The model of diffraction by a sphere immersed in a homogeneous, isotropic medium.

2.2 The solution of Maxwell equations for non-magnetic particles

In a completely analogous way as in Ref. [84], one can prove that the electromagnetic fields in a region between two concentric spheres, in which there are no free charges and currents, are completely determined by two scalar functions ${}^{e}D(r,\theta,\varphi)$ and ${}^{h}D(r,\theta,\varphi)$, the so-called electric and magnetic Debye potentials. The potentials fulfill the scalar Helholtz equation:

$$\nabla^2 D + k^2 D \equiv \frac{1}{r^2}\frac{\partial}{\partial r}\left(r^2\frac{\partial D}{\partial r}\right)+\frac{1}{r^2\sin\theta}\frac{\partial}{\partial\theta}\left(\sin\theta\frac{\partial D}{\partial\theta}\right)+\frac{1}{r^2\sin\theta}\frac{\partial^2 D}{\partial\varphi^2}+k^2 D = 0, \tag{2.3}$$

The electric and magnetic fields can be derived from these potentials by:

$$\mathbf{E}=\nabla\times\nabla\times\left(\mathbf{r}\ {}^{e}D\right)+ik\,\nabla\times(\mathbf{r}\ {}^{h}D),\quad \mathbf{H}=\sqrt{\varepsilon_m}\left[\nabla\times\nabla\times\left(\mathbf{r}\ {}^{h}D\right)-ik\,\nabla\times(\mathbf{r}\ {}^{e}D)\right]. \tag{2.4}$$

where $k = \frac{\omega}{c}\sqrt{\varepsilon}$ is the wave vector. The solution with vanishing radial magnetic field is called the electric wave (or transverse magnetic wave) and that with vanishing radial electric field is called the magnetic wave (or transverse electric wave).

It should be noted that different Debye potentials should be defined for inside and outside the particle. To indicate this difference, notations Π and Ψ will be used for outside and inside respectively. Debye potentials can be expanded into sum series of different resonance modes:

$$\text{(Outside sphere): } {}^{e}\Pi = \sum_{\ell=1}^{\infty}\sum_{m=-\ell}^{\ell} {}^{e}w_{\ell}^{m}\Pi_{\ell}^{m}, \quad {}^{h}\Pi = \sum_{\ell=1}^{\infty}\sum_{m=-\ell}^{\ell} {}^{h}w_{\ell}^{m}\Pi_{\ell}^{m}$$

$$\text{(Inside sphere): } {}^{e}\Psi = \sum_{\ell=1}^{\infty}\sum_{m=-\ell}^{\ell} {}^{e}v_{\ell}^{m}\Psi_{\ell}^{m}, \quad {}^{h}\Psi = \sum_{\ell=1}^{\infty}\sum_{m=-\ell}^{\ell} {}^{h}v_{\ell}^{m}\Psi_{\ell}^{m} \tag{2.5}$$

where

$$\Pi_{\ell}^{m} = h_{\ell}^{(1)}(kr)\, Y_{\ell}^{m}(\theta,\phi), \quad \Psi_{\ell}^{m} = j_{\ell}(kr) Y_{\ell}^{m}(\theta,\phi), \tag{2.6}$$

Here $h_{\ell}^{(1)}(\rho)$ and $j_{\ell}(\rho)$ are spherical Hankel and Bessel functions of order ℓ respectively:

$$h_{\ell}^{(1)}(\rho) \equiv \sqrt{\frac{\pi}{2\rho}}\, H_{\ell+1/2}^{(1)}(\rho), \qquad j_{\ell}(\rho) \equiv \sqrt{\frac{\pi}{2\rho}}\, J_{\ell+1/2}(\rho) \tag{2.7}$$

and $Y_\ell^m(\theta,\varphi)$ the spherical harmonics function of degree ℓ and order m:

$$Y_\ell^m(\theta,\varphi)=[(2\ell+1)\frac{(\ell-m)!}{(\ell+m)!}]^{1/2}\ P_\ell^m(\cos\theta)\,e^{\,im\varphi}, \tag{2.8}$$

With the associated Legendre function $P_\ell^m(\cos\theta)$:

$$P_\ell^m(\eta)\equiv\frac{(1-\eta^2)^{m/2}}{2^\ell.\ell!}\frac{d^{\,\ell+m}}{d\eta^{\,\ell+m}}(\eta^2-1)^\ell \quad (m\geq 0)$$

$$P_\ell^m(\eta)\equiv(-1)^{-m}\frac{(\ell+m)!}{(\ell-m)!}P_\ell^{-m}(\eta) \quad (m<0) \tag{2.9}$$

The field is thus completely determined by the coefficients ${}^e w_\ell^m$, ${}^h w_\ell^m$, ${}^e v_\ell^m$ and ${}^h v_\ell^m$ in Eq. (2.5).

The amplitude of the electric vector of the incident plane wave is normalized to unity, and wave propagates along the *z*-coordinate, electric vector is directed along *x*-coordinate and magnetic vector along the *y*-coordinate. In the spherical coordinate system {*r*, θ, φ} with the origin situated at the sphere center, these spherical waves can be expressed as the following (index "*i*" indicates the incident wave):

$$E_r^{(i)}=\frac{\cos\varphi}{(k_m\,r)^2}\sum_{\ell=1}^{\infty}\ i^{\,\ell-1}\,(2\ell+1)\ \psi_\ell(k_m r)\,P_\ell^{(1)}(\cos\theta),$$

$$E_{\theta}^{(i)} = -\frac{\cos\varphi}{k_m r}\sum_{\ell=1}^{\infty} i^{\ell-1}\frac{2\ell+1}{\ell(\ell+1)}\left[\psi'_{\ell}(k_m r)\,P_{\ell}^{(1)'}(\cos\theta)\sin\theta - i\,\psi_{\ell}(k_m r)\frac{P_{\ell}^{(1)}(\cos\theta)}{\sin\theta}\right],$$

$$E_{\varphi}^{(i)} = -\frac{\sin\varphi}{k_m r}\sum_{\ell=1}^{\infty} i^{\ell-1}\frac{2\ell+1}{\ell(\ell+1)}\left[\psi'_{\ell}(k_m r)\frac{P_{\ell}^{(1)}(\cos\theta)}{\sin\theta} - i\,\psi_{\ell}(k_m r)\,P_{\ell}^{(1)'}(\cos\theta)\sin\theta\right],$$

$$H_{r}^{(i)} = \frac{\sqrt{\varepsilon_m}\sin\varphi}{(k_m r)^2}\sum_{\ell=1}^{\infty} i^{\ell-1}(2\ell+1)\,\psi_{\ell}(k_m r)\,P_{\ell}^{(1)}(\cos\theta),$$

$$H_{\theta}^{(i)} = i\frac{\sin\varphi}{k_0 r}\sum_{\ell=1}^{\infty} i^{\ell-1}\frac{2\ell+1}{\ell(\ell+1)}\left[\psi_{\ell}(k_m r)\frac{P_{\ell}^{(1)}(\cos\theta)}{\sin\theta} + i\,\psi'_{\ell}(k_m r)\,P_{\ell}^{(1)'}(\cos\theta)\sin\theta\right],$$

$$H_{\varphi}^{(i)} = -i\frac{\cos\varphi}{k_0 r}\sum_{\ell=1}^{\infty} i^{\ell-1}\frac{2\ell+1}{\ell(\ell+1)}\left[\psi_{\ell}(k_m r)P_{\ell}^{(1)'}(\cos\theta)\sin\theta + i\,\psi'_{\ell}(k_m r)\frac{P_{\ell}^{(1)}(\cos\theta)}{\sin\theta}\right],$$

(2.10)

where the radial dependence is expressed through the Bessel function (regular at $\rho = 0$) and prime indicates differentiation

$$\psi_{\ell}(\rho) = \rho\, j_{\ell}(\rho) = \sqrt{\frac{\pi\rho}{2}}\,J_{\ell+1/2}(\rho), \quad \psi'_{\ell}(\rho) = \frac{\partial\psi_{\ell}(\rho)}{\partial\rho}.$$

(2.11)

The scattered field for the non-magnetic particle ($\mu_p = 1$) immersed in vacuum is presented by (index "*s*" stands for indication of the scattered wave):

$$E_r^{(s)} = \frac{\cos\varphi}{(k_m r)^2} \sum_{\ell=1}^{\infty} \ell(\ell+1)\, {}^{e}B_\ell\, \zeta_\ell(k_m r)\, P_\ell^{(1)}(\cos\theta),$$

$$E_\theta^{(s)} = -\frac{\cos\varphi}{k_m r} \sum_{\ell=1}^{\infty} \left[{}^{e}B_\ell\, \zeta_\ell'(k_m r)\, P_\ell^{(1)\prime}(\cos\theta)\sin\theta - i\ {}^{m}B_\ell\, \zeta_\ell(k_m r) \frac{P_\ell^{(1)}(\cos\theta)}{\sin\theta} \right],$$

$$E_\varphi^{(s)} = -\frac{\sin\varphi}{k_m r} \sum_{\ell=1}^{\infty} \left[{}^{e}B_\ell\, \zeta_\ell'(k_m r) \frac{P_\ell^{(1)}(\cos\theta)}{\sin\theta} - i\ {}^{m}B_\ell\, \zeta_\ell(k_m r)\, P_\ell^{(1)\prime}(\cos\theta)\sin\theta \right],$$

$$H_r^{(s)} = \frac{\sqrt{\varepsilon_m}\,\sin\varphi}{(k_m r)^2} \sum_{\ell=1}^{\infty} \ell(\ell+1)\ {}^{m}B_\ell\, \zeta_\ell(k_m r)\, P_\ell^{(1)}(\cos\theta),$$

$$H_\theta^{(s)} = i\,\frac{\sin\varphi}{k_0 r} \sum_{\ell=1}^{\infty} \left[{}^{e}B_\ell\, \zeta_\ell(k_m r) \frac{P_\ell^{(1)}(\cos\theta)}{\sin\theta} + i\ {}^{m}B_\ell\, \zeta_\ell'(k_m r)\, P_\ell^{(1)\prime}(\cos\theta)\sin\theta \right],$$

$$H_\varphi^{(s)} = -i\,\frac{\cos\varphi}{k_0 r} \sum_{\ell=1}^{\infty} \left[{}^{e}B_\ell\, \zeta_\ell(k_m r) P_\ell^{(1)\prime}(\cos\theta)\sin\theta + i\ {}^{m}B_\ell\, \zeta_\ell'(k_m r) \frac{P_\ell^{(1)}(\cos\theta)}{\sin\theta} \right],$$

(2.12)

where

$$\zeta_\ell(\rho) = \rho\, h_\ell^{(1)}(\rho) = \sqrt{\frac{\pi\rho}{2}}\, H_{\ell+1/2}^{(1)}(\rho), \qquad \zeta_\ell'(\rho) = \frac{\partial \zeta_\ell(\rho)}{\partial \rho}.$$

(2.13)

Coefficients ${}^{e}B_\ell$ and ${}^{m}B_\ell$ in Eq. (2.12) are given by

$$ {}^{e}B_{\ell} = i^{\ell+1}\frac{2\ell+1}{\ell(\ell+1)}a_{\ell}, \qquad {}^{m}B_{\ell} = i^{\ell+1}\frac{2\ell+1}{\ell(\ell+1)}b_{\ell} \tag{2.14} $$

where a_ℓ and b_ℓ are defined as

$$ a_{\ell} = \frac{q_p\psi'_{\ell}(q_m)\psi_{\ell}(q_p) - q_m\psi_{\ell}(q_m)\psi'_{\ell}(q_p)}{q_p\zeta'_{\ell}(q_m)\psi_{\ell}(q_p) - q_m\psi'_{\ell}(q_p)\zeta_{\ell}(q_m)}, \quad q_m = k_m a = \frac{2\pi}{\lambda}a $$

$$ b_{\ell} = \frac{q_p\psi'_{\ell}(q_p)\psi_{\ell}(q_m) - q_m\psi_{\ell}(q_p)\psi'_{\ell}(q_m)}{q_p\psi'_{\ell}(q_p)\zeta_{\ell}(q_m) - q_m\psi_{\ell}(q_p)\zeta'_{\ell}(q_m)}, \quad q_p = k_p a = \frac{2\pi n_p}{\lambda}a . \tag{2.15} $$

These formulae take particularly simple forms when either the dielectric constant or the conductivity of the sphere is high, and at the same time the radius of the sphere is not too small. In this case $n_p >> 1$, $\dfrac{q_p}{q_m} = n_p >> 1$ and ${}^{e}B_l$, ${}^{m}B_l$ reduce to

$$ \left.\begin{aligned} {}^{e}B_{\ell} &= i^{\ell+1}\frac{2\ell+1}{\ell(\ell+1)}\frac{\psi'_l(q_m)}{\zeta'_l(q_m)} \\ {}^{m}B_{\ell} &= i^{\ell+1}\frac{2\ell+1}{\ell(\ell+1)}\frac{\psi_l(q_m)}{\zeta_l(q_m)} \end{aligned}\right\}, \tag{2.16} $$

This approximation is of little interest for optics, but it is of importance in connection with radio waves. It is also historical interest as the early theories were concerned with this limiting case [85].

The internal fields (indicated by index "*a*") inside the particle are given by

$$E_r^{(a)} = \frac{\cos\varphi}{(k_p r)^2} \sum_{\ell=1}^{\infty} \ell(\ell+1)\ {}^{e}A_\ell\ \psi_\ell(k_p r) P_\ell^{(1)}(\cos\theta),$$

$$E_\theta^{(a)} = -\frac{\cos\varphi}{k_p r} \sum_{\ell=1}^{\infty} \left[{}^{e}A_\ell\ \psi'_\ell(k_p r) P_\ell^{(1)'}(\cos\theta)\sin\theta - i\ {}^{m}A_\ell\ \psi_\ell(k_p r) \frac{P_\ell^{(1)}(\cos\theta)}{\sin\theta} \right],$$

$$E_\varphi^{(a)} = -\frac{\sin\varphi}{k_p r} \sum_{\ell=1}^{\infty} \left[{}^{e}A_\ell\ \psi'_\ell(k_p r) \frac{P_\ell^{(1)}(\cos\theta)}{\sin\theta} - i\ {}^{m}A_\ell\ \psi_\ell(k_p r) P_\ell^{(1)'}(\cos\theta)\sin\theta \right],$$

$$H_r^{(a)} = \frac{\sqrt{\varepsilon_p}\sin\varphi}{(k_p r)^2} \sum_{\ell=1}^{\infty} \ell(\ell+1)\ {}^{m}A_\ell\ \psi_\ell(k_p r) P_\ell^{(1)}(\cos\theta),$$

$$H_\theta^{(a)} = i\frac{\sin\varphi}{k_0 r} \sum_{\ell=1}^{\infty} \left[{}^{e}A_\ell\ \psi_\ell(k_p r) \frac{P_\ell^{(1)}(\cos\theta)}{\sin\theta} + i\ {}^{m}A_\ell\ \psi'_\ell(k_p r) P_\ell^{(1)'}(\cos\theta)\sin\theta \right],$$

$$H_\varphi^{(a)} = -i\frac{\cos\varphi}{k_0 r} \sum_{\ell=1}^{\infty} \left[{}^{e}A_\ell\ \psi_\ell(k_p r) P_\ell^{(1)'}(\cos\theta)\sin\theta + i\ {}^{m}A_\ell\ \psi'_\ell(k_p r) \frac{P_\ell^{(1)}(\cos\theta)}{\sin\theta} \right]. \qquad (2.17)$$

Coefficients ${}^{e}A_\ell$ and ${}^{m}A_\ell$ in Eq. (2.17) are given by

$${}^{e}A_\ell = i^{\ell+1}\frac{2\ell+1}{\ell(\ell+1)}c_\ell, \quad {}^{m}A_\ell = i^{\ell+1}\frac{2\ell+1}{\ell(\ell+1)}d_\ell, \qquad (2.18)$$

where c_ℓ and d_ℓ are defined as

$$c_\ell = \frac{q_p\varsigma_\ell(q_m)\psi'_\ell(q_m) - q_p\varsigma'_\ell(q_m)\psi_\ell(q_m)}{q_p\varsigma'_\ell(q_m)\psi_\ell(q_p) - q_m\psi'_\ell(q_p)\varsigma_\ell(q_m)},$$

$$d_\ell = \frac{q_p \varsigma'_\ell(q_m)\psi_\ell(q_m) - q_p \varsigma_\ell(q_m)\psi'_\ell(q_m)}{q_p \psi'_\ell(q_p)\varsigma_\ell(q_m) - q_m \psi_\ell(q_p)\varsigma'_\ell(q_m)}. \tag{2.19}$$

2.3 The solution for magnetic particles

The given solutions in the above sections only deal with nonmagnetic spherical particles, e.g., $\mu_P = \mu_m = 1$. In the cases of magnetic spheres, μ_P and μ_m quantities should be included in the wave solutions. Firstly, from Eqs. (2.10) to (2.19), the following new quantities in Table 2.1 should be used. Secondly, the magnetic field components for scattered and incident waves, i.e. waves outside of sphere, should be multiplied by a factor of $1/\mu_m$, and $1/\mu_p$ for internal wave. Finally, the wave expansion coefficients, including both the scattering coefficients of Eq. (2.15) and the internal field coefficients of Eq. (2.19) should be modified accordingly. New scattering coefficients are given by:

Table 2.1 Notations for nonmagnetic and magnetic spheres

Nonmagnetic	**Replaced by**	**Magnetic**
$\sqrt{\varepsilon_m} = n_m + i\kappa_m$	$\Leftrightarrow$	$\sqrt{\varepsilon_m \mu_m} = n_m + i\kappa_m$
$k_m = 2\pi\sqrt{\varepsilon_m}/\lambda$	$\Leftrightarrow$	$k_m = 2\pi\sqrt{\varepsilon_m \mu_m}/\lambda$
$\sqrt{\varepsilon_p} = n_p + i\kappa_p$	$\Leftrightarrow$	$\sqrt{\varepsilon_p \mu_p} = n_p + i\kappa_p$
$k_p = 2\pi\sqrt{\varepsilon_p}/\lambda$	$\Leftrightarrow$	$k_p = 2\pi\sqrt{\varepsilon_p \mu_p}/\lambda$

$$a_\ell = \frac{q_p \mu_m \psi'_\ell(q_m)\psi_\ell(q_p) - q_m \mu_p \psi_\ell(q_m)\psi'_\ell(q_p)}{q_p \mu_m \varsigma'_\ell(q_m)\psi_\ell(q_p) - q_m \mu_p \psi'_\ell(q_p)\varsigma_\ell(q_m)}, \quad q_m = k_m a$$

$$b_\ell = \frac{q_p \mu_m \psi'_\ell(q_p)\psi_\ell(q_m) - q_m \mu_p \psi_\ell(q_p)\psi'_\ell(q_m)}{q_p \mu_m \psi'_\ell(q_p)\varsigma_\ell(q_m) - q_m \mu_p \psi_\ell(q_p)\varsigma'_\ell(q_m)}, \quad q_p = k_p a.$$

(2.20)

2.4 Calculated distribution of light intensity under dielectric particles

In the limiting cases of geometrical optics and dipole approximation, the field is obtained with approximations. By Mie theory, we are able to see the exact field distribution. An example of Mie calculation is shown in Fig. 2.2 for a radius of $a = 0.5\mu m$ silica particle illuminated by laser at $\lambda = 800\ nm$. Both Figs. 2.2(a) and (b) show that the light speed inside the particle is lower than that in the medium since the refractive index of particle is larger, which results in the incident plane wave being bent along z direction in particle center. From Fig. 2.2(c), it can be seen that the electric field is greatly enhanced in the near-field region under the transparent particle. The electric field enhancement decays quickly (almost exponentially as a character of NFO) from 15 at $z = a$ to 3.5 at $z = 2a$. Within the $z = a$ tangential plane, the distribution of laser intensity is shown in Fig. 2.3. One can see the high localization of laser intensity in this plane. The intensity profiles of $I = |E|^2$ and I = S shown here is different from each other although the peak values are close. The profile of $|E|^2$ intensity is not in a round shape but

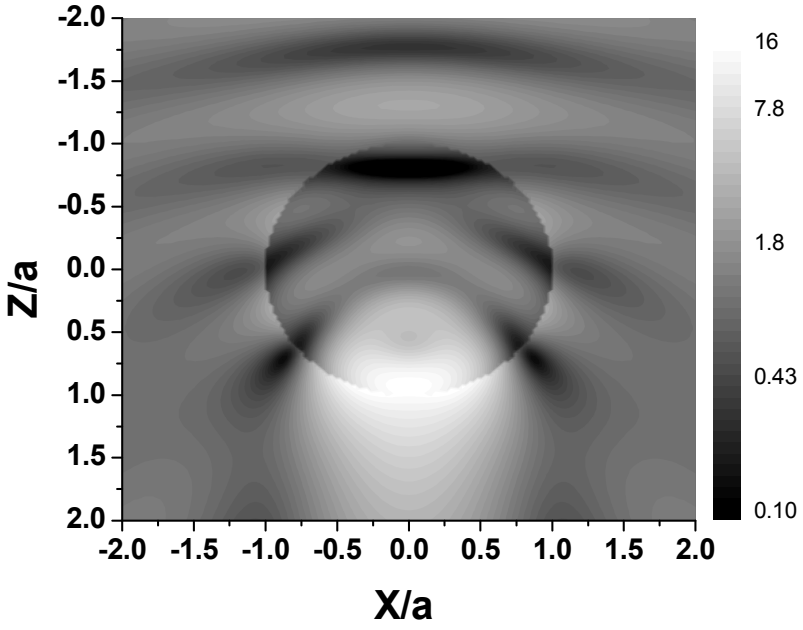
-2.0
-1.5
-1.0
-0.5
0.0
0.5
1.0
1.5
2.0
Z/a
-2.0 -1.5 -1.0 -0.5 0.0 0.5 1.0 1.5 2.0
X/a
16
7.8
1.8
0.43
0.10

(a)

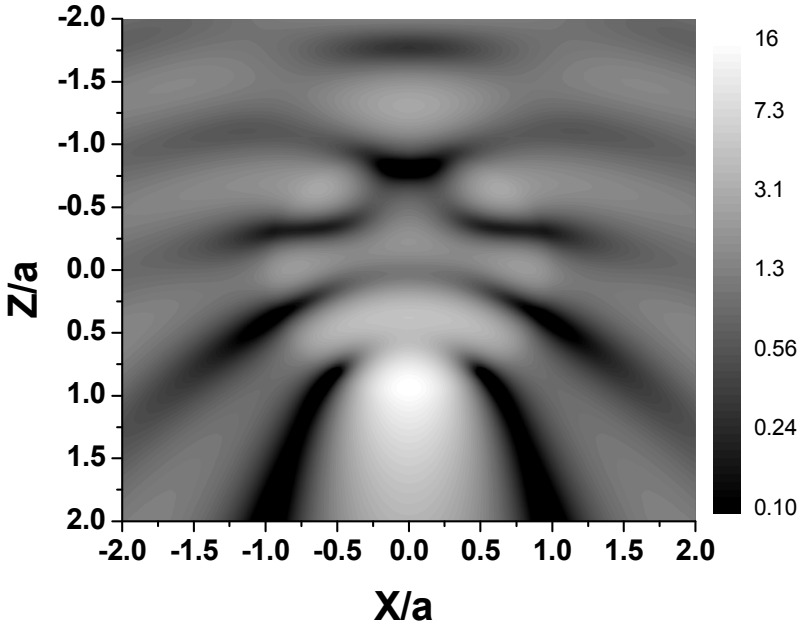
-2.0
-1.5
-1.0
-0.5
0.0
0.5
1.0
1.5
2.0
Z/a
-2.0 -1.5 -1.0 -0.5 0.0 0.5 1.0 1.5 2.0
X/a
16
7.3
3.1
1.3
0.56
0.24
0.10

(b)

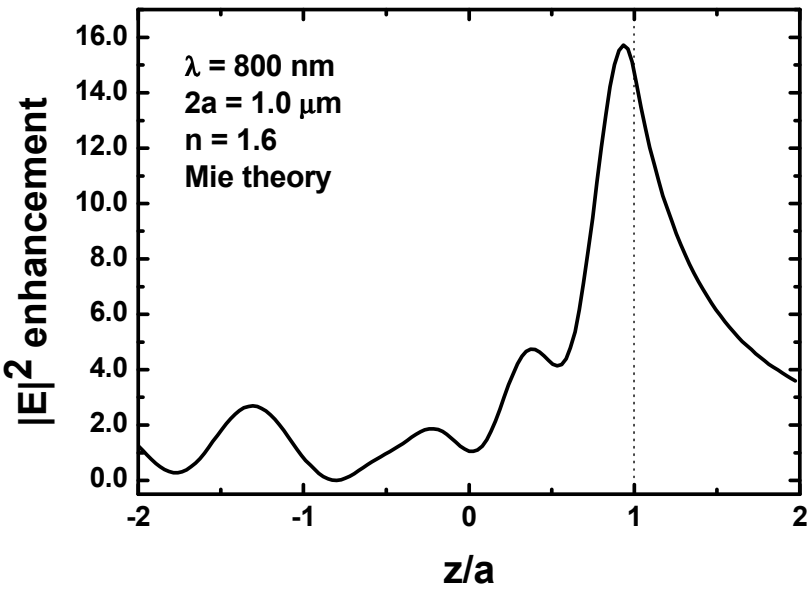

(c)

Figure 2.2 Spatial Intensity distribution, $I = |E|^2$, inside and outside a = 0.5 μm glass particle, illuminated by a laser at λ = 800 nm, and (a) polarization parallel and (b) perpendicular to the image plane. The maximum intensity enhancement in calculations is about 15.7 for both regions. (c) shows the intensity along *z*-axis. z = 1.0 is the position under the particle.

difference between them originally comes from the contribution of the *r*-component of electrical vector, E_r, which decays with *r* as $E_r \propto 1/r^2$ from the scattering centre, whereas the amplitudes of the other components fall off more slowly, as the inverse of this distance. It quickly tends to zero in the far field ($r \geq \lambda$). In other words, at sufficiently great distances, in the radiation zone or wave zone, the radial components may, therefore, be neglected in comparison with the tangential components, i.e. the scattered wave in the far field is a transverse wave for which the $|E|^2$ and S intensity are identical. But the scattered wave in the near field is not transverse which results in the difference.

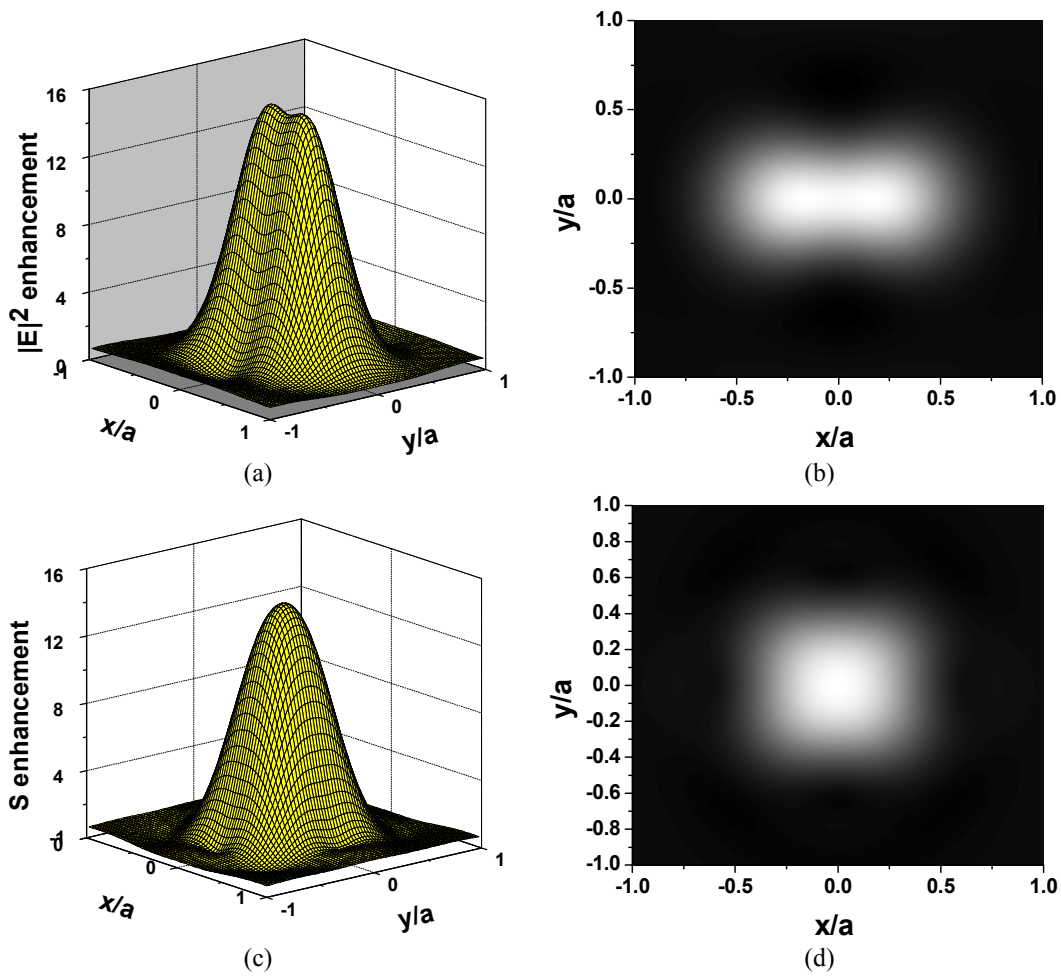

Figure 2.3 Distribution of laser intensity within the tangential plane under the particle with radius a = 0.5 μm, illuminated by laser at λ = 800 nm. (a) 3D picture of the $I = |E|^2$ intensity distribution. (b) contour plot of (a). (c) 3D picture of $I = S$ intensity distribution and (d) contour plot of (c). Particle is considered to be nonabsorbing with refractive index n = 1.6.

2.5 Calculated distribution of laser intensity under the metal nanoparticle

2.5.1 Drude model for metals

The material properties needed for the electrodynamical calculations have to be

calculated using solid state theory. A simple model for metals was developed by Drude (1900) based on the kinetic gas theory. It assumes independent and free electrons with a common relaxation time. Sommerfeld incorporated corrections originating from the Pauli-exclusion principle (Fermi-Dirac velocity distribution). This so-called free-electron model was later modified to include minor corrections from the band-structure of matter (effective mass) and termed quasi-free-electron model.

The basic picture of the properties of metals in the frame work of this theory is a gas of independent point-like electrons. These electrons move freely between independent collisions with unspecified collision centers (lattice ions, other electrons, defects, phonons, etc.), which occur with an average rate of $\gamma_0 = \tau^{-1}$ with τ being the so-called electron relaxation time. Each collision leads to a complete loss of directional information and results in a random orientation of the electron velocity afterwards.

In an external field, the electrons are accelerated between collisions resulting in a drift motion. In reality, only electrons near the Fermi level contribute, because the Pauli exclusion principle does not allow deeper lying electrons to change their electronic state. Band-structure corrections lead to a modification of this motion. These corrections are customarily incorporated into an effective mass m^*, which is in general different from the free-electron mass m_e.

Many properties of real metals, including their optical properties as described by the frequency dependent dielectric function $\varepsilon(\omega)$, are surprisingly well predicted from this

simple model. The resulting equation is:

$$\varepsilon(\omega) = n_c^2 = 1 - \frac{\omega_p^2}{\omega^2 + \gamma^2} + i\frac{\gamma}{\omega}\frac{\omega_p^2}{\omega^2 + \gamma^2} \qquad (2.21)$$

with ω_p the so-called plasma frequency and γ_0 the electron relaxation rate. ε_∞ includes the contribution of the bound electrons to the polarizability and should have the value of 1 if only the conduction band electrons contribute to the dielectric function. The plasma frequency is given by $\omega_p = \sqrt{\frac{\rho e^2}{\varepsilon_0 m^*}}$ with ρ and m^* being the density and effective mass of the conduction electrons, respectively. The electron relaxation time can be calculated from the DC conductivity σ by $\tau = \frac{\sigma m^*}{\rho e^2}$.

In real metals, besides the contribution of the free electrons, the effects of interband transitions have to be considered. For alkali metals, such as sodium and potassium, interband transitions do not affect the dielectric function in the visible range, because the energy of the band gap is large. For the noble metals, such as copper, silver and gold, the influence of interband transitions in the visible range can not be ignored. For them, then interband transitions are 3d → 4sp, 4d → 5sp, and 5d → 6sp, respectively, and the free electrons are in the 4s, 5s and 6s states. For copper and gold, the absorption edge due to interband transitions is in the visible range, so that these metals are colored. For silver, although the absorption edge is in the ultraviolet, it affects the dielectric constant in the visible range a lot.

2.5.2 Light intensity distribution around metal nanoparticles

In contrast to SCR, the PR mode in a metal sphere is generated due to the oscillation of free electrons. The PR mode is damping mode due to the high dissipative factor of metals. Unlike 40 nm silica particle which produces "shadowing effect" [86] instead of light energy enhancement under laser irradiation, 40 nm gold particle can produce enhancement due to surface plasmon resonance effect [87,88].

Due to the development of nanotechnologies, the study of light scattering by small particles becomes especially important. Bohren published the first work in this field in 1983 within the frame of dipole approximations [89]. He demonstrated that the energy flux in the vicinity of a small particle deflects towards the particle from the surrounding area. As a result the particle can absorb much more radiation than that given by the geometrical cross-section. This presentation clearly explains the growth of the particle absorption process for small ε'' near plasmon resonance frequency, $\omega = \omega_p$, when $\varepsilon(\omega_p) = -2 + i\varepsilon''$. It should be mentioned, according to Ref. [20], that the absorption cross-section increases inversely proportional to ε''. But, it is very questionable that the particle absorbs incident energy through its whole surface.

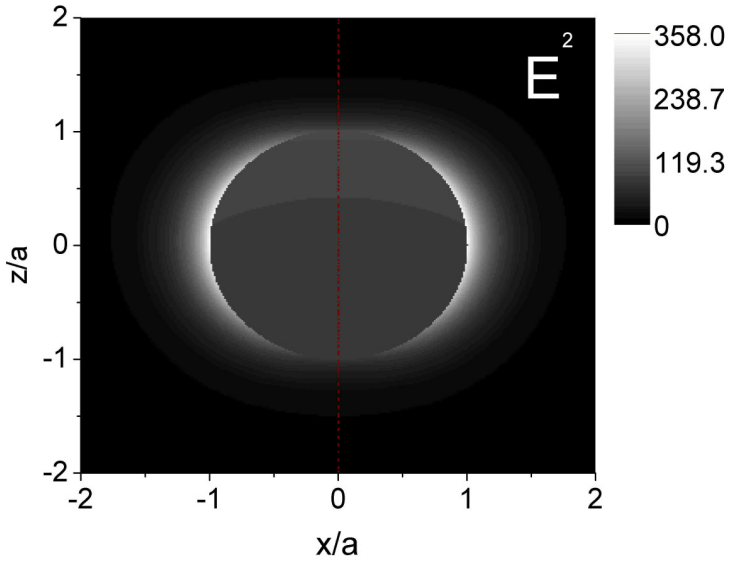

(a)

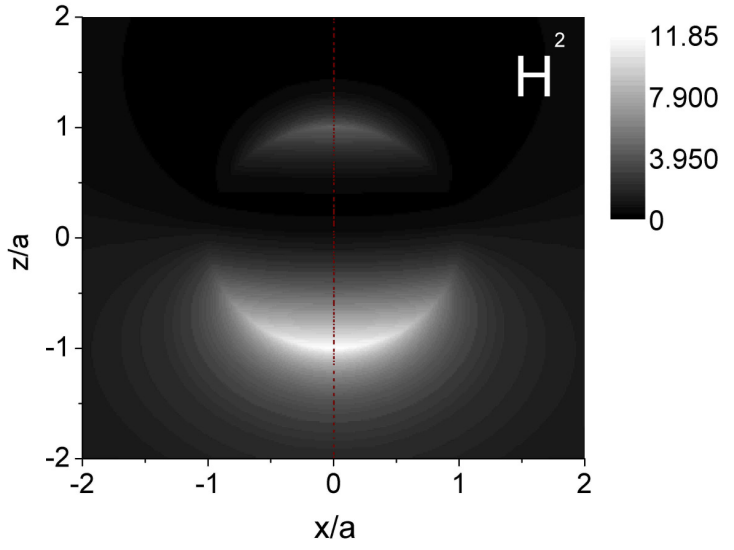

(b)

Figure 2.4. Electric $|\boldsymbol{E}|^2$ and magnetic $|\boldsymbol{H}|^2$ fields distributions within the *xz*-plane, calculated from the Mie theory for a sphere with q = 0.3 and dielectric function $\varepsilon = -2 + 0.2\,i$. Incident electric field is directed along *x*-axis.

This question stems from the fact that the refractive index of the particle $n = \mathrm{Re}\sqrt{\varepsilon' + i\varepsilon''}$ with $\varepsilon' = -2$ becomes smaller than 1 when ε'' < 3.464. From the geometrical optics point of view (when a particle is big compared to λ), some incident rays cannot "enter" the particle due to total internal reflection. In other words, a particle with a small ε'' value should absorb incident energy just through some "input window" on its surface and this window should be smaller with decreasing ε''.

Examples of calculations from Mie theory for the electrical and magnetic fields are shown in Fig. 2.4. Plasmon is localized under the particle for magnetic field and equator plane for electric field [90]. The field distributions are typical for dipole radiation. One can see that the electric field mainly concentrates along "left" and "right" surfaces, while magnetic field is localized near "top" and "bottom" surfaces.

Chapter 3 Experimental details

3.1 Sample preparation

The near-field distribution around a small particle under laser irradiation can be imaged by NSOM/SNOM systems [91,92]. However, the presence of a tip/particle/aperture in the near-field region could significantly distort the original field, and NSOM/SNOM systems are not able to detect the field inside the gap between the particle and surface. To overcome these, Mǜnzer *et al*. [93] proposed that the field under the particle can be directly mapped by the post-processing patterns left on the substrate.

In experiment, two kinds of particles were used: (1) SiO_2 particle (Duke, $n = 1.6$, 10% size deviation, in suspension), (2) Gold nanoparticle (5% size deviation, in suspension form).

For experiment, we need to prepare an appropriate particle mask on substrate surface. In principle, a single sphere is sufficient for our study but it is rather difficult to locate them in experiment. An applicable choice is to prepare a monolayer particle on surface in an acceptable area. An easy method to prepare such mask is by self-assembly. The phenomenon of self-assembly is due to the mutually attractive 'lateral capillary force' developed between the particles caused by the deformation of the liquid layer when it evaporates. It is a function of the particle radius and the liquid surface tension. Ideally, the process leaves behind an order array of closely packed monolayer of particles under some conditions: (a) chemical homogeneity of the surface, (b) clean and hydrophilic flat surface,

and (c) evaporation temperature. More information on this topic can be found in Ref. [94,95].

The substrate was cleaned with acetone in an ultrasonic bath for 5 minutes followed by rinsing in DI water and then dried by N_2 gas. The as-received particle suspensions were diluted and disposed onto the sample surface with a 0.5 μL dispenser. The sample was slightly titled (at an angle of 5 degree) and kept in a refrigerator at ~10 ^{o}C until dry. The final sample was baked in a vacuum oven at ~80 ^{o}C for 10 minutes to remove the water molecules on the surface. Figure 3.1 shows a typical particle mask prepared by this method. The major part of the mask is in a hexagonally closely packed monolayer form while some isolated particles are stayed at the edge regions. After laser processing, the patterns left on substrate surfaces can be examined by field emission scanning electron microscope (FESEM) and atomic force microscopy (AFM).

The recording medium sample was coated with P1205 positive tone photoresist. To obtain a uniform layer of photoresist, the resist was spin coated on the sample surface using a spin coater. Centrifugal force during the spinning of the sample vacuum chuck causes the photoresist to widespread from the center of the sample until it covers the whole sample surface. The coater's spin speed determines the thickness of the photoresist coated over the substrate. For P1205 photoresist, a typical spin speed of 5000 rpm corresponding to a resist thickness of ~ 0.5 μm. The coated sample needs to undergo a pre-expose soft bake at 100 ºC on a hotplate for 60 seconds to remove the moisture and harden the photoresist.

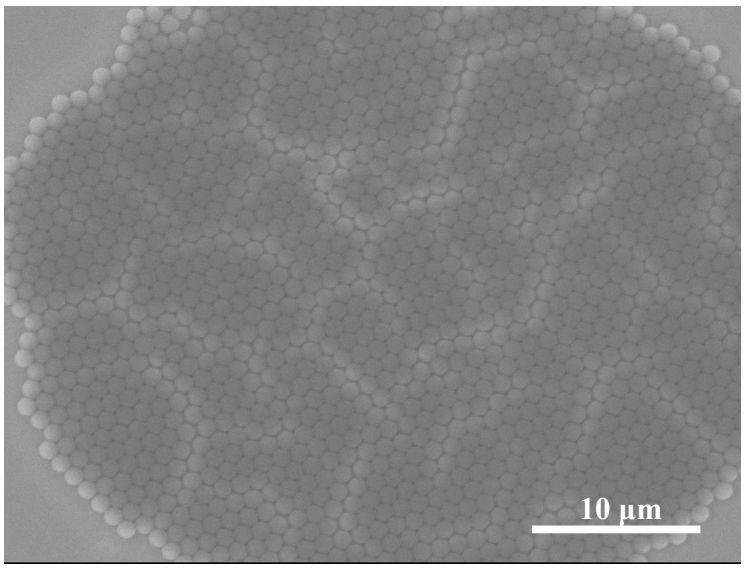

(a)

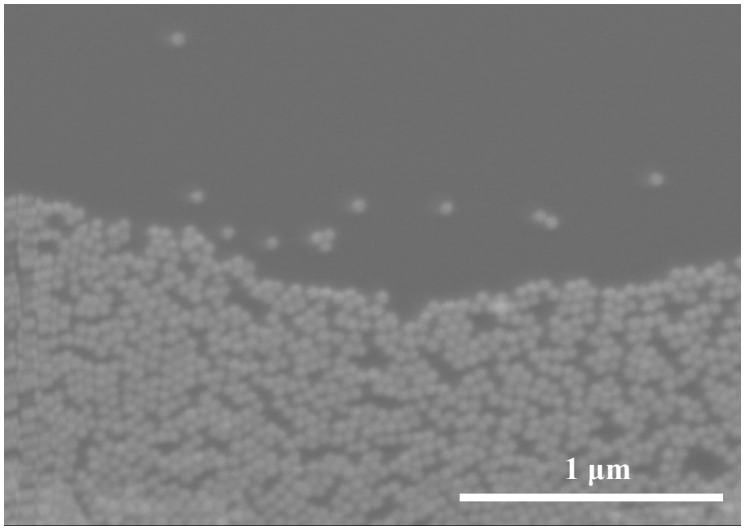

(b)

Figure 3.1. Self-assembly of (a) 1 μm silica particles array and (b) 40 nm Au particles on silicon wafers

3.2 Experimental setup

The laser beam is redirected with a 45^{o} high reflectivity dielectric mirror through an adjustable aperture placed in front of a near infra-red objective lens (20X, NA: 0.40) with a focal length of 20 cm. The samples are set at the focus plane with a spot size around 5.4 μm on surface as shown in Fig. 3.2. taking femtosecond system as an example. The laser spot is paralleling scanned through the particle covered regions with a motion stage. For details on our femtosecond laser and motion systems, one can refer to Ref. [96].

3.3 Light sources

3.3.1 Femtosecond laser

The femtosecond laser system consisting of a Ti: Sapphire oscillator (Spectra Physics Tsunami) and a regenerative amplifier (Spectra Physics Spitfire) provide high-intensity femtosecond laser pulses. A self-mode-locked Ti:Sapphire laser oscillator produces ~80 femtosecond pulses at a wavelength of 800 nm and a repetition rate of 80 MHz. The oscillator provides seed pulses into the regenerative amplifier, which is based on chirped pulse amplification (CPA) technique. The pulse duration of the output beam from the amplifier is ~100 femtosecond with nominal wavelength at 800 nm. The repetition rate can be set from 1 to 1000 Hz and the beam profile emitted from the regenerative amplifier is approximately Gaussian shape. Beam diameter at the laser exit window is elliptical with an average diameter of 5 mm.

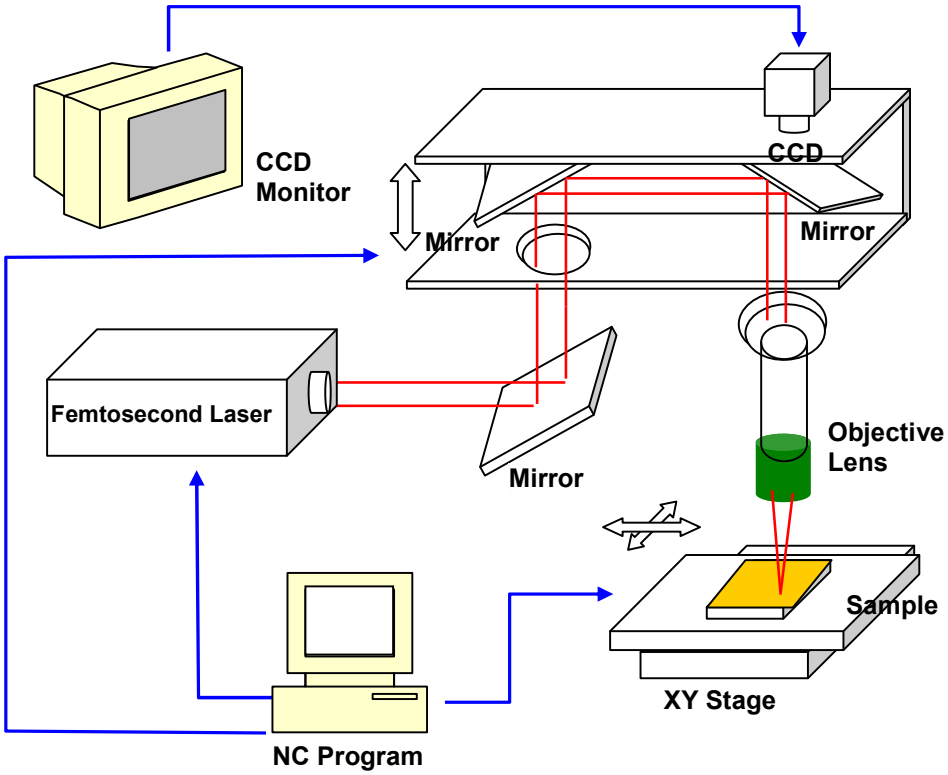

Figure 3.2. Schematic drawing of the laser processing system

3.3.2 KrF excimer laser

The KrF excimer laser (Lambda Physik LPX50) with a wavelength of 248 nm, a FWHM (Full Width at Half Maximum) pulse duration of 23 ns, a maximum repetition rate of 30 Hz and a maximum pulse energy of 300 mJ was used as one of the laser sources in our experiment. The output laser light is non-polarized and has a rectangular intensity profile (spot size: $\sim 4\ cm \times 2\ cm$). A lens of 500 mm focal length focused laser beam onto

the sample mounted on a holder. The holder can be rotated to control the laser incidence angle on the sample. The normal incidence corresponds to $\alpha = 0°$. Comparing with other Gaussian-beam lasers (for example Nd:YAG and femtosecond lasers), the KrF laser has a better beam quality in terms of its intensity homogeneity within the spots. It is the preferred laser source in this project.

3.3.3 Nd:YAG 532 nm / 7 ns laser

A Q-switched Nd: YAG laser (BMI industry Series 5000) was used as the laser source to study the effect of wavelength on nanopatterning. The fundamental wavelength of the laser is 1064 nm and it can be converted into its harmonics to get the second harmonic at 532 nm and third harmonic at 355 nm. The output linearly polarized laser light was redirected by a high-reflecting mirror and incident onto sample surface. The spot is about 1 cm in diameter before focusing. The repetition rate can be varied from 1 to 10 Hz and the maximum output pulse energy is about 1200 mJ at 1064 nm.

3.3.4 Nd: YVO_4 1064 nm / 7 ns laser

Nd: YVO_4 laser at 1064 nm wavelength was used as an irradiating source. The maximum output power used was ~ 25 W at a repetition rate of 10 MHz. A galvanometer with a F-theta lens was used to control the scanning direction of the laser through Scanlab software. The scanning speed used is 400 mm/s. The spot size is around 200 μm

3.3 Characterization techniques

The Olympus MX-50 optical microscope was employed to examine the self-assembled masks before and after laser irradiation. The microscope is equipped for up to 150X magnification and it is connected with a CCD camera fed to PC image-acquisition software.

Hitachi S-4100 field emission SEM with a minimum resolution of 15 Angstrom was used in this work. The accelerating voltage is in a range from 5 kV to 30 kV, and the magnification factor can vary from 20 to 300,000. For high quality SEM imaging, our samples were coated with a thin Au film by thermal evaporator before SEM observation.

Atomic force microscope is a lens-free microscope where a tip is mounted on the end of a micro-fabricated tapping mode cantilever as shown in Fig. 3.3. As the sample is scanned, small force of interaction between tip and surface causes the cantilever to deflect, revealing the sample's topography in a three-dimensional way, down to the atomic level. A variety of optical methods have been designed to detect the cantilever deflection. The typical lateral resolution of AFM is about 10 nm. In this project, AFMs (model: DI3000, DI3100) were used to retrieve the 3D profiles of interested patterns.

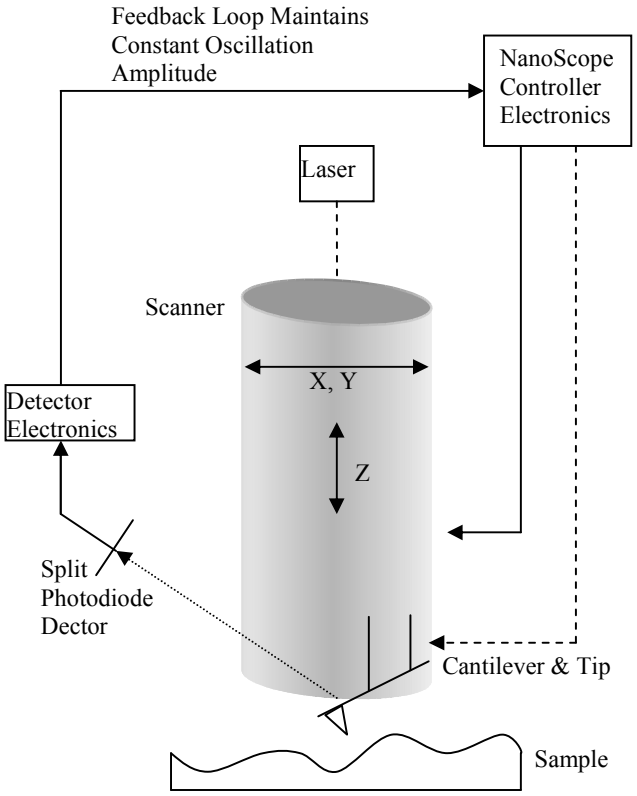

Figure 3.3. Schematic drawing of tapping mode AFM

Chapter 4 Near-field enhanced laser nanopatterning by silica particles

In the research, transparent soda-lime glass was taken as substrate because it is the most common commercial glass with low cost and possesses a large variety of applications in optic devices and optical communications when doped with other elements or compounds. It is also, however, a high challenge for glass processing to get nanostructures due to its hard, brittle, nonconductive and other inert properties. According to the theory, when laser passes through dielectric microspherical particle, the light will be redistributed and confined in a local area resulting in a near-field enhancement in nanometer scale. By applying the enhanced light energy, it is possible for nanopatterning on substrate surface.

4.1 Particles array assisted nanostructuring of glass substrate by femtosecond laser irradiation

4.1.1 Nano-craters formed on the substrate

The technique is to employ the self-assembly of microspheres on the substrate surface and then to focus an incident laser beam to fabricate sub-wavelength holes with single or a few laser shots.

Figure 4.1(a) shows a typical nano-hole array created on the glass substrate after femtosecond laser ($\lambda = 800nm$) irradiation on 1 μm self-assembly glass particles array at a laser fluence of 35 J/cm^2. As it can be seen, the silica particles on glass surface were removed after the laser irradiation, and nano-structures were formed at the place where the particles originally were located. Meanwhile, debris were observed around the nano-crater.

They are hardly to be removed by conventional ultrasonic cleaning due to strong Van der Waals force adhesion [97, 98]. The cross section of craters is shown in Fig. 4.1(b). The full width at the half maximum is about 250 nm and average depth of nanofeatures is around 150 nm. The size of melting zone ranges from 380 to 650 nm.

It is observed that the edges of these nanostructures are free of cracks due to the ultra-short laser pulse. For a long pulse duration laser, the formation of cracks is mainly caused by laser induced high temperature and high pressure [99]. While the processing with ultra-short laser pulses essentially eliminates heat flow to surrounding materials. Therefore, thermally induced substrate crack is prevented.

After 1000 Hz femtosecond laser irradiation in scanning mode, nanobump was formed on glass surface without cracks as shown in Fig.4.2. The laser power density was calculated as 43.67 KW/cm^2. AFM image shows that the bump diameter is 900 nm and the height is 90 nm. The dimple in the center is roughly 200 nm in radius. There exists a threshold value for pulse energy that if exceeded, it would result in nanobump formation. In our case where the laser pulse energy is much higher than threshold energy due to near field enhancement of laser energy, dome-shaped bump with a dimple in the centre is formed. Two most likely mechanisms responsible for the dimple formation are the lateral viscous flow created by the Marangoni effect and laser ablation [70].

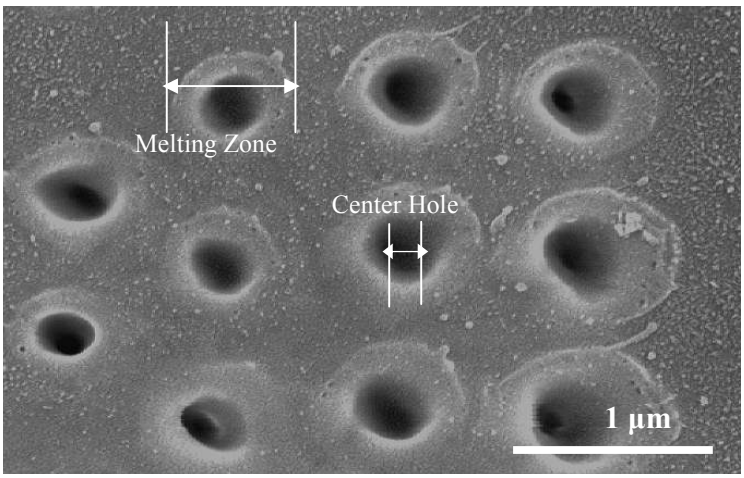

(a)

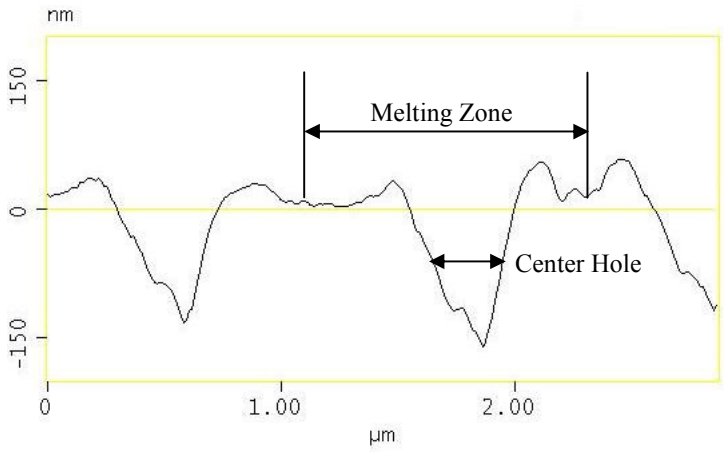

(b)

Figure 4.1 (a) SEM image of nano-craters formed under 1.0 μm Silica particles on glass surface by 800 nm, 100 femtosecond single laser pulse irradiation at a laser fluence of 35 J/cm^2 and (b) AFM image of cross section view of craters.

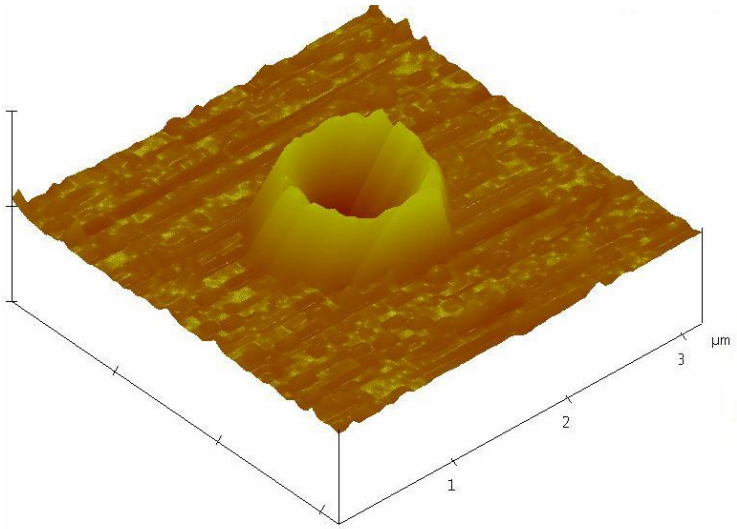

Figure 4.2 AFM image of a nanobump created on glass substrate with 800 nm/100 femtosecond laser irradiation. Scanning speed 400 mm/min, repetition rate 1000 Hz, laser power 10 mW, power density 43.67 KW/cm^2.

4.1.2 Light distribution under a glass particle

The near-field enhancement due to light scattering by the small spherical transparent particles plays an important role in forming of nanopatterns. The distribution of laser energy around spherical particles can be found from the Mie theory [100]. In Fig. 4.3(a), the energy distribution, $I = S$, within the incident plane (xz-plane) is shown for silica particle (refraction index n = 1.6, particle diameter $2a$ = 1 μm) on glass surface under 800 nm laser irradiation. At the interface between a particle and glass surface, laser energy is localized within a small region near the particle-substrate contacting point, both inside and outside the particle. Figure 4.3(b) is 3D picture of Poynting intensity distribution under the particle in tangential plane. It can be found that the focused spot size was about 300 nm. This theoretical value is in good agreement with experimental measurement.

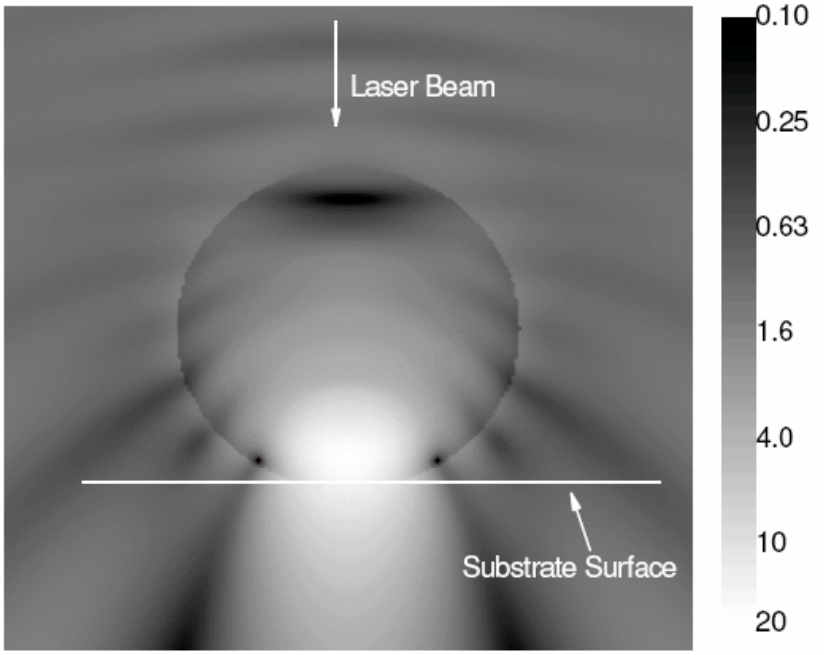

(a)

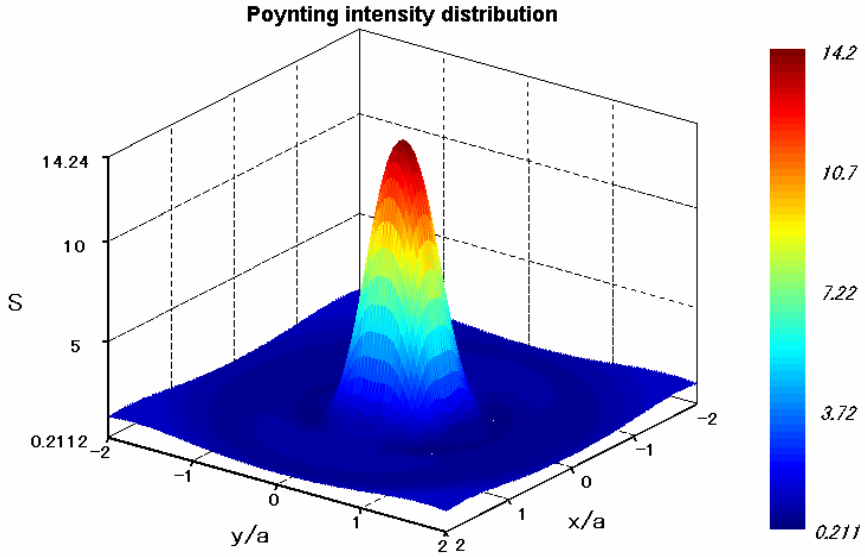

(b)

Figure 4.3 (a) Contour plot of the laser energy, $I = S$, in x-z plane with a 1.0 μm silica particle based on the Mie theory within incident plane. (b) 3D picture of S distribution under the particle in tangential plane. The silica particle is considered as non-absorbing materials for the laser light with a refractive index of 1.6.

Although the enhanced and localized laser intensity was found as high as 20 times of incident intensity, it was distributed as evanescent wave around the particle. Since silica is non-absorptive at 800 nm wavelength, incident light could excite some resonance modes inside the particle as well as produce enhanced light intensities near the contact area. In this case, the particle functions as a lens [6, 101].

4.1.3 Absorption during femtosecond laser irradiation

In recent years, femtosecond laser processing of different kinds of materials has attracted more and more attentions due to its unique advantages over conventional nanosecond lasers: a minimal thermal penetration region and low processing temperature, precision removal of material and good-quality feature definition [96]. Another important feature is that femtosecond laser can deliver an enormous of power (larger than tens of GW) with just a modest of total power for the energy is packed into a short time. This leads to applications such as laser machining and ablation, generation of electromagnetic radiation at unusual wavelength and multiphoton absorption. When such a laser pulse is focused to a small spot, the light intensity and electric field are truly tremendous. The electrical field reaches values millions of times higher than the field of the nucleus attracting electrons. Such chip pulse with very little total energy can generate free electrons and irons in practically any materials. It can be used to machine materials and does not cause heat damage to the nearby substrate. Further, the laser pulse creates the free carriers before energy has time to transfer from the excited carriers to the lattice. The free carriers reach extremely high temperature while the lattice of atoms is still cold. This unique non-equilibrium excitation can cause novel and unusual phase transition. Thus

the use of femtosecond laser for both fundamental studies and applications is increasing rapidly.

Experiments have shown that the nature of the ablation process depends upon the transfer of energy from the laser pulse to the system of electrons on target, then from the electrons to the lattices of the bulk materials. Since linear absorption by the lattice is not active in transparent media, laser ablation is proceeded by the production of a dense laser induced plasma [99,102], which transforms the transparent media into an absorbing media. The crater could not be created with a long pulse duration laser irradiation at that wavelength because that glass is transparent to 800 nm wavelength. Electrons absorb photon energy and consequently transfer the energy to lattices in a very short time that is generally in the timescale of several picoseconds [103] in the condition of long pulse exposure. However in the femtosecond time scale, energy can be deposited into a material faster than needed for the system to react, leading to confinement of important quantities of energy. This pushes the matter into a state of extreme nonequilibrium (for example, near the critical point) and can lead to material properties modification or ejection from the target, i.e. laser ablation.

Multi-photon absorption often takes place for the femtosecond laser pulse interaction with glass. Considering the electronic band gap of the glass (5eV) and the laser photon energy (1.55eV), it is a three-photon absorption process. The *n*-photon absorption is proportional to the *n*th power of the intensity [104]. For the three-photon process, the theory indicates that the fluorescence resulting form three-photon absorption must be proportional to the cube of the laser output. This effect significantly narrows the

processed area. The simultaneous absorption of three-photon was demonstrated by Singh and Bradley [105]. As a result, with femtosecond lasers, the processing area should be confined to the central part of optical axis [104].

Furthermore, at high intensities such as on the peak of an ultrashort laser pulse, the refractive index of any medium becomes a function of the incident intensity. This effect, which is often referred to as the optical Kerr effect [106], can have a significant effect on a femtosecond pulse traveling through a medium. An implication of the nonlinear refractive index is self-focusing or defocusing. As a laser beam is typically more intense in its center, the nonlinear change of the refractive index will be stronger in the center. As a result femtosecond laser-induced non-linear effect gives rise to the change of glass optical properties affecting the propagation of incident light [72, 107]. Then the laser beam is self-focused in a smaller area, which leads to the advantages of a small spot size and extremely high laser fluence to form nanoscale feature size on glass.

4.1.4 Influence of particle size

Figure 4.4 shows the calculated $|E|^2$ intensity field for particles with different sizes of (a) 100 nm, (b) 400 nm, (c) 2.0 μm and (d) 6.8 μm at a same laser wavelength of 532 nm. From Fig. 4.4 (a), it is clear that a small particle could also lead to the decay of field instead of enhancement. As particle size increases shown in Figs. 4.4 (b) - (d), the optical enhancement under the particle increases.

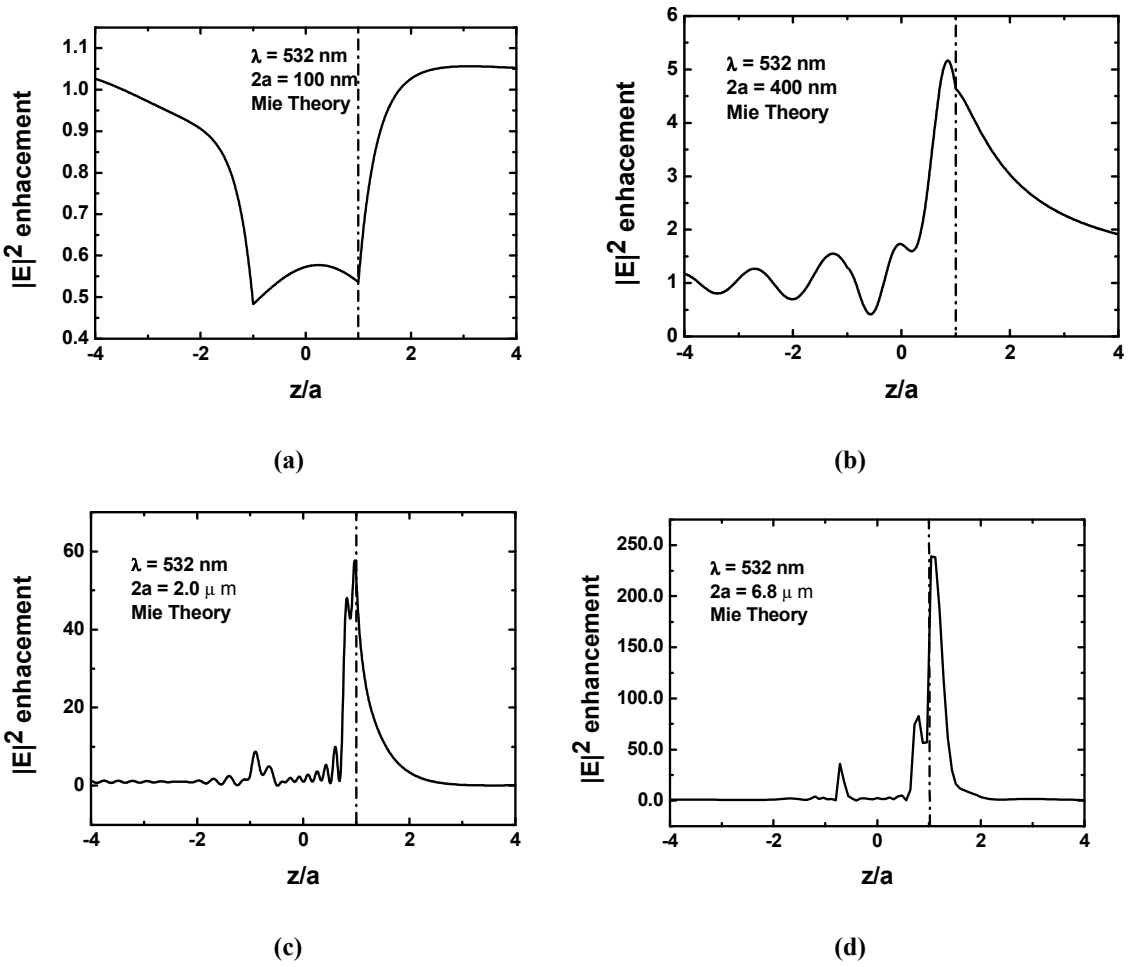

Figure 4.4 Distribution of laser intensity $I = |E|^2$ inside and outside the particle with different particle sizes of (a) $2a$ = 100 nm, (b) $2a$ = 400 nm, (c) $2a$ = 2.0 μm nm and (d) $2a$ = 6.8 μm under a same laser wavelength of 532 nm. Particle is considered to be nonabsorbing (κ = 0) with refractive index n = 1.6. Background media is vacuum. Intensity is understood as a square of the electric vector.

As the radius of the sphere is increased, there is a departure from symmetry, more light being scattered in the forward direction than that in the opposite direction. This phenomenon is often called the Mie effect. As the radius is increased still further, practically all the scattered light appears around the forward direction; likewise for a

conducting sphere there is a greater concentration of light in this direction. When the radius of the sphere is very large compared to the wavelength for most of the incident light, however, reflected, as from geometrical optics.

Actually, the calculation shows that even using 10 μm diameter particle, the enhancement laser energy will still be confined in an area with only 450 nm diameter. This technique has a potential to be applied to nanomachining on transparent material in optical near field with tens micrometers lens.

Figure 4.5 shows the distribution of intensity along the *z*-axis of the 1.0 μm particle for radiation with λ = 248, 355, 532 and 800 nm. Particle is also considered to be nonabsorbing with refractive index n = 1.6. One can see that the maximal intensities (outside of the particle) decrease with wavelength.

In the view of above cases, the optical enhancement under the particle can be by the order of magnitude higher than the incident intensity. The enhancement is sensitive to the particle size and incident laser wavelength. A size parameter $q = 2\pi a/\lambda$ is defined. Small variations in size parameter can lead to big variations in enhancement intensity. It should be noted that the used silica particles in our experiments have a size deviation of 10%, which corresponds to a variation in size parameter q ($q = 2\pi a/\lambda$) from 3.54 to 4.32. Figure 4.6 presents the optical near-field enhancement under the particle as a function of q. As it can be seen, the enhancement is about 10 times for q = 3.54 ($2a$ = 902 nm) while 15 times for q = 4.12 ($2a$ = 1050 nm), which shows an oscillation [108]. It is clear that the

difference in enhancement factor affects the formation of nano-crater under the same

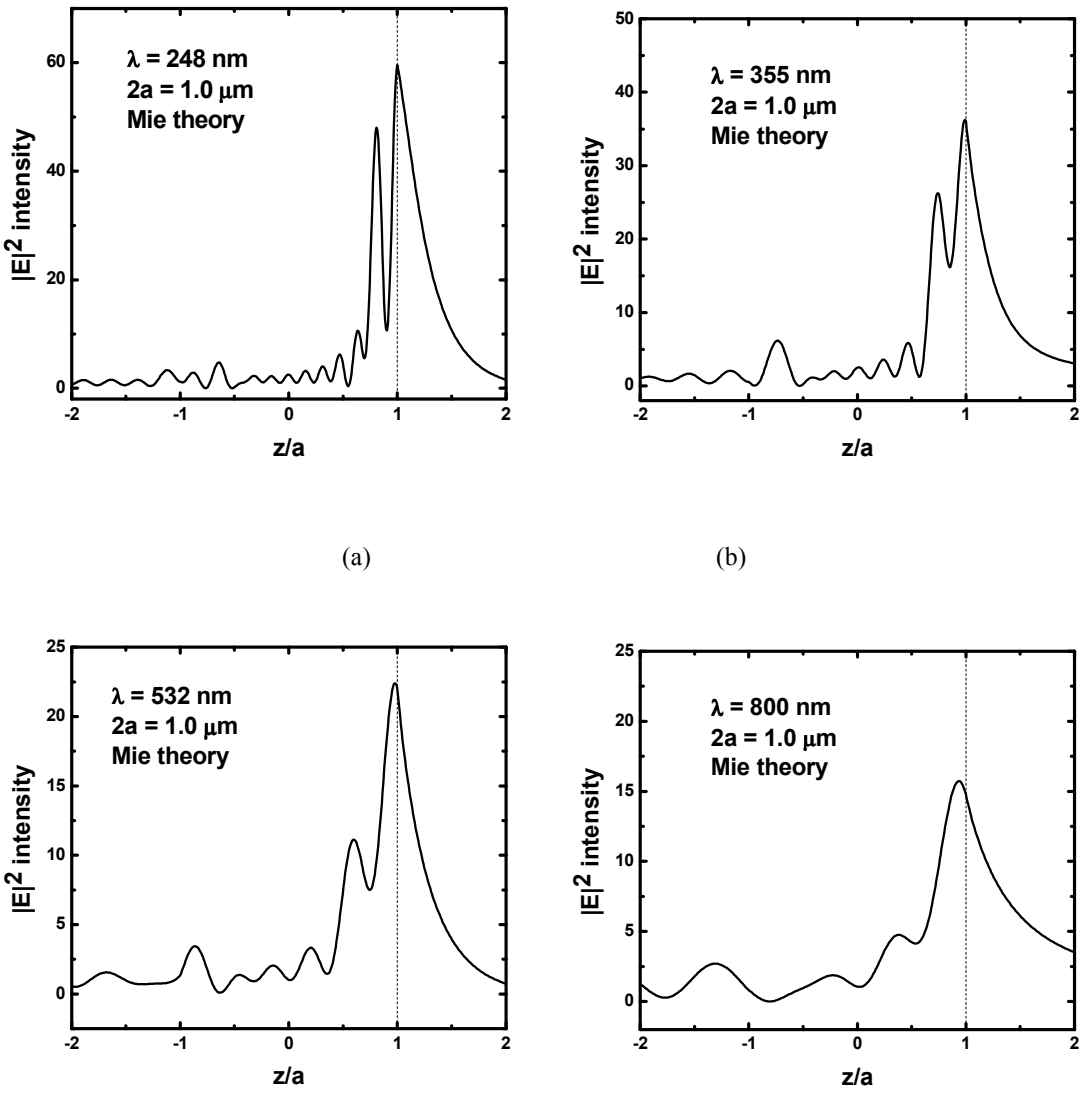

Figure 4.5 Distribution of laser intensity $I = |E|^2$ inside and outside the particle with radius $2a$ = 1 μm for different radiation wavelength λ. Particle is considered to be nonabsorbing ($\kappa = 0$) with refractive index n = 1.6 for all wavelengths. Background media is vacuum. Intensity is understood as a square of the electric vector.

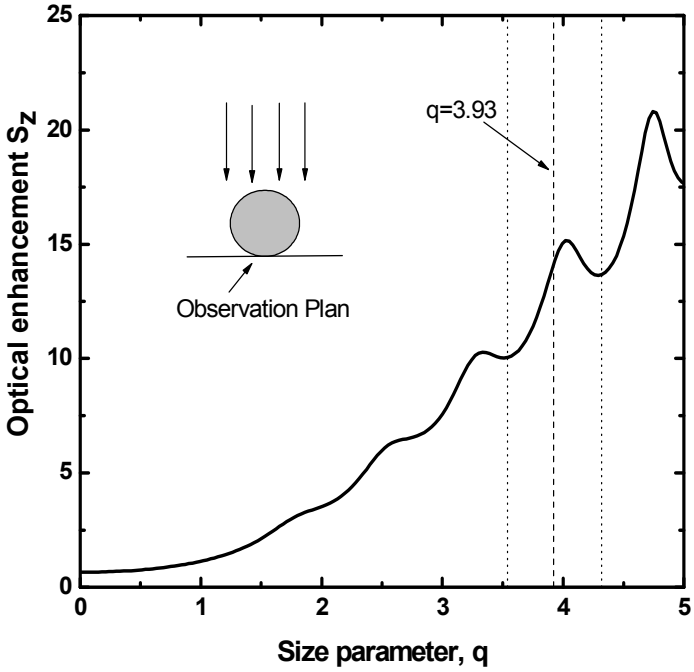

Figure 4.6 Variation of the optical near-field enhancement under the particle as a function of particle size parameter. The silica particle is considered as non-absorbing materials for the laser light with a refractive index of 1.6.

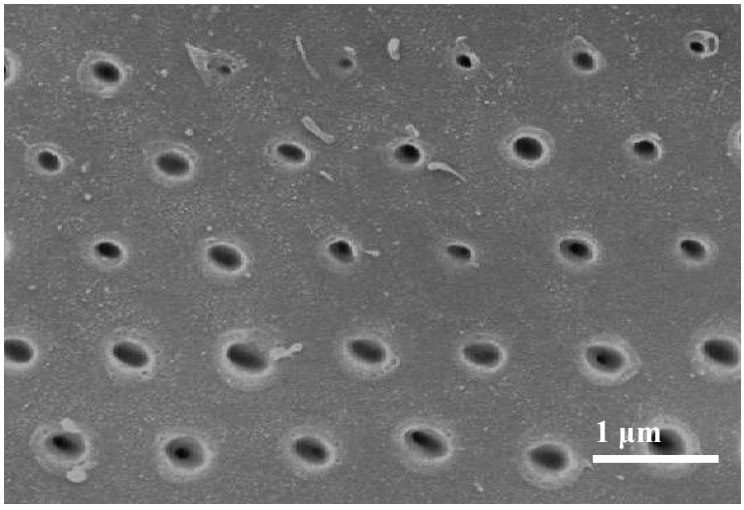

Figure 4.7 The nano-craters sizes variation under glass substrate surface.

laser fluence irradiation, and this could be used to explain why the nano-craters have different sizes in diameter. It can be clearly seen in Fig. 4.7, where size variation in the nanopits was bigger than 30% although variation of the particle size was smaller than 10% because the difference in the enhancement factor strongly affects the formation of nanopits under the same laser fluence irradiation.

Naturally, the nanopits size depends on the particle diameter if the input laser fluence remains the same. The calculations of enhancement area size of full widths at half maximum (FWHM) and different laser wavelength are shown in Fig. 4.8 with the particle diameters of 1 μm, 2 μm, 4 μm, 6 μm, 8 μm and 10 μm respectively. It was found that for 1 μm and 2 μm particles, the FWHM sizes increase with incident laser wavelength. For other size particles, such relation can not be observed. While, the abrupt increase of FWHM size exists for all particles. This is due to the second order enhancement zone which can significantly enlarge the FWHM size. Increasing particle diameter further, the second order enhancement occupies much more laser energy resulting in the energy decreasing of first order enhancement zone or in other words, the first order enhancement zone was compressed. Then the FWHM size is shrunk pronouncedly. The jumping point moves right when laser wavelength increases which means that for longer wavelength the range of particle diameters for stable enhancement zone size is wider than near ultraviolet laser. Hence in the industry applications, to improve the size uniformity, red or near infra-red lasers are to be employed.

The dependence of the intensity of the scattered light on the size parameter is illustrated in Table 4.1 . The Mie effect may be clearly seen from the comparison of the first and

third rows. The table indicates a very rapid increase in intensity with increasing size of the sphere.

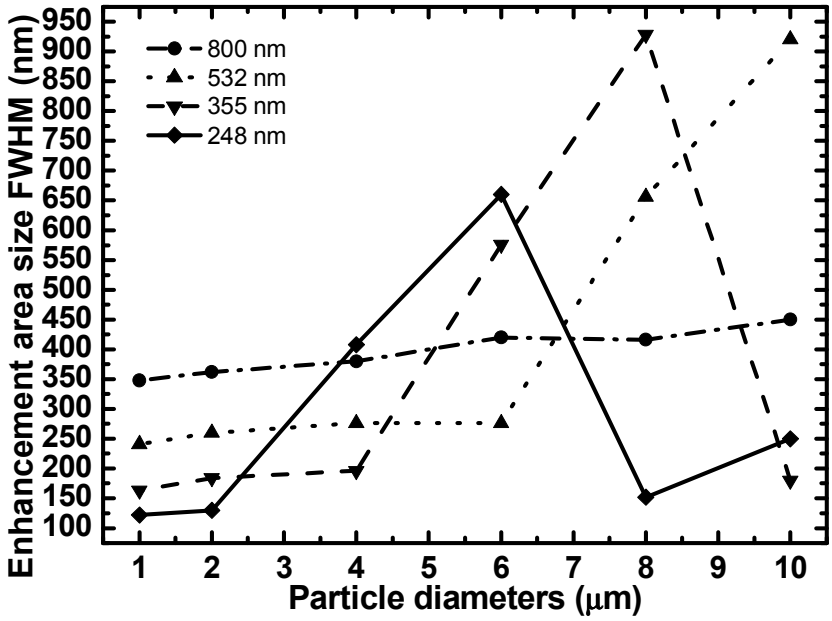

Figure 4.8 The FWHM size of enhancement zone with different particle sizes on the substrate surface.

Table 4.1 The normalized intensity of light scattered by dielectric spheres of refractive index n=1.25, as function of the size parameter q (Compiled from calculations in Ref. [109])

θ	q=0.01	q=0.1	q=0.5	q=1	q=2	q=5	q=8
0	5.0×10^{-14}	5.0×10^{-8}	1.2×10^{-3}	2.3×10^{-1}	4.3	980	7500
90^0	2.5×10^{-14}	2.5×10^{-8}	5.0×10^{-4}	3.6×10^{-2}	0.25	2.7	7.1
180^0	5.0×10^{-14}	4.9×10^{-8}	7.8×10^{-4}	1.9×10^{-3}	0.02	1.3	0.9

When q exceeds unity, i.e. when the diameter 2a of the spheres is greater than λ/π, there appears a series of maxima and minima, which at first are distributed irregularly. The appearance of a number of maxima and minima when q is large is in agreement with the Huygens-Kirchhoff theory.

As the radius of the sphere is increased, up to about $a = \lambda/\pi$, the maximum is displaced; in the majority of the cases that have been investigated the displacement is in the direction of larger θ for dielectric spheres and in the direction of smaller θ for absorbing spheres. When the radius of the sphere is increased still further, there appears an irregular sequence of polarization maxima. In the direction $\theta = 90^0$ the light is, for $q < 1$, almost completely polarized, with its electric vector perpendicular the plane of observation; for larger values of q this is no longer the case and the behavior becomes irregular.

It is noted that the wavelength enters our formulae only through the parameter q and through the refractive index n. in a sufficiently small range of wavelengths, n is practically independent of the wavelength if the conductivity σ is small, i.e. for a poorly conducting sphere. On the other hand, in the limit of infinitely high conductivity, n does not enter at all. In these cases the intensities of the spectral components depend on a/λ only. The effect of changing the wavelength is thus substantially equivalent to the effect that arises from changing the radius of the sphere by an appropriate amount. Since for different wavelengths the polarization maxima occur at different angles of observations, complicated color changes are seen when observations on scattered light are made through

a polarizing prism. This effect is called polychroism. The dependence of polarization of the scattered light on wavelength – know as dispersion of polarization- affords a very precise test of the theory [110].

The extinction curves for dielectric spheres of other refractive indices exhibit similar behaviors. It may be shown that if n is not too different from unity all the curves have a first maximum for a value of q give by $2q(n-1) \sim 4$.

4.2 Nanopatterning at different laser fluences

4.2.1 Substrate morphology change with laser fluence

To further investigate the effect of laser fluence on the formation of nano-craters, we repeated the experiments at different laser fluences. Figure 4.9 shows the SEM images of nano-patterns on the glass surface by laser irradiation on particle mask at fluence ranging from 17.5 to 61.3 J/cm^2. From Figs. 4.9(a) to 4.9(c), the nano-pattern shape does not change too much as the laser fluence increases from 17.5 to 35.0 J/cm^2. They are single-hole structure. It was found that the center-hole size was enlarged. However, the melting zones of the patterns are kept at the same size appoximately. A further increase of the laser fluence leads to a very interesting phenomenon: at a laser fluence of 43.8 J/cm^2, there are three linked holes inside each nano-crater as shown in Fig. 4.9(d). It was referred to as tri-hole crater. Compared with those structures at the lower laser fluence, the main difference is that there are two wing holes formed on both sides of the center-hole. And the melting

zone increases from 450 nm to 800 nm. The tri-hole nano-crater becomes more significant as laser fluence increases further to 52.5 J/cm^2 (as shown in Fig. 4.9(e)). The two wing holes grow much bigger while the center-hole changes from the original circular to the elliptical shape. Meanwhile, the melting zone is also in an elliptical shape. The orientation of major axis of nano-crater is perpendicular to nano-hole major axis. When the fluence increases further to 61.3 J/cm^2, the whole area is damaged as shown in Fig. 4.9(f). In contrast, glass substrate without particle mask was irradiated at the same laser fluence. No damage was observed. It shows that particle-assisted near-field enhancement is the main mechanism for the formation of nano-craters.

Figure 4.10 is the relationship between the size of center-holes and melting zone as a function of laser fluence. Both center-holes and melting zone sizes increase with laser fluence while the melting zone increases faster than the center-hole. At a high laser fluence, the melting zone can be as large as the particle size of 1 μm. While the diameter of center-hole remains at about 300 nm.

It is observed that the edges of these nanostructures are free of cracks. This can be attributed to the ultra-short laser pulse. For a long pulse duration laser, the formation of cracks caused mainly by laser associated high temperature and high pressure [99]. The processing with ultra-short laser pulses essentially eliminates heat flow to surrounding materials due to the two-temperature model where the hot electron gas causes ablation of materials, while the lattice stays cool at a significantly lower temperature. Therefore, thermally induced substrate crack is prevented.

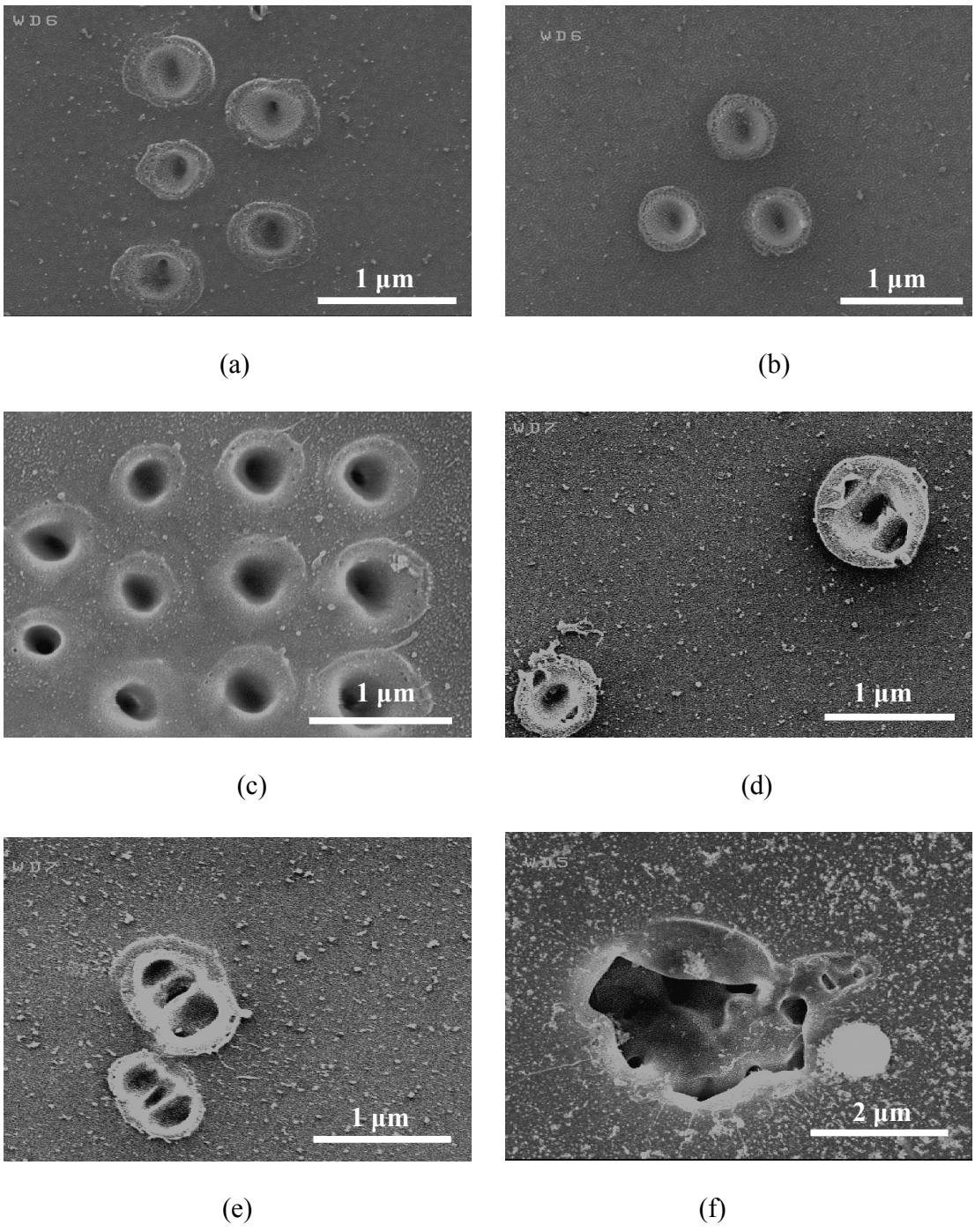

Figure 4.9 SEM images of the patterns formed on the glass substrate after the laser irradiation at laser fluences of (a) 17.5 J/cm^2, (b) 26.3 J/cm^2, (c) 35.0 J/cm^2 (d) 43.8 J/cm^2, (e) 52.5 J/cm^2 and (f) 61.3 J/cm^2.

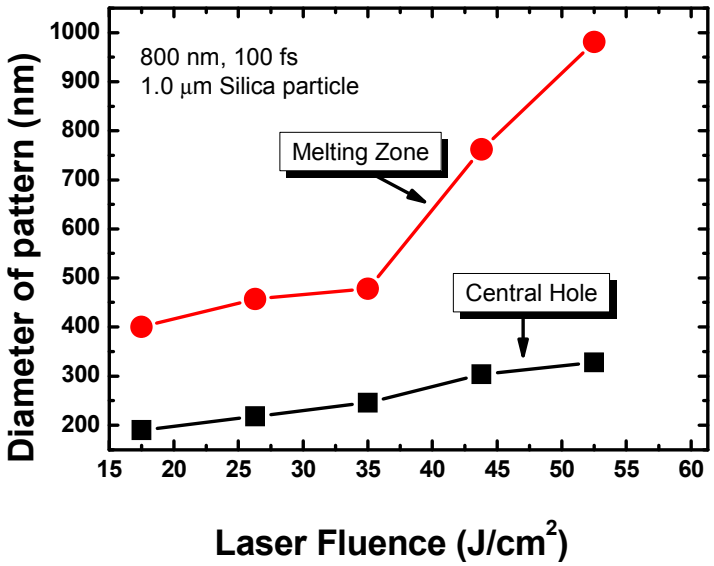

Figure 4.10 Average size of nano-craters as a function of laser fluence.

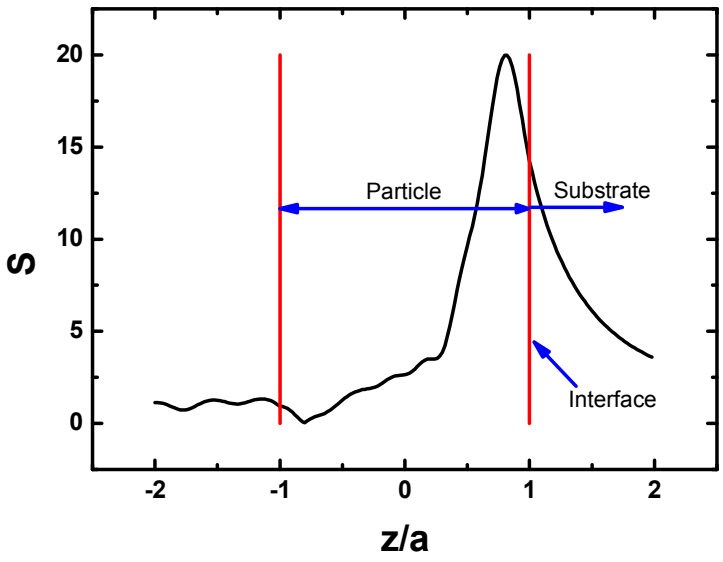

Figure 4.11 Normalized poynting intensity distribution along *z* axis under a silica particle (a = 0.5 μm) by 800 nm femtosecond laser irradiation based on Mie theory.

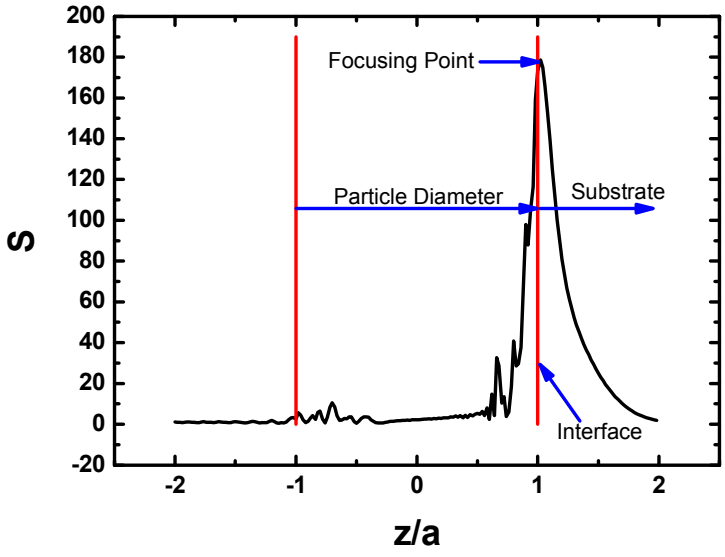

Figure 4.12 Normalized poynting intensity distribution along *z* axis under a silica particle(a = 3.42 μm) by 800 nm femtosecond laser irradiation based on Mie theory.

4.2.2 Focusing point position of spherical particle

Meanwhile, much debris was observed when increasing the laser fluence. Some of them was resulted from the high fluence laser ablation of the glass substrate. Figure 4.11 is the normalized poynting intensity distribution along *z* axis under a silica particle (a = 0.5 μm, *n* = 1.6) by 800 nm femtosecond laser irradiation based on Mie theory. It indicates that the maximum enhancement (focus point) is located in the interior of the particle. Hence, if nanopits can be formed on glass substrate surface, the laser intensity inside the silica particle is definitely larger than the damage threshold. Then during the laser irradiation, the particle exploded into pieces. Some of the ablation debris comes from the exploded silica particles due to that highly localized field inside the sphere. A possible way to

reduce the debris is to use bigger particles. For comparison, silica particles with the diameter of 6.84 μm (Bangs Laboratories, Inc.) were used to check whether there would be debris or not under bigger size particles. Theoretical calculation predicts that the focusing point moves outward as the size of particle increases. Figure 4.12 is the normalized poynting intensity distribution along *z* axis under a silica particle (a = 3.42 μm, *n* = 1.6) by 800 nm femtosecond laser irradiation based on Mie theory. The focus point was found at the interface between particle and substrate surface. Figure 4.13 presents the image of substrate surface after the femtosecond laser irradiation. The craters formed hexagonally closely packed array on the glass surface with the spacing of 6.84 μm which is the diameter of particles applied. No debris was found except the particles in the center ejected from other locations which were diameter of craters is 400 nm is 100 nm bigger

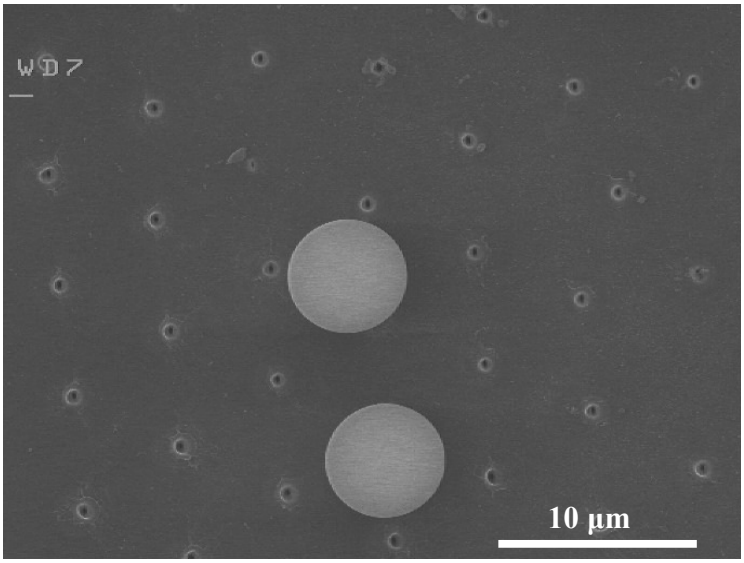

Figure 4.13 SEM image of substrate surface after femtosecond laser (100 femtosecond, 800 nm) irradiation of self-assembly 6.84 μm silica particles.

in their integrity. The profile of the crater measured by AFM indicates that average which

than those formed under 1 μm particle mask while the depth remains the same at about 150 nm.

4.2.3 Three-hole structure formation

As for tri-hole new phenomenon, laser energy redistribution induced by refraction index change was proposed as the formation mechanism. One should mention that 3D profile of laser intensity scattered by spherical particle yields a complex pattern, related to caustic diffraction catastrophes [111]. A well-known example is the Airy pattern, which is discussed due to its relation to super-resolution near field structure. We have found previously [112] a pattern with additional holes around the basic central maximum under the spherical particle using nanosecond laser pulses. With higher laser intensity this pattern can be complicated additionally due to non-linear absorption effects.

In Fig. 4.14 the normalized distribution of the z-component of the Poynting vector (optical enhancement $S_z = I/I_0$) is shown. Here I_0 is the input laser intensity. Parameters which were used in calculations correspond to the experiment: particle diameter 2 a = 1 μm, laser wavelength λ= 800 nm and refraction index for particle and glass n = 1.6. One can see from the figures that maximal laser intensity is localized within a small region near the particle-substrate contacting point and the size of this central region of enhanced intensity is about 300 nm in good agreement with experimental measurement. Modification of the hole shape can be qualitatively understood considering some threshold intensity $I > I_{tr}$ necessary to produce hole structure. With higher input intensity I_0 the

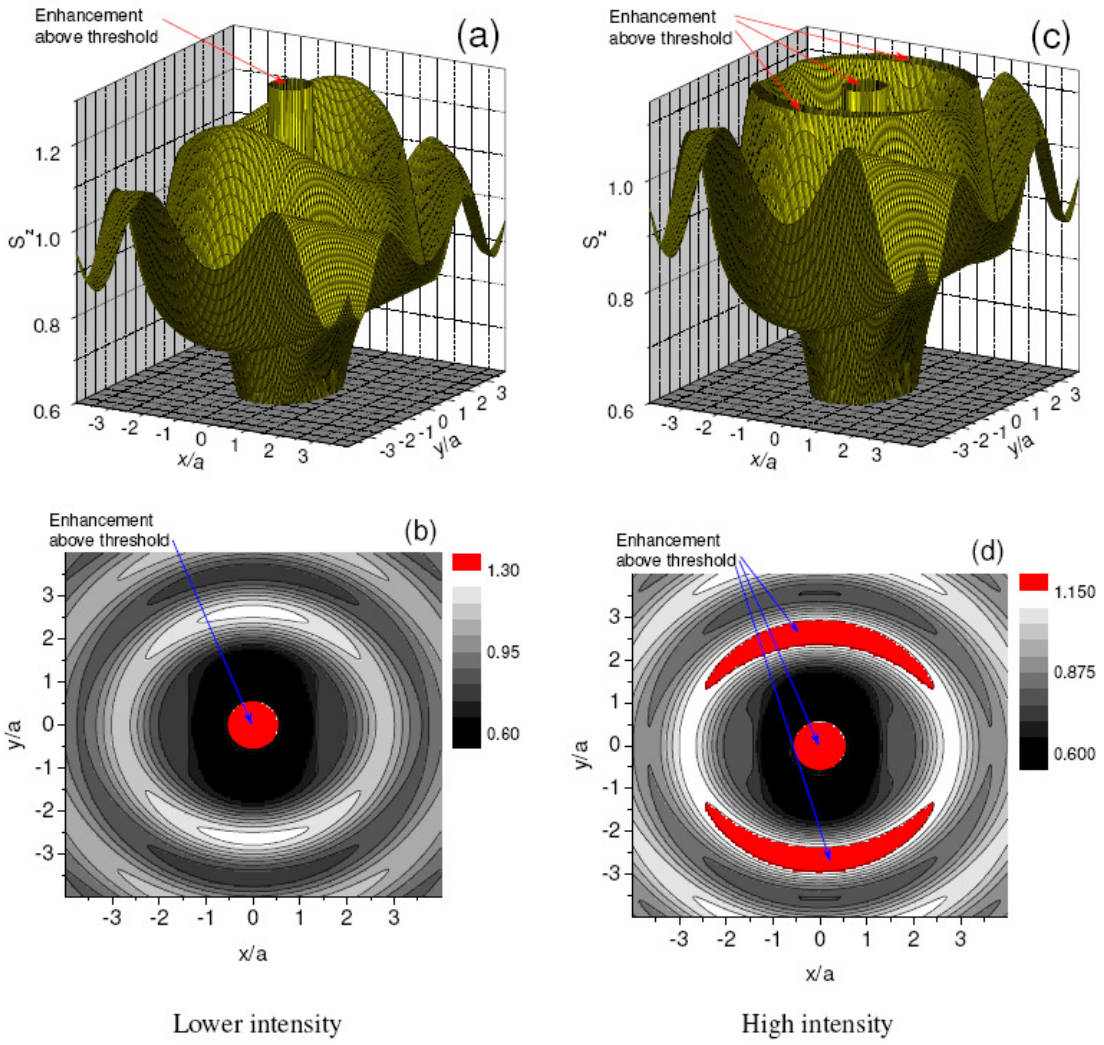

Figure 4.14 Calculated enhancement in intensity distribution (z-component of the Poynting vector), $S_z = I/I_0$, on the glass surface under a 1.0 μm Silica particles (n = 1.5 for λ = 800 nm). 3D pictures (a) and (c) present intensity distributions, where the top of the pictures corresponds to certain threshold for slightly different input intensity I_0. The same distributions are also shown in contour plots (b) and (d). The right pictures correspond to input intensity I_0, which is 13% higher than input intensity I_0 in the left pictures.

modification of the holes structure appears at smaller $S_z = I_{tr}/I_0$ value. One can see from Figs. 4.9(a) to 4.9(b) that a single crater is created at small intensity, while with higher intensity the tri-hole structure is created, as shown in Figs. 4.9(c) to 4.9(d). The side arcs in the intensity distribution become longer with further increase of input intensity and finally they form ring around the basic maximum in the centre. In experiment, we saw the whole region destroyed at a high fluences as shown in Fig. 4.9(f). However, formation of the ring around basic maximum was found in experiment with the film of phase-change material [112]. We should mention also that the maximal intensity is quite sensitive to the particle size; small variations in size parameter can lead to big variations in this intensity. It can be clearly seen in Fig. 4.1(a), where variation in the crater size was 30% bigger although variation of the particle size was smaller than 10%.

4.3 Nanopatterns formed with oblique light irradiation

Besides normal incident laser, oblique laser irradiation was also included in the research. Figure 4.15 shows the patterns on glass surface after single femtosecond laser shot of 6.84 μm silica particles at a laser fluence of 1.3 J/cm^2 and 20^0 incident angle. From zoom-in image in Fig. 4.15(b), it can be found that the nanodent does not locate in the center but around 1 μm off the center. Theory calculation based on Mie theory is shown in Fig. 4.16. It is obvious that under the particle, hot point on glass surface has a bias distance of 0.3 a, where a is the radius of glass particle. Meanwhile the peak value of enhancement decreases from 178.6 at normal incident to 141.3 at 20^0 incidence. The outer ring was

formed due to the thermal deformation close to contact point between silica particle and glass substrate.

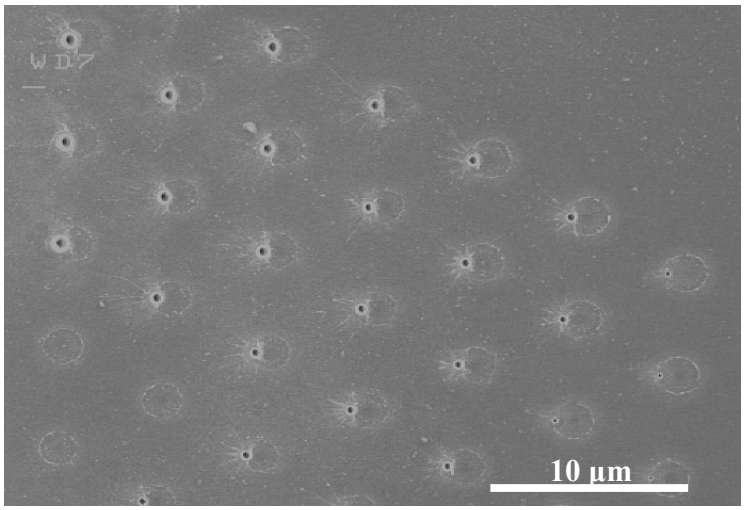

(a)

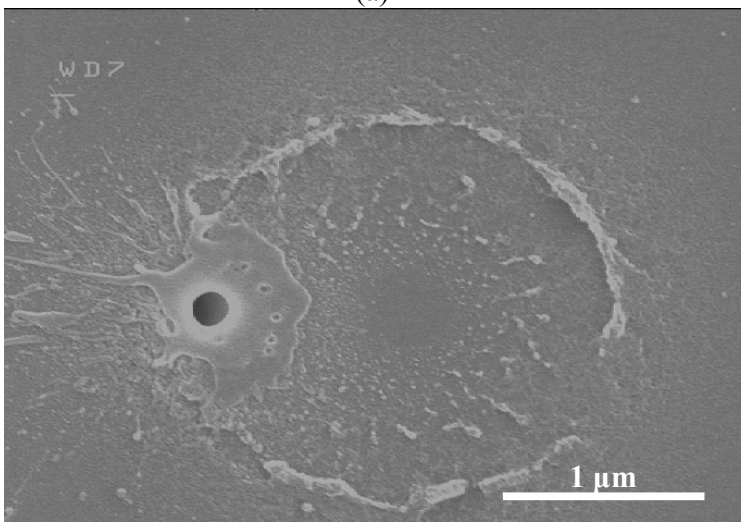

(b)

Figure 4.15 (a) Patterns on glass substrate surface under 6.84 µm glass particles by 800 nm femtosecond laser at a laser fluence of 1.3 J/cm^2, and (b) Zoom in image of single structure at the same sample. The incident angle is 20^0

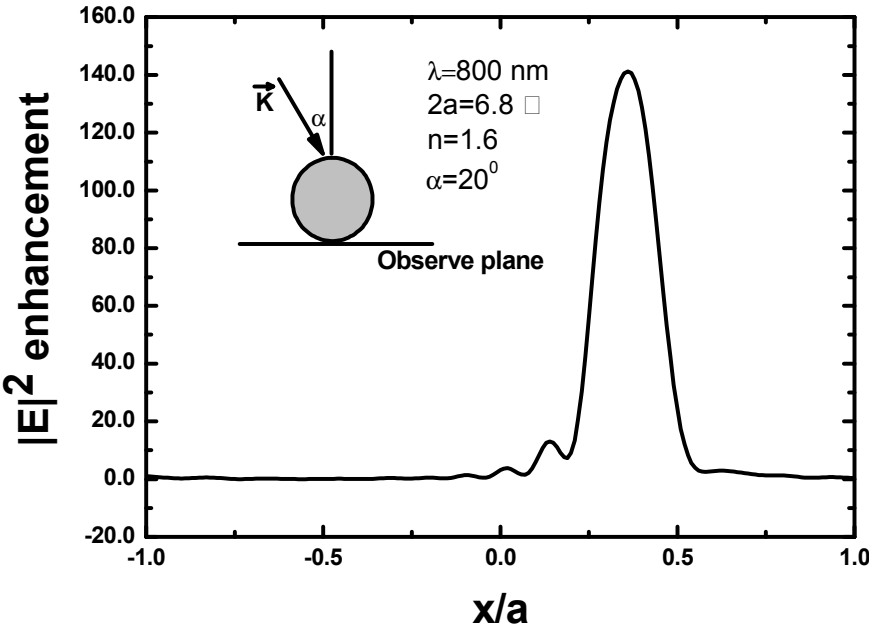

Figure 4.16 $|E|^2$ enhancement along x direction under glass particle with 20^0 incident angle calculated by Mie theory. Particle diameter 6.8μm, laser wavelength 800 nm, refractive index n = 1.6, and glass material was considered as non-absorptive.

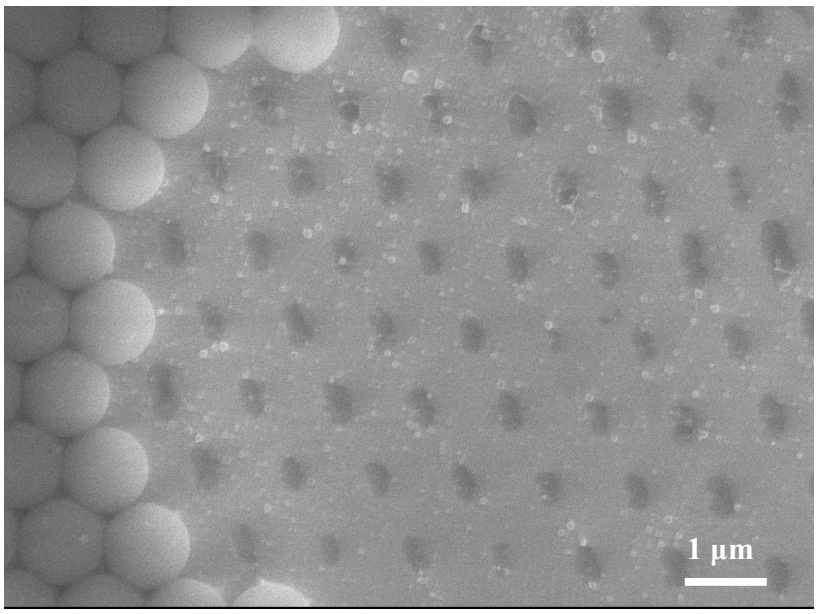

Figure 4. 17 Nano-dents on silicon surface after one pulse femtosecond laser irradiation at a laser power of 2.5 mW power through 1 μm glass particle mask.

4.4 Femtosecond laser nanopatterning of Si through silica particle mask

The nanopatterns on silicon wafer under 1 μm glass particle mask irradiated by single femtosecond laser pulse at a laser power of 2.5 mW is shown in Fig. 4.17. From the image, the glass particles were removed away from substrate surface. This effect can be potentially utilized in laser dry cleaning of transparent particles on transparent substrate. The detail can be seen in Chapter 6. It is clear that the absorption index of Si is significantly larger than transparent glass so that with a very low laser power, the nanodents could be formed, while with that low power deposited on glass surface with the same particle mask, the substrate is intact as shown in Fig 4.18 because of the non-effective coupling from transparent substrate.

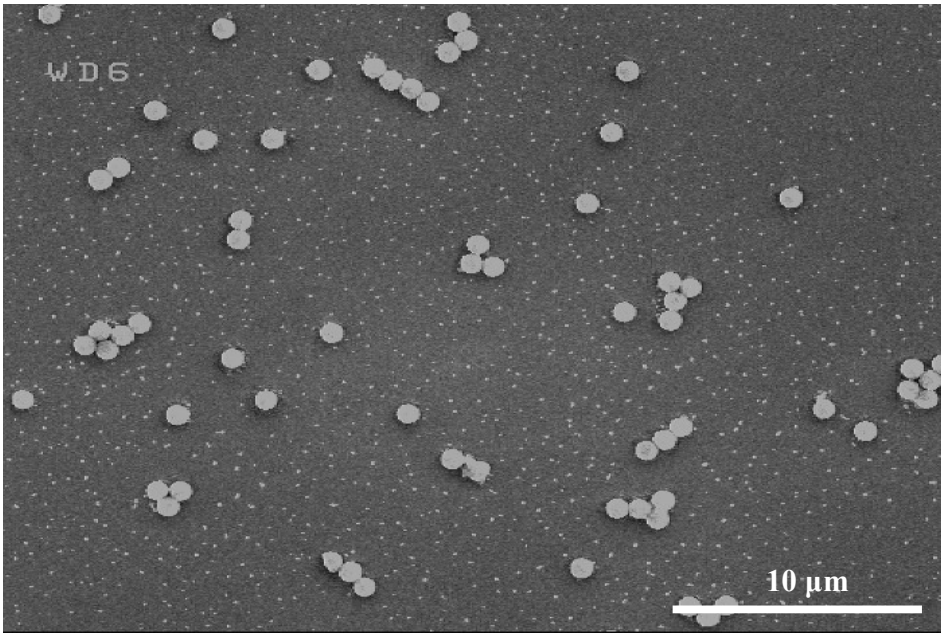

Figure 4.18 The glass surface after 2 mW femtosecond laser radiation on 1 μm glass particles.

As noticed before, Mie theory does not take into account the surface influence on the field distribution. Due to reflection and secondary scattering of the reflected radiation of the substrate, final field distribution in fact can be different.

Let a wave $\mathbf{V}^{in}$ (e.g. a plane wave) be incident on this system. If the sphere was absent, we could satisfy the boundary conditions at the interface between the ambient and the substrate by adding a wave $\mathbf{V}^{R}$ (just Fresnel reflection in the case of a plane wave). In the presence of the sphere, there will be an additional scattered wave $\mathbf{W}^{S}$ as a result of the displacement current flowing inside the sphere. But this wave will also be reflected by the substrate – i.e. inducing displacement current flowing inside the substrate and giving rise to a secondary reflected scattered wave $\mathbf{V}^{SR}$. The fields $\mathbf{V}^{SR}$ and $\mathbf{W}^{S}$, once again, should be linearly related by some matrix $\hat{\mathbf{A}}$, characterizing the reflection of sphereical waves by the substrate: $\mathbf{V}^{SR} = \hat{\mathbf{A}} \cdot \mathbf{W}^{S}$.

In Ref. [113, 114] authors used the expansion of inverse matrix, while in Ref. [115] some particular cases were analyzed: perfectly conducting substrate or far-field scattered field. Examples of practical calculations for Si particles on the silicon substrate were presented in Ref.[116]. They did the numerical calculation with the help of discrete numerical solvers for Maxwell equations. Although during the last decade, there was a big progress with these computation [117], the exact solutions are still interesting for practical calculations as a test problem for solution of Maxwell equations. In spite of the difficulties in numerical calculation, the situation is rather clear from the physical point of view. Qualitatively the substrate surface works like a mirror coupled with spherical resonator

(particle); it should lead to an increase in optical enhancement.

Chapter 5 Plasmonic resonance by metallic nanoparticles

Metal exhibits vagarious optical characteristics not only in bulk but also when they are finely divided. We may recall the brilliant ruby colors of gold whether in liquids or glasses. These phenomena are of great interest, as scattering, absorption and diffraction take place here side by side caused by plasmonic resonance effect.

5.1 Light scattering by Au nanoparticles

Photoresist (ma-P1205) was utilized to record scattering patterns by 40 nm Au nanoparticles. As the photoresist is only sensitive to UV light, a 325 nm He-Cd continuous wave laser was used. 500 nm thick photoresist was coated on glass substrate. Then the gold particle suspension was dropped on the photoresist. After 6 seconds exposure to the laser beam, the sample was dipped into developer (ma-D331) for 20 seconds. Figure 5.1 shows the resulted patterns on photoresist surface. The insert is an AFM image of the center part of a ring. The hole size is around 200 nm in diameter. It can be seen that the laser energy spreads out to circular regions of 4 ~ 10 μm at a laser power of 3 mW. It is hundreds of times larger than particle size.

To explain these micro-rings, the amplitude of intensity, $|E|^2$, on photoresist surface under 40 nm gold particles by the 325 nm He-Cd laser irradiation is plotted in Fig. 5.2. Under the particle, the localized area, “light point”, covers an area 5 times bigger than particle size (Φ = 40 nm). This enlarged area can be explained as the multi-reflection of the Poynting vector between the gold particle and the substrate, which results in a larger

affected zone on the contact area. Meanwhile, around the particle, it is obvious that the scattering wave can propagate at a distance as far as 200 times of particle radii determining the boundary of micro-rings. It can be seen that, according to the finite differential time domain (FDTD) calculation of aggregated 40 nm Au nanoparticles in Fig. 5.2, the enhancement factor induced by single gold nanoparticle is less than unit so that the background light would erase all the patterns during the exposure. Since the gold particles were not isolated but grouped randomly, the resulting field is the sum of all interfered scattering fields excited by gold particles and/or particle pairs. Practically, it is possible that the micro-rings in the experiment were formed from the accumulation effect.

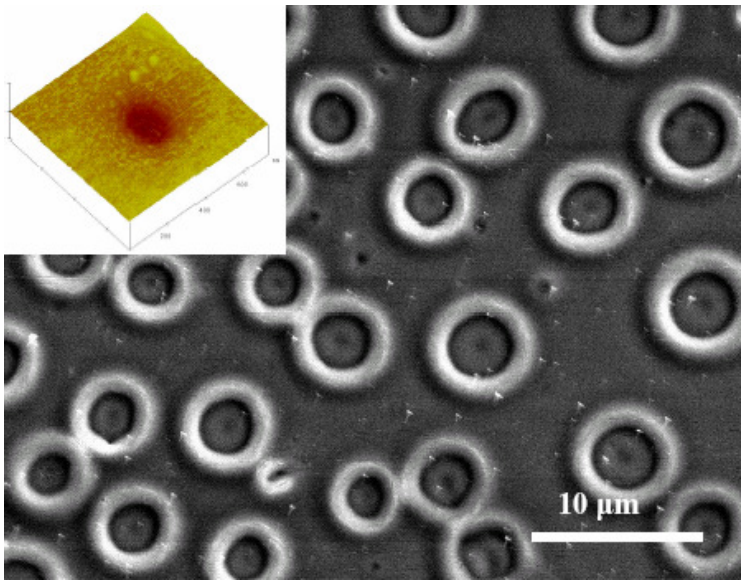

Figure 5.1 Micro-rings formed on photoresist surface after 325 nm He-Cd laser irradiation of 40 nmAu particles. The insert is an AFM image of central hole with the diameter ~ 160 nm.

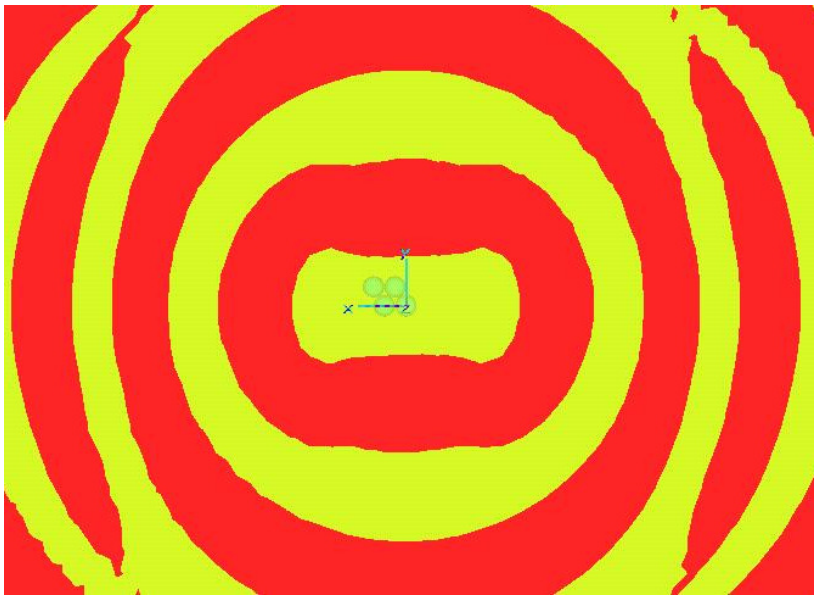

Figure 5.2 The contour plot of intensity, $|E|^2$, on photoresist surface under aggregated 40 nm gold particles illuminated by 325 nm He-Cd laser calculated with finite differential time domain technique.

It is of considerable practical interest to determine the total amount of light that is scattered by the sphere. This may be calculated by evaluating the Poynting vector and integrating it over all directions. With the help of the orthogonality relations that exist between the associated Legendre functions, it is possible to express the integrals in terms of the coefficients ${}^{e}B_{l}$ and ${}^{m}B_{l}$. These calculations, which are somewhat lengthy, were carried out in full in the paper by Mie.

5.2 Jumping triangular gold nanostructures due to light absorption

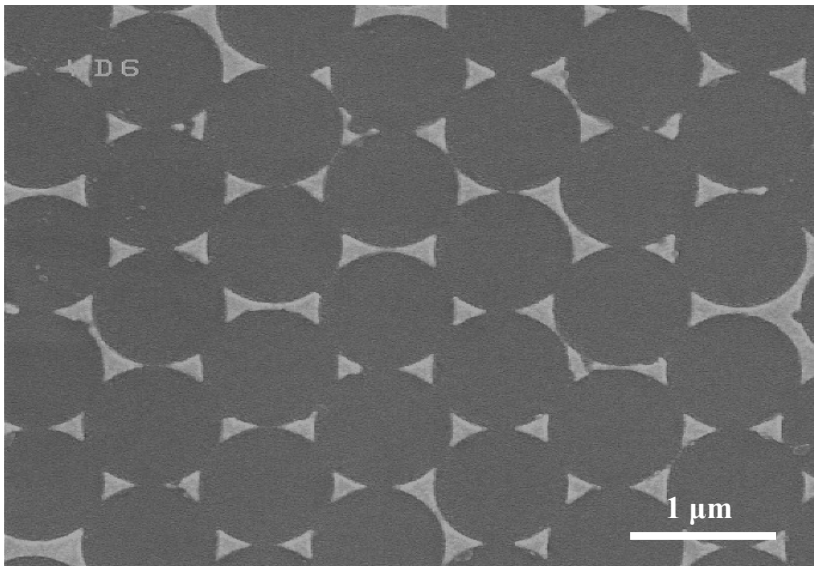

Figure 5.3 SEM image of triangular gold nanostructure on glass substrate as produced by colloidal monolayer lithography

Leiderer [118] in his Science paper considered that the basic driving force for jumping of gold nanostructure is created by dewetting process, which is dominant for melting of gold particles with initial triangular shape. However we saw these "jumping gold particles" for initial spherical shape in our experiments and we use this effect for laser cleaning (Chapter 6). In the research, jumping effect was related to efficient coupling of the surface Plasmon resonance with substrate surface. Dewetting process during melting also plays some role. And people well remember jumping oil droplets from the surface of frying pan but they are caused not by dewetting process only but also by recoil pressure of vaporized oil. For gold particles near the melting temperature vaporization do not play important role but dewetting process plays some roles. However the plasmonics coupling

also plays some roles. Naturally dewetting process is more important for triangular initial shape, because the higher surface energy release arises during conversion of triangular to spherical shape. In the case of spherical particles, it is less pronounced.

It is clear that dewetting process does not depend on the radiation frequency, it is not important by which wavelength you produce melting. So dewetting exists independently on radiation wavelength. In contrast, plasmon resonance coupling strongly depends on the wavelength.

Figure 5.3 repeats the triangular gold nanostructure array patterned on glass surface with microsphere lithography technique in Ref [118]. First, 1 μm silica particles were dropped on substrate surface to form self-assembly hexagonal closely packed monolayer. Subsequently, the monolayer was used as a mask for 40 nm Au deposition by e-beam evaporator. Finally, the silica particles were chemically etched and detached from substrate surface in a room temperature 10 % hydrofluoric acid (HF) solution.

From Figs 5.4 to 5.5, the gold nanostructure was illuminated by 355 nm single pulse which is off plasmonic resonance wavelength. It is clear that the nanostructures can jump both with and without melting. Thus, dewetting force induced by melting itself is not the only mechanism for particle removal even with triangular shape. Elastic forces can also play some roles in the particle removal that is proved by those triangle nanostructures jumped without melting in Fig 5.4.

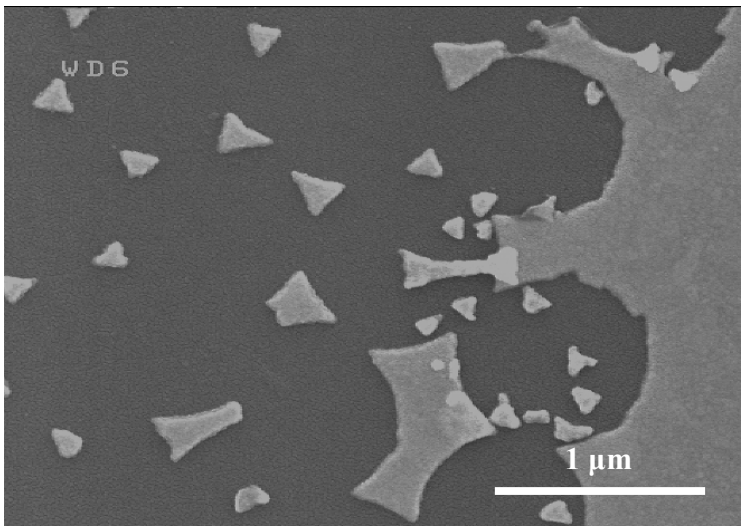

Figure 5.4 The jumping without melting triangular gold nanostructure on glass after single pulse Nd:YAG 355 nm laser illumination at a laser fluence of 17.8 mJ/cm^2.

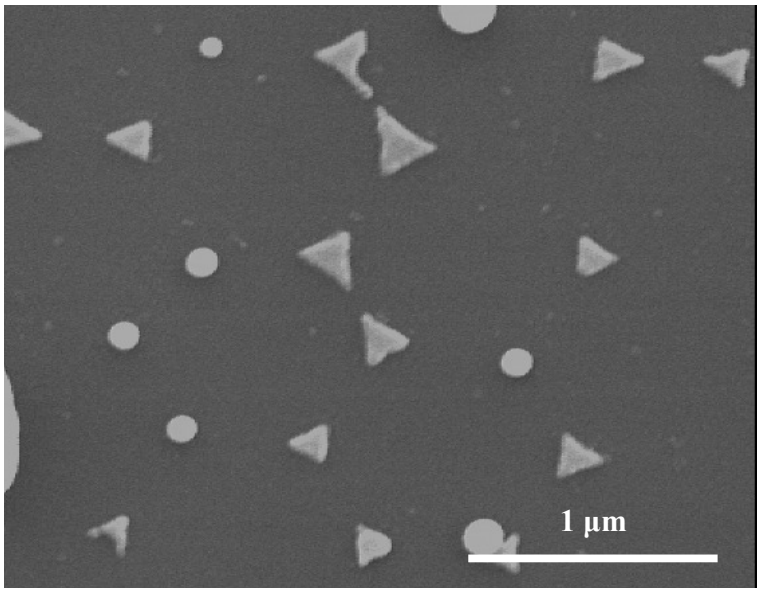

Figure 5.5 The melting without jumping triangular gold nanostructure on glass after single pulse Nd:YAG 355 nm laer illumination at a laser fluence of 17.8 mJ/cm^2 .

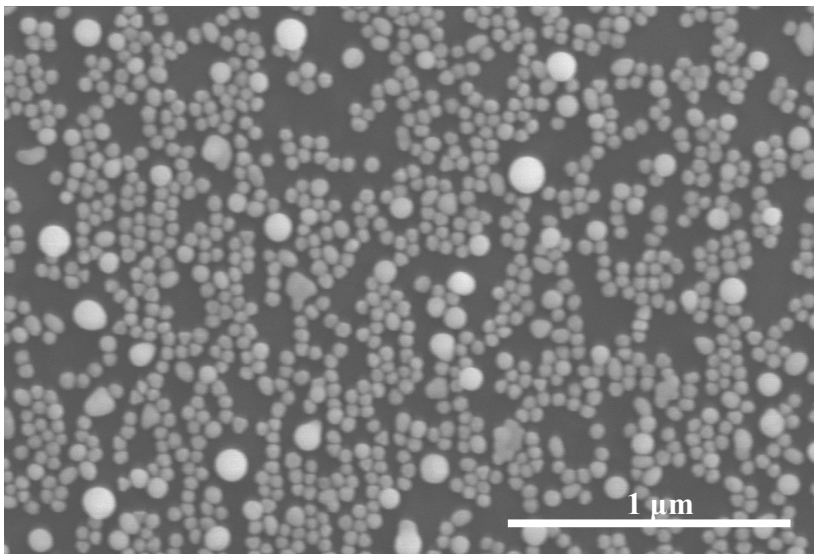

Figure 5.6 SEM image of 40 nm gold particles on Si surface after Nd:YVO_4 1064 nm / 7 ns laser annealing. Laser power 5.05W, repetition rate 30 KHz, scanning speed 400 mm/min

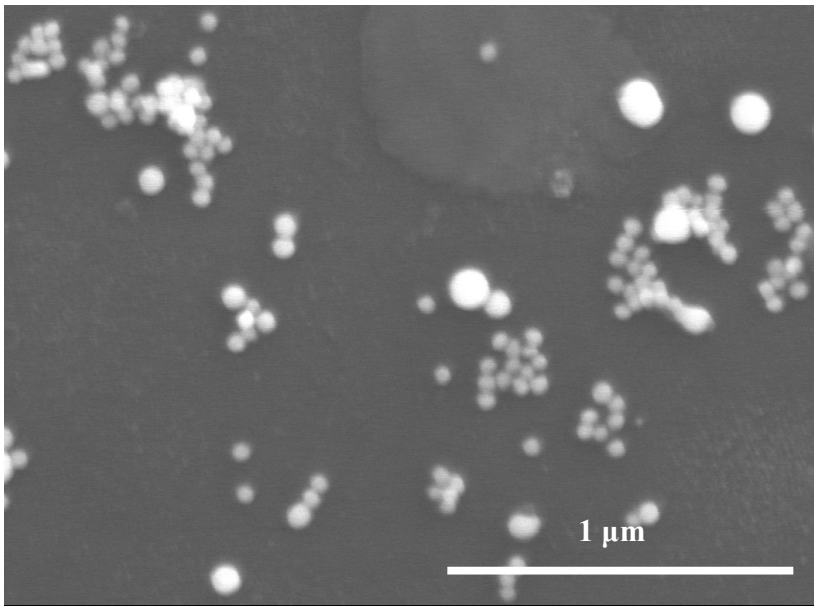

Figure 5.7 SEM image of 40 nm gold particles on Si surface after KrF 248 nm /23 ns single pulse laser illumination with 159 mJ pulse energy.

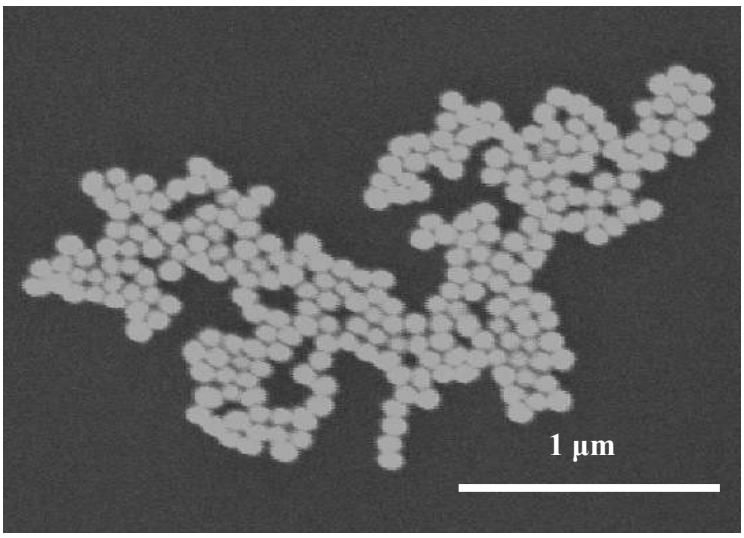

(a)

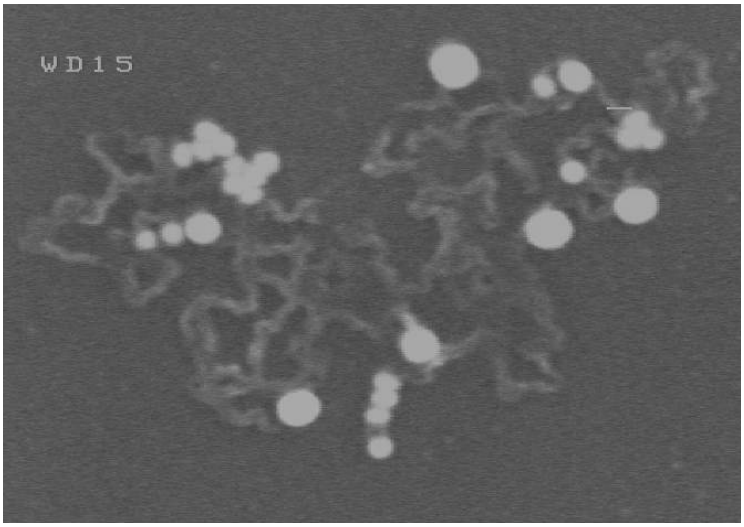

(b)

Figure 5.8 SEM image of (a) 40 nm gold particles on Si surface (b) after Nd:YAG 532 nm / 7 ns laser illumination. The laser fluence is 50 mJ/cm^2.

5.3 light absorption by 40 nm spherical Au nanoparticles

The SEM images of absorption of different wavelength laser energy by 40 nm gold

particles are shown from Figs. 5.6 to 5.8. We can conclude that for longer wavelength (1064 nm) the absorption is the lowest. For UV laser (248 nm) the absorption is intermediate. And for 532 nm laser, the absorption is the highest due to the plasmonic resonance effect.

Metal nanoparticles strongly absorb and scatter light at the plasmon resonance frequency. Since the color of most strongly colored substances is due to absorption, scattering is usually neglected thus the change in transmission, the so-called extinction, is solely attributed to absorption. For metal particles with dimensions above 30 nm, scattering becomes very important.

Light scattering, absorption and extinction of particles are described by frequency dependent cross sections C_{sca}, C_{abs}, and $C_{ext} = C_{sca}+C_{abs}$. The amount of scattered light is then given by

$$I_{sca}(\omega) = \frac{I_0(\omega)}{A} C_{sca}(\omega) \tag{5.1}$$

if a particle is illuminated with the light intensity per area $I_0(\omega)/A$. Usually these cross sections are normalized to the particle's geometrical cross section (πr^2 for spherical particles with radius *r*) to give the so-called efficiencies Q_{sca}, Q_{abs}, and Q_{ext}. In the Mie theory, the scattering and extinction efficiencies are calculated by;

$$Q_{sca} = \frac{2}{k_m^2 a^2} \sum_{l=1}^{\infty} (2l+1)(|a_l|^2 + |b_l|^2) \tag{5.2}$$

$$Q_{ext} = \frac{2}{k_m^2 a^2} \sum_{l=1}^{\infty} (2l+1)\,\mathrm{Re}(a_l + b_l) \tag{5.3}$$

where k is the wave vector, a particle radius, l multipole extension of the fields, for dipole mode $l = 1$, and a_l, b_l Mie coefficients defined as

$$a_\ell = \frac{q_p \psi'_\ell(q_m)\,\psi_\ell(q_p) - q_m \psi_\ell(q_m)\,\psi'_\ell(q_p)}{q_p \varsigma'_\ell(q_m)\,\psi_\ell(q_p) - q_m \psi'_\ell(q_p)\,\varsigma_\ell(q_m)}, \quad q_m = k_m a = \frac{2\pi}{\lambda} a \tag{5.4}$$

$$b_\ell = \frac{q_p \psi'_\ell(q_p)\,\psi_\ell(q_m) - q_m \psi_\ell(q_p)\,\psi'_\ell(q_m)}{q_p \psi'_\ell(q_p)\,\varsigma_\ell(q_m) - q_m \psi_\ell(q_p)\,\varsigma'_\ell(q_m)}, \quad q_p = k_p a = \frac{2\pi n_p}{\lambda} a\,. \tag{5.5}$$

The absorption extinction efficiencies is

$$Q_{abs} = Q_{ext} - Q_{sca} \tag{5.6}$$

Figure 5.10 is calculated cross section efficiencies of 40 nm Au nanoparticle. The optical constants of Au materials were plotted in Fig. 5.9. The calculated results proved the experimental results that show the strongest absorption at plasmonic resonance frequency. Here it is around 510 nm.

The ratio of scattering to absorption changes dramatically with size. Large particles scatter light very efficiently, whereas the color of small particles is mainly caused by absorption.

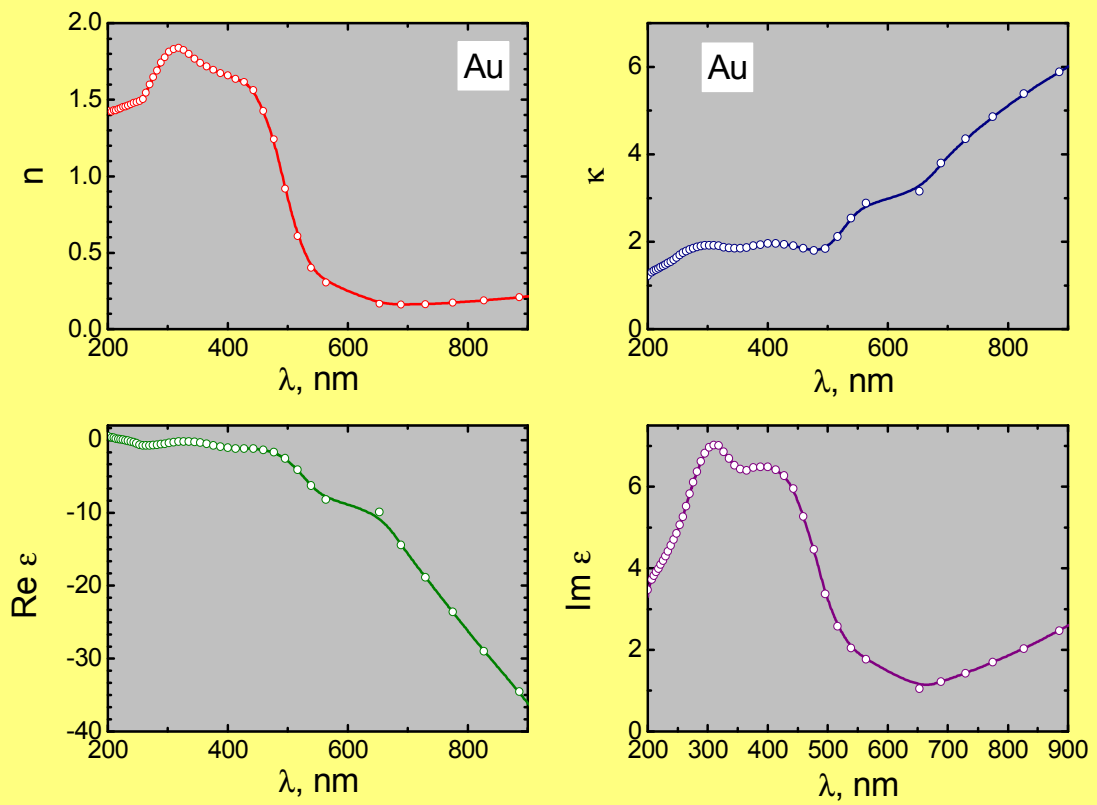

Figure 5.9 Optical constant of Au in visible range

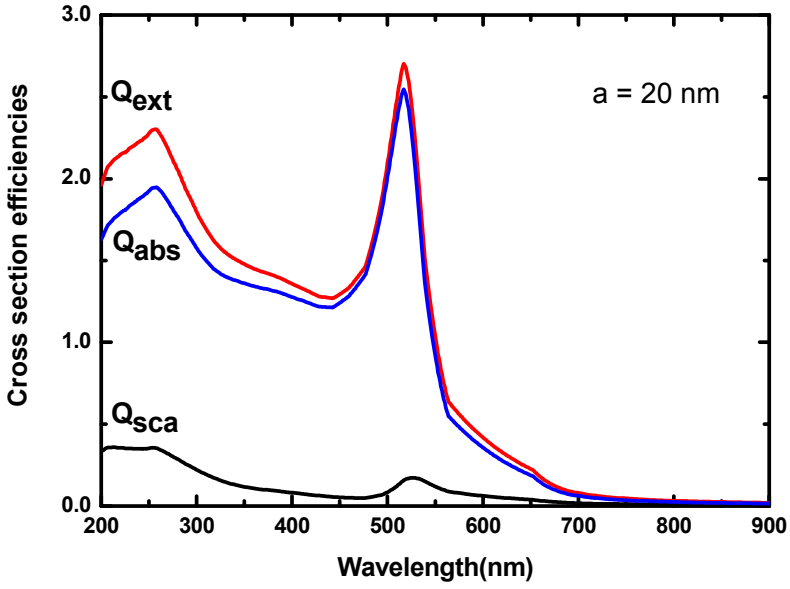

Figure 5.10 Extinction, absorption and scattering cross section efficiencies of a a = 20 nm Au particle in air. The efficiencies were calculated with Mie theory with the optical constants from Fig 5.9.

5.4 Light Scattering by nondissipative metallic nanoparticles near plasmon resonance frequency

According to the Rayleigh approximation, a small particle scattering light is a point dipole. The far field scattering polar diagram for dipole is presented by the well-known "8-shaped" distribution, which has been discussed in many books [4, 84]. Optical excitation of localized plasmons is accompanied by an inverse process - transformation of localized resonant plasmons into scattered light, resulting in the radiative damping [119, 120]. The Rayleigh approximation holds when this radiative damping is small compared to the usual dissipative one. In the opposite limit, when radiative damping prevails over the dissipative damping, the Rayleigh scattering is replaced by the anomalous light scattering [121], which results in sharp giant optical resonance and a complicated near-field structure of the Poynting vector field.

In fact this extraordinary scattering effect follows from the classical Mie theory. In the far field $l >> r$ (r is the distance from the particle centre), the radial component of the scattered radiation is negligible and the scattered diagram is defined by angular components $\left|E_{\theta}^{(s)}\right|^2 = I_{II}^{(s)} \cos^2\theta$ and $\left|E_{\varphi}^{(s)}\right|^2 = I_{\perp}^{(s)} \cos^2\varphi$, where the corresponding scattering intensities are presented by the asymptotic of the Mie formulae:

$$I_{II}^{(s)} = \frac{a^2}{r^2}\frac{1}{q_m^2}\left|\sum_{l=1}^{\infty}(-1)^l\left[{}^{e}B_l P_l^{(l)'}(\cos\theta)\sin\theta - {}^{m}B_l\frac{P_l^{(l)}(\cos\theta)}{\sin\theta}\right]\right|^2, \qquad (5.7)$$

$$I_{\perp}^{(s)} = \frac{a^2}{r^2}\frac{1}{q_m^2}\left|\sum_{l=1}^{\infty}(-1)^l\left[{}^{e}B_l\frac{P_l^{(l)}(\cos\theta)}{\sin\theta} - {}^{m}B_l P_l^{(l)'}(\cos\theta)\sin\theta\right]\right|^2 \qquad (5.8)$$

Here $P_l^{(l)}(\cos\theta)$ are the associated Legendre polynomials, and the stroke indicates differentiation over the entire argument of the corresponding function, i.e. $P_l^{(l)'}(z) \equiv dP_l^{(l)}(z)/dz$. Value $q_m = 2\pi a\sqrt{\varepsilon_m}/\lambda$ defines the so called size parameter which in the case is a small quantity, λ is the wavelength of the incident light in vacuum, ω its frequency, *c* light speed in vacuum, and *a* the radius of the spherical particle.

The attention should be drawn to the fact that formulas (5.7) and (5.8) follow from the exact solution of the Maxwell equations and they are valid for any size parameter *q* and any dielectric function. Far from the resonance, dipole scattering (*l* = 1) plays the dominant role. Also, for small particles, one can neglect magnetic amplitudes compared to the electric ones because of their total value is smaller in *q*. Thus, the amplitude $a_1 \approx -\frac{2i}{3}\frac{\varepsilon-1}{\varepsilon+2}q^3$ plays the dominant role. It yields the classical Rayleigh formula

$$Q_{sca} \approx \frac{8}{3}\left|\frac{\varepsilon-1}{\varepsilon+2}\right|^2 q^4 \tag{5.9}$$

This formula has singularity at the plasmon resonance frequency, when $\varepsilon = -2$. In reality, this divergence does not exist; it is stabilized either by dissipative processes or by the radiative damping at low dissipation rates. For nondissipative media, maximal values of the amplitudes are $a_l = 1$ and $b_l = 1$ at plasmon resonance frequencies. For small particles, if $\varepsilon \le 1$, only electric resonances occur. Thus, the true scattering efficiency for a nondissipative particle at exact resonance frequencies ω_l is given by the expression

$$Q_{sca} \approx Q_{sca}^{(l)} = 2(2l+1)/q^2 \tag{5.10}$$

where $Q_{sca}^{(l)}$ stands for the partial scattering efficiency. The Eq. (5.10) means that the resonance scattering cross section increases with an increase in order of the resonance l. This "*inverse hierarchy of resonances*" [121] is a remarkable feature, which disagrees with the conventional Rayleigh case dramatically. Eq. (5.10) also exhibits *inverse frequency dependence* – while in the Rayleigh case, the scattering cross section increases with an increase of frequency ($q \propto \omega$) as ω^4 , in the case given by Eq. (5.10), it decreases as ω^2 . The finiteness of the cross-section for a particle with zero radius obviously is an artifact related to the non-dissipative limit [122]. In reality, there is competition between the radiative damping and the one related to the dissipative losses. The necessary conditions for the anomalous scattering to take place may be found from the Mie theory, taking into account the dissipation factor ε'' in the denominator of the scattering amplitude. This consideration leads to the applicability condition

$$\varepsilon''(\omega_l) << \frac{q^{2l+1}}{l[(2l+1)!!]^2} \tag{5.11}$$

When this condition is fulfilled, the anomalous scattering is dominant. In the opposite case, the Rayleigh scattering is restored. The condition clearly explains numerical results found in Ref. [122]. Thus, under real experimental conditions, anomalous scattering can be realized just in some intermediate range of size parameter and only up to a certain order of the resonance: $l < l_{\max}$. We can illustrate this effect for metal, whose dielectric

permittivity is described by the Drude model.

Following Ref. [84], the scattering diagram in *xz* -plane ($\varphi = 0$) as a function of angle θ will be presented for two cases: linearly polarized light and nonpolarized light. The first case corresponds to the situation when the length of radius vector $I_{II}^{(s)}(\theta)$ presents the corresponding intensity. For nonpolarized light we can consider averaging $\left\langle \cos^2 \varphi \right\rangle = \left\langle \sin^2 \varphi \right\rangle = 1/2$; thus, the length of radius vector $I_{II}^{(s)}(\theta) + I_{\perp}^{(s)}(\theta)$ presents the corresponding intensity. In the case of the Rayleigh scattering amplitude a_l plays the dominant role. Thus

$$I_{II}^{(1)}(\theta) = \frac{a^2}{r^2 q_m^2} |a_1|^2 \frac{9}{4} \cos^2 \theta, \qquad I_{\perp}^{(1)}(\theta) = \frac{a^2}{r^2 q_m^2} |a_1|^2 \frac{9}{4} \tag{5.12}$$

This produces the universal "8-shaped" (or ∞- shaped depending on the definition of angle θ) angular distribution, which does not depend on the size parameter (at q << 1) or dielectric permittivity ε (Fig 5.11). Only the total intensity depends on these parameters. With anomalous light scattering, the polar diagram remains the same, one just should put in Eq. (5.12) $a_1 = 1$. The important point however is that for the anomalous light scattering, we also have pronounced higher order resonances for a small particle, e.g. quadrupole and octopole resonances, while in case of the Rayleigh scattering they are suppressed. At q << 1 these resonances are not overlapped and they have polar diagrams, which are presented at exact resonance frequencies by Eq. (5.7) and (5.8) with a single term, e.g. with $a_2 = 1$ for quadrupole resonance, or with $a_3 = 1$ for octopole resonance,

etc., namely:

$$I_{II}^{(2)}(\theta)=\frac{a^2}{r^2q_m^2}|a_2|^2\frac{25}{4}\cos^2 2\theta, \qquad I_{\perp}^{(2)}(\theta)=\frac{a^2}{r^2q_m^2}|a_2|^2\frac{25}{4}\cos^2\theta \tag{5.13}$$

$$I_{II}^{(3)}(\theta)=\frac{a^2}{r^2q_m^2}|a_3|^2\frac{49}{1024}(\cos\theta+15\cos 3\theta)^2, \quad I_{\perp}^{(3)}(\theta)=\frac{a^2}{r^2q_m^2}|a_3|^2\frac{49}{256}(3+5\cos 2\theta)^2 \tag{5.14}$$

For strongly dissipating (at the resonance frequencies) materials, e.g. for gold, amplitudes of partial resonances for small particle $q << 1$ are small $a_{i+1} << a_i << 1$ but the widths of the resonances are quite large. Overlapping of different resonances and their interference produce more complicated scattering diagrams. Some examples of that for gold nanoparticle are in Fig. 5.12.

With perfectly conducting material (conductivity $\sigma >> \omega$) or very large dielectric constant ($n_p >> 1$) the particle mostly produces backward scattering ("reflected" radiation). In spite of small q_m , the size parameter for the particle q_p cannot be considered as a small value. When both parameters q_m and q_p are small, the Rayleigh scattering yields the symmetrical diagram, shown in Fig. 5.12(a). As radius of the sphere is increased to $q \approx 1$, more light scatters in the forward direction (the so-called *Mie effect*).

Strong variations in scattered intensities can be found at different angles. Thus, weakly dissipating materials have very high *dispersion of polarization*. This effect can be used for different applications, e.g. optical recording. However it should be stressed that to have the effect pronounced one needs materials with weak dissipation near plasmon resonance

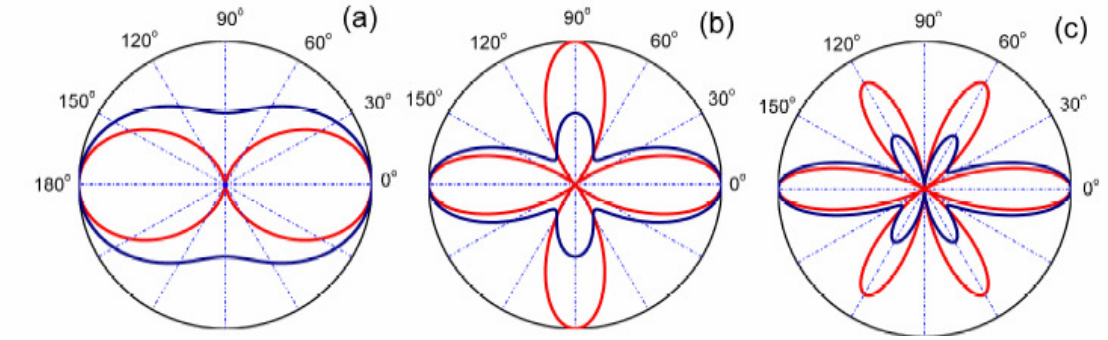

Figure 5.11 Partial polar scattering diagrams in xz -plane ($\varphi = 0$) for the electric dipole $l = 1$ (a), quadrupole $l = 2$ (b) and octopole $l = 3$(c) plasmon resonances according to Eqs. (5.12)-(5.14). Red lines correspond to linearly polarized light, navy to nonpolarized.

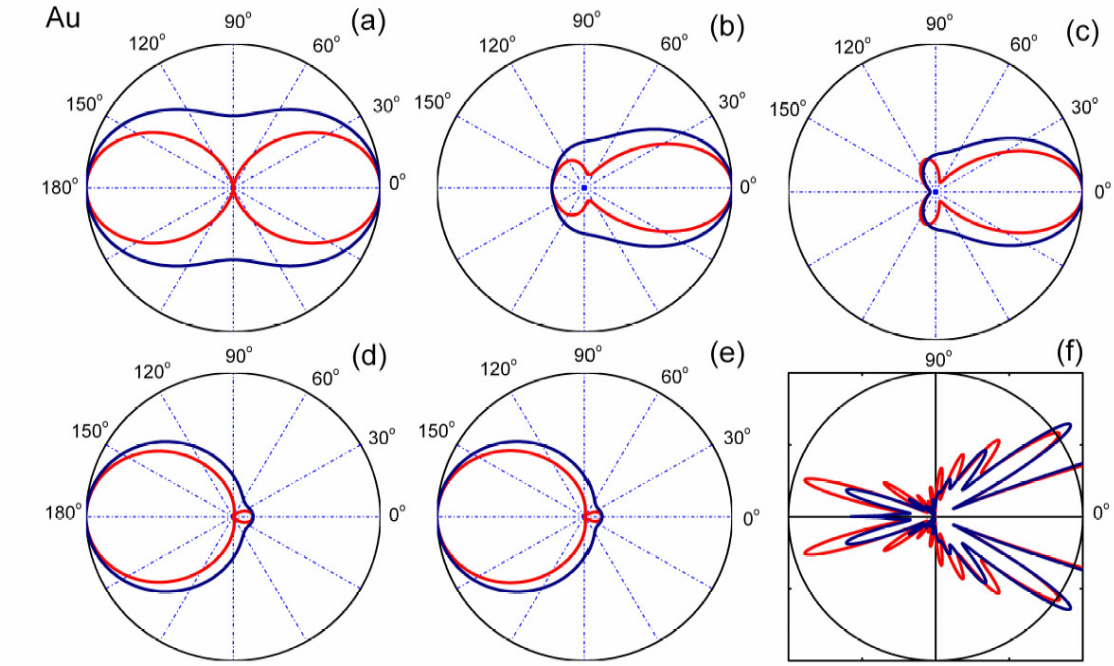

Figure 5.12 Scattering diagram for a gold particle, $n = 0.57 + i2.45$, in water for radiation wavelength $\lambda = 550$ nm. The radius of the particle a = 8.75 nm (a), 80 nm (b) and 90 nm (c), respectively. The corresponding size parameter $q_m = 2\pi a n_m / \lambda = 0.133$ (a), 1.215 (b) and 1.367 (c). Plot (d) presents a scattering diagram for a small particle a = 8.75 nm of highly conducting material $\varepsilon_p = \sqrt{i4\pi\sigma/\omega}, \sigma/\omega = 10^4$. Plot (e) represents a similar diagram with a large value of refractive index $n_p = 100$. The last picture (f) represents details of the scattering diagram for a large particle with $q = 10$ and refractive index $n_p = 1.5$. Vacuum as surrounding media, in the plots (d), (e) and (f).

frequencies. A possible candidate which might exhibit the discussed modifications in polar scattering diagram near quadrupole resonance might be an additively colored alkali halide crystal, e.g. potassium chloride. A small metal cluster of potassium produces the dipole scattering with the peak position at 730 nm. It agrees with our calculations in Fig. 5.13. The quadrupole resonance cannot be seen for a very small cluster because of its suppression by dissipation, see Eq. (5.11). However this resonance becomes pronounced at larger values of the size parameter. For example for a cluster with $a = 70$ nm the quadrupole resonance is quite pronounced and for $a > 90$ nm (in some range of sizes) the amplitude of this resonance is larger than that for the dipole resonance.

In Fig. 5.14 it can be seen that the shape of the scattering diagram practically does not change with variation of the incident light wavelength in the vicinity of dipole resonance (peak at 930 nm), but does change dramatically with its variation in the vicinity of quadrupole resonance (peak at 718 nm) from forward at $\lambda = 718$ nm to basically backward scattering at $\lambda = 758$ nm. This clearly indicates the mentioned *dispersion of polarization* near the quadrupole resonance for weakly dissipating materials.

An extraordinary scattering diagram can be found also for sodium nanoclusters immersed in a NaCl matrix, as well as for aluminum nanoclusters in vacuum. Many researchers have reported that the thermal heating-cooling process yields variation of the size of alkali-metal colloidal particles in the additively colored alkali halide crystals. Because of the extraordinary scattering effect this permits to use dispersion of polarization to write and read multibit information in nanoclusters with sub 100 nm range of sizes.

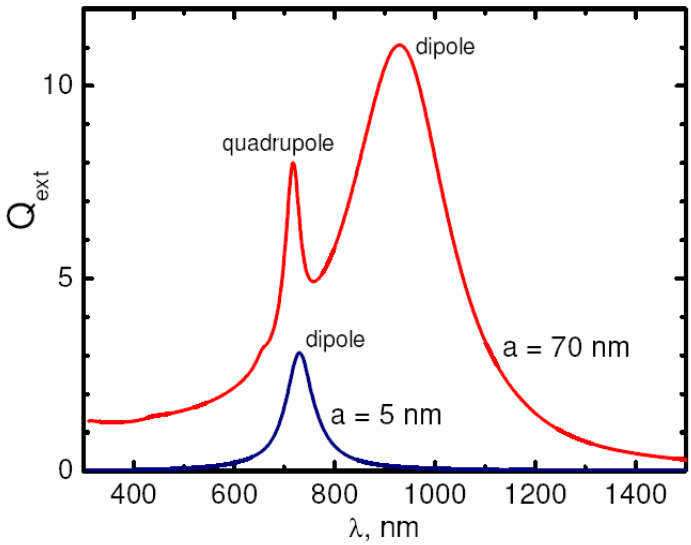

Figure 5.13 Spectral dependencies of extinction efficiency for K cluster in KCl matrix. Optical constants for both materials are taken from Ref. [123]. In calculations, the size effect renormalizing the collision frequency of free electrons due to their collisions with particle surface124, $\gamma \to \gamma_\infty + v_F / a$. Fermi velocity $v_F = 8.6 \times 10^7$ cm/s.

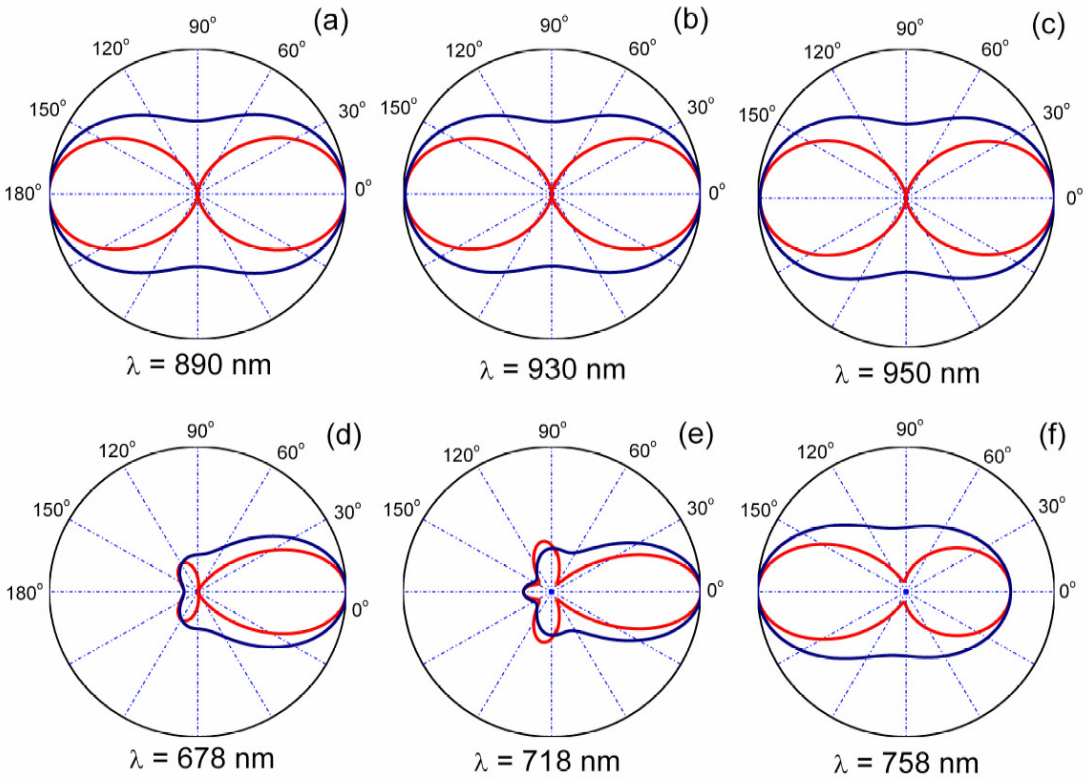

Figure 5.14 Scattering diagram near dipole (a, b, c) and quadrupole (d, e, f) resonances for a potassium spherical nanocluster with radius $a = 70$ nm immersed in a KCl matrix.

Chapter 6 Applications in dry laser cleaning

6.1 Adhesion of mesoscopic particles on the substrate

Particle adhesion on solid surface is mainly composed of three primary forces: electrostatic force, capillary force and Van der Waals force [125,126], as shown in Fig. 6.1. Two types of electrostatic forces may act to hold particles to surfaces. One is due to bulk excess charges present on the surface and/or particle that produces a classical Coulombic attraction known as an electrostatic image force.

The theory shows that the three forces are in proportional to the particle size *a*. A theoretical calculation shows that for micron-size particle, the Van der Waals force predominates over electrostatic force, as shown in Fig. 6.2. The capillary force can be clearly predominant over other forces for small particles.

It is reported that the absorbed water molecules can be retained around the contact area up to a temperature 180 ºC [127]. In the actual cleaning process, the substrate temperature is higher than 500 ºC, so that the first few pulses can adsorb the water molecules. Therefore, the Van der Waals force is the main adhesion force in dry laser cleaning.

Figure 6.1 Van der Waals Force Capillary Force Electrostatic Force

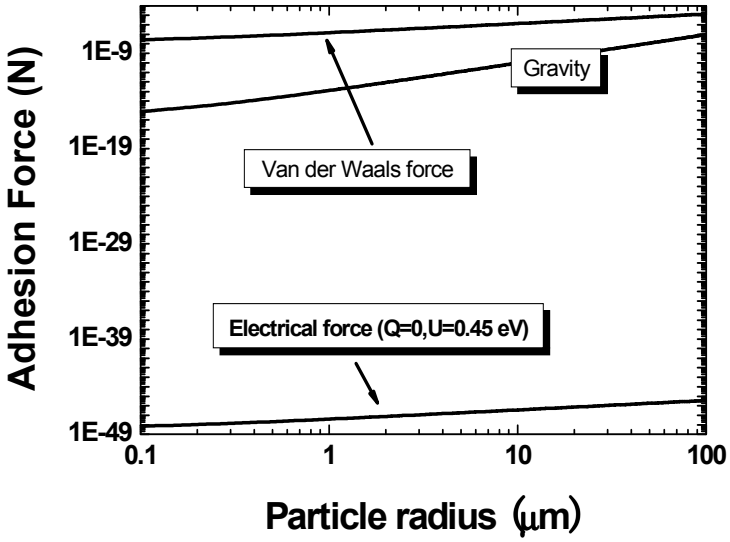

Figure 6.2 Van der Waals force in comparison to gravity and electrostatic forces as a function of particle radius.

6.2 Laser cleaning of transparent particles

In chapter 4, glass particles have been found to be removed from transparent glass substrate after femtosecond laser irradiation as shown in Fig. 6.3. The cleaning effect can be contributed to the surface acoustic wave generated by femtosecond laser energy deposition. As comparison, SEM image of glass particles after continuous wave 355 nm laser irradiation is shown in Fig. 6.4. Although the net energy deposited on particle is higher, particles remain on substrate surface with partial melting. This phenomenon can be considered from two aspects. One is the energy input and the other is laser pulse duration. In previous chapter, higher fluence of femtosecond laser pulse was applied, where nanopatterns were found on transparent substrate and glass particles were removed by

ejecting material flow. Hence energy input is not the only factor which influences the melting of glass particle. Pulse duration has to be included also. With continuous wave laser, energy has sufficient time to transfer through glass particles before the forming of strong elastic force due to the particle elastic transformation, which results in a high temperature in particle. And since the laser power is relatively strong, this temperature will be above glass melting point. The melting and flowing glass liquid changed the propagation properties that defocused laser beam. It is pure melting effect instead of cleaning effect with long laser pulse. As a result, particles can not be removed until higher laser power is applied. However, in the case the substrate surface should be damaged.

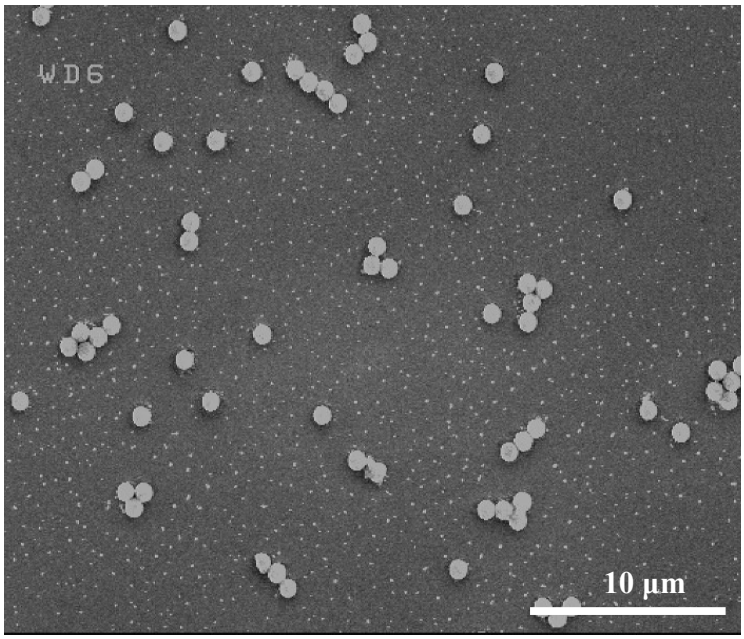

Figure 6.3 The glass surface after 2 mW femtosecond laser radiation on 1 µm glass particles.

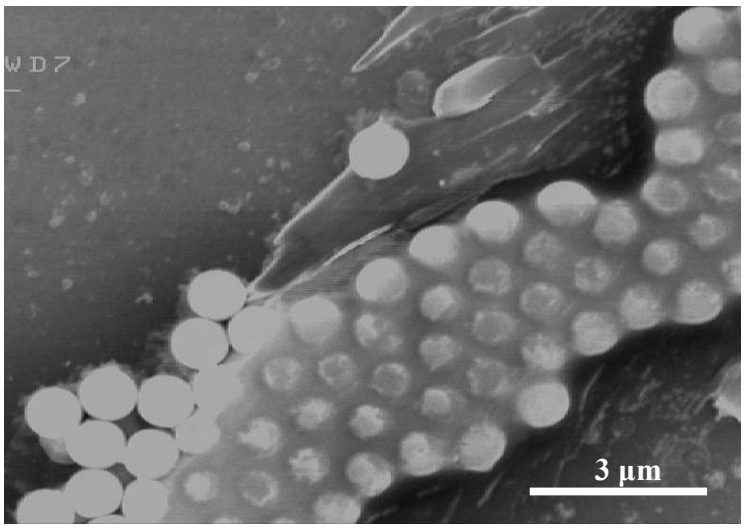

Figure 6.4 The glass particles on glass substrate after 355 nm continues wave laser illumination with at a laser power of 0.36W.

The demonstration of laser dry cleaning of glass particles on transparent glass substrate is shown in Fig. 6.5. The scratch line in the center is for marking purpose. It is clear that the cleaning efficiency is above 90% for only one run of scanning at the scanning speed of 400 mm/min.

Acoustic effects in laser cleaning were discussed previously. The acoustic effects in 1D case are probably important for weakly absorbing materials. The generation of surface acoustic wave can be modeled by a pressure pulse, $p(r,t)$, acting on the free surface of solid. Assuming a Gaussian distribution:

$$p(r,t) = p_0 \exp\left[-\frac{r^2}{r_a^2}\right]\exp\left[-\frac{t^2}{t_0^2}\right], \tag{6.1}$$

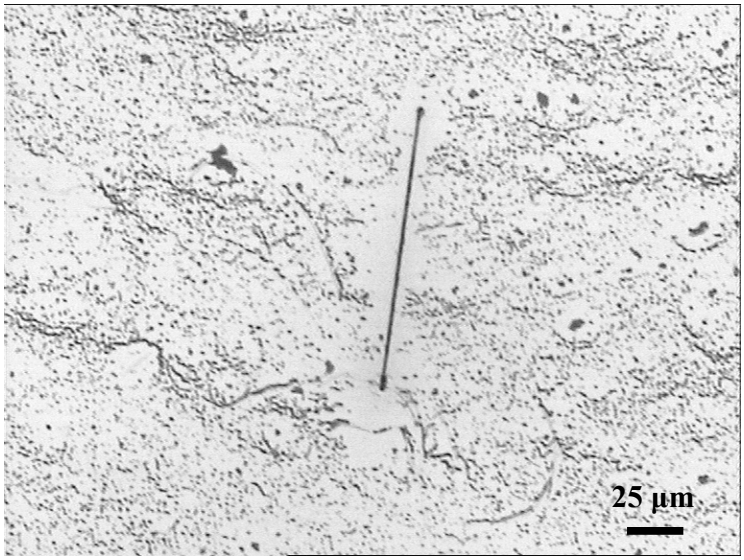

(a)

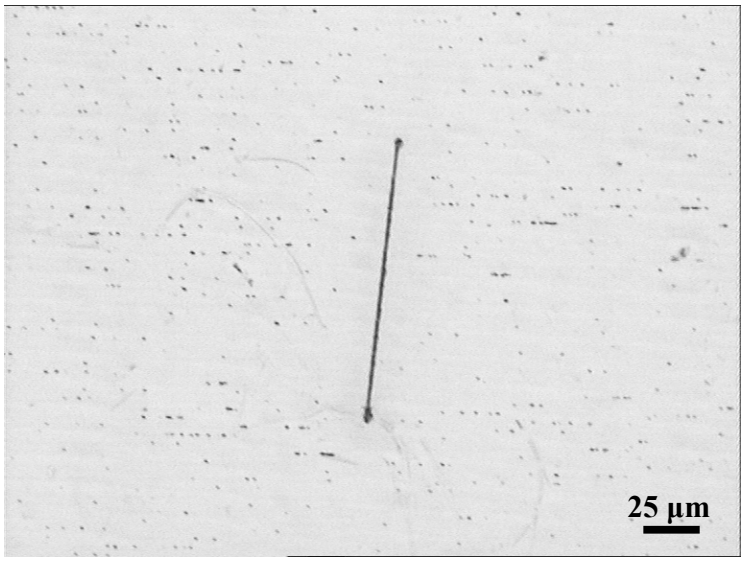

(b)

Figure 6.5 Optical microscope images of before (a) and after (b) 800 nm femtosecond laser cleaning of 1 μm glass particles on glass surface. The scratch line in the central is for marking.

the normal velocity component $v(r,t)$ in the excited SAW pulse can be described in a linear approximation by the expression (Kolomenskii, 1998)

$$v(r,t)=\frac{c_R}{4}\left(\frac{r_a^2}{2br}\right)^m \frac{r_a c_R t_0}{b^2}\frac{p_0}{\rho c_t^2}\Gamma\gamma\Phi_m\left(\frac{c_R t-r}{b}\right), \tag{6.2}$$

where the shape of the SAW is given by the function

$$\Phi_m(\xi)=\int_0^\infty k^{1+m}\exp\left(-\frac{k^2}{4}\right)\cos\left(k\xi+\frac{\pi m}{2}\right)dk\,, \tag{6.3}$$

and the characteristic wavelength of the SAW pulse is given by parameter

$$b=\sqrt{r_a^2+c_R^2 t_0^2}\,. \tag{6.4}$$

The exponent $m=0$ is used for a line shape source (near acoustic field), and $m=1/2$ for a point source. The dimensionless combination of the elastic constants in Eq. (6.2) is introduced

$$\gamma=\left[\left(1-c_R^2/c_l^2\right)/\left(1-c_R^2/c_t^2\right)\right]^{1/4}, \tag{6.5}$$

$$\Gamma=\left\{\left(c_t^2-c_R^2/2\right)\left[\left(c_t^2-c_R^2\right)^{-1}+\left(c_l^2-c_R^2\right)^{-1}\right]-2\right\}^{-1}, \tag{6.6}$$

where $c_{t,l,R}$ are the propagation velocities of the transverse, longitudinal, and Rayleigh waves. For different solids, the product $\Gamma\times\gamma$ ranges from 0.1 to 1. For the Si substrate, the typical values are $c_R=3.4\cdot10^5$ cm/s, $c_t/c_R=$ 1.10, $c_l/c_R=$ 1.59, thus $\Gamma\gamma$ = 0.74.

Kolomenskii estimated the SAW intensity for a line shape source with $m = 1/2$ and pulse pressure $p_0 = 10^8$ Pa. Normal velocity and acceleration for SAW with $r_0 = 7\,\mu m$ and $t_0 = 10\,ns$ are shown in Fig. 6.6 a, which are close to the results published by Kolomenskii.

For a line shape source, the SAW profiles (in the linear approximation) do not depend on the distance. Values of acceleration are sufficient to remove 0.4 μm Al_2O_3 particles from the Si substrate, in agreement with the experiment. Kolomenskii discussed the situation when SAW was created by a line focused laser pulse.

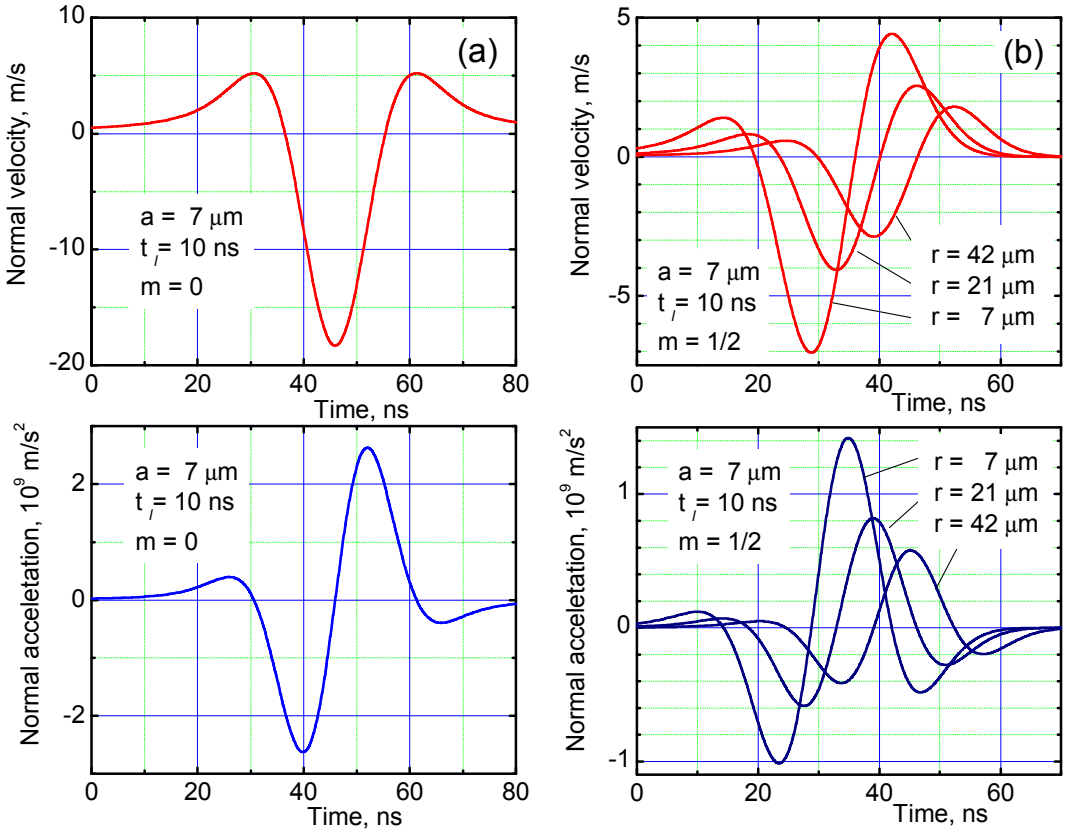

Figure 6.6. Normal velocity and acceleration for a line shape source (a) and for point source at different distances (b).

However if we discuss the point source, one can see from Eq. (6.2) the amplitude of SAW is reduced with distance as $1/\sqrt{r}$. It follows the total conservation of the energy flux. The flux density varies with distance as $\frac{1}{2\pi r}$. As the acoustic energy is proportional to v^2 it means that velocity (and acceleration) amplitudes vary as $1/\sqrt{r}$. These quantities are shown in Fig. 6.6(b) (other parameters are the same as in Fig. 6.6(a). One can see that for a distance bigger than 7 μm, acceleration amplitude is insufficient for the removal of the same particles. With point source, the SAW shape becomes asymmetrical. The amplitude of velocity for the leading edge is higher than that for the falling edge. However with higher value of p_0, one can consider the following situation when sufficiently intensive SAW is created by the neighboring particle.

We can roughly estimate the effect of convergent acoustic wave, replacing the pressure profile in Eq. (6.1) by

$$p(r,t) = p_1\left\{\exp\left[-\frac{r^2}{r_a^2}\right] - \exp\left[-\frac{r^2}{(r_a-\delta_r)^2}\right]\right\}\exp\left[-\frac{t^2}{t_0^2}\right], \tag{6.7}$$

where δ_r is the width of the ring. It does not practically change the pulse shape if $\delta_r << c_R t_0$ but the amplitude strongly depends on the position *r*, near the center where it can be sufficiently big, at least comparable with quasistatic thermal expansion.

To illustrate the basic effect, let us discuss distribution Eq. (6.7) with a narrow ring, $\delta_r << r_a$, and the same total energy as in Eq. (6.1), i.e. $p_1 \approx p_0 r_a / 2\delta_r$. Examples are shown in Fig. 6.7.

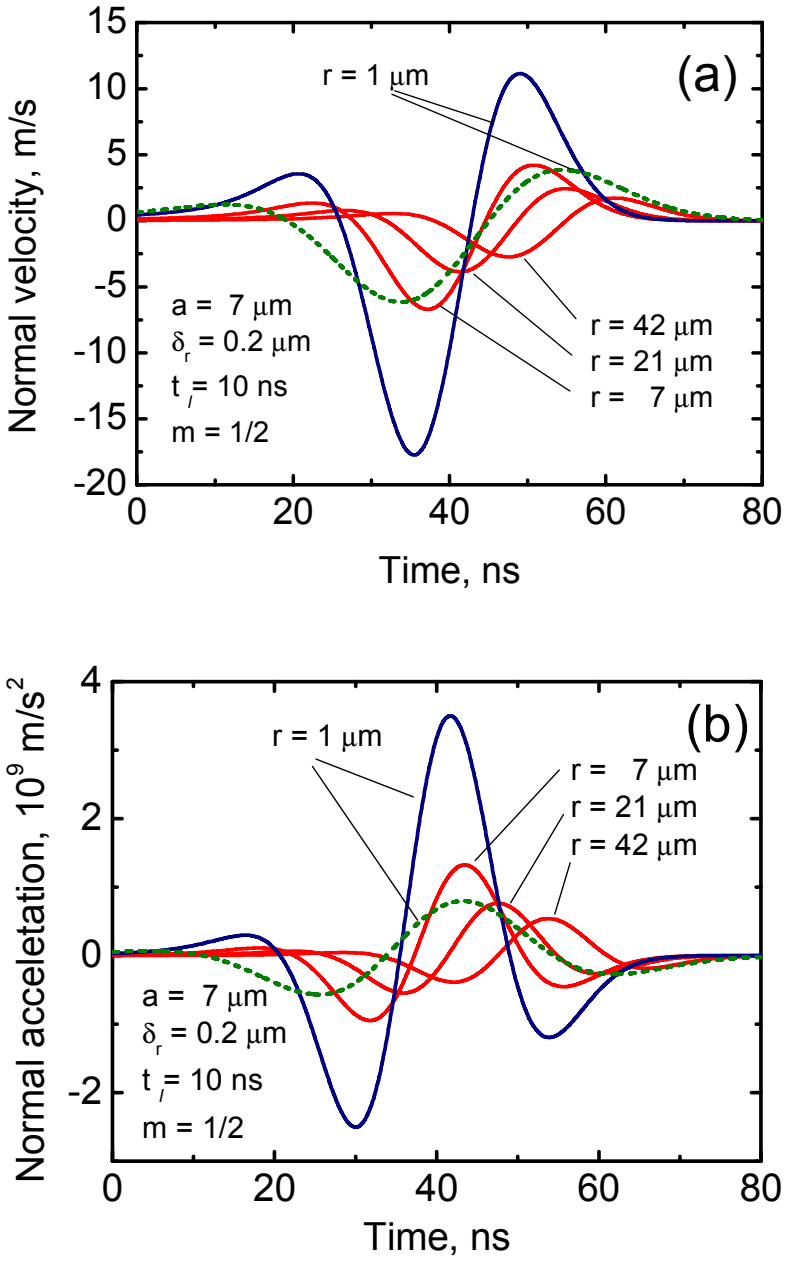

Figure 6.7. Normal velocity (a) and acceleration (b) for a ring-shape source with radius a = 7 μm and width δ_r = 0.2 μm. Dot lines present the acoustic wave which comes from the region of homogeneous heating. For this case $a = 42\,\mu\text{m}$ and $\delta_r = 41\,\mu\text{m}$. Total energy is the same as that in Fig. 6.6.

One can see that the divergence wave out of ring is practically the same as that in Fig. 6.6, while the convergent wave produces enhanced velocities and accelerations. Other acoustic waves can appear from the area of homogeneous heating out of the "shadow region". This case can also be estimated from the ring shape profile Eq. (6.7) if one puts $r_a >> c_R t_\ell$ and $\delta_r = r_a - r_{sh}$, where r_{sh} is the radius of the shadow region. Example of this pulse is also presented in Fig. 6.7.

Equation (6.2) was written for a particular case of the far field, thus we cannot apply this formula for small r values. It is clear from the energy conservation, that the limiting increase in the amplitude of acceleration under the particle can be estimated as $(ka)^{1/2}$, where $k = 2\pi/\lambda_R$ is the wave vector of Rayleigh wave. This estimation is applicable just for the "big ring" with $a >> c_R t_\ell$. In laser cleaning for the acoustic near-field, all characteristic sizes are smaller than $c_R t_\ell$. A careful examination of the near-field problem is beyond the scope of the present study. We just want to draw attention that in the near field region, the radius of the focal spot for a convergent wave can be significantly smaller than the wavelength of SAW, experimentally a focal spot size less than 1/14 of the wavelength was recorded (De Rosny & Fink, 2002). Thus one should expect that acoustic effects gave contribution for the particles with the size above $\approx c_R t_\ell / 15\pi$. For laser pulse of 23 ns, it means the size (diameter) is larger than 1.7 μm. It is also clear that acoustic effects are more pronounced for bigger particles.

6.3 Laser cleaning of sub-50nm Au particles

With dry laser cleaning thermal expansion of the particle (and/or substrate) produces particle acceleration, sufficient for particle removal [128]. However with smaller particles

one needs to produce a higher surface temperature for particle removal. It is illustrated in Fig. 6.8 which shows calculated surface temperature versus particle size [108, 111].

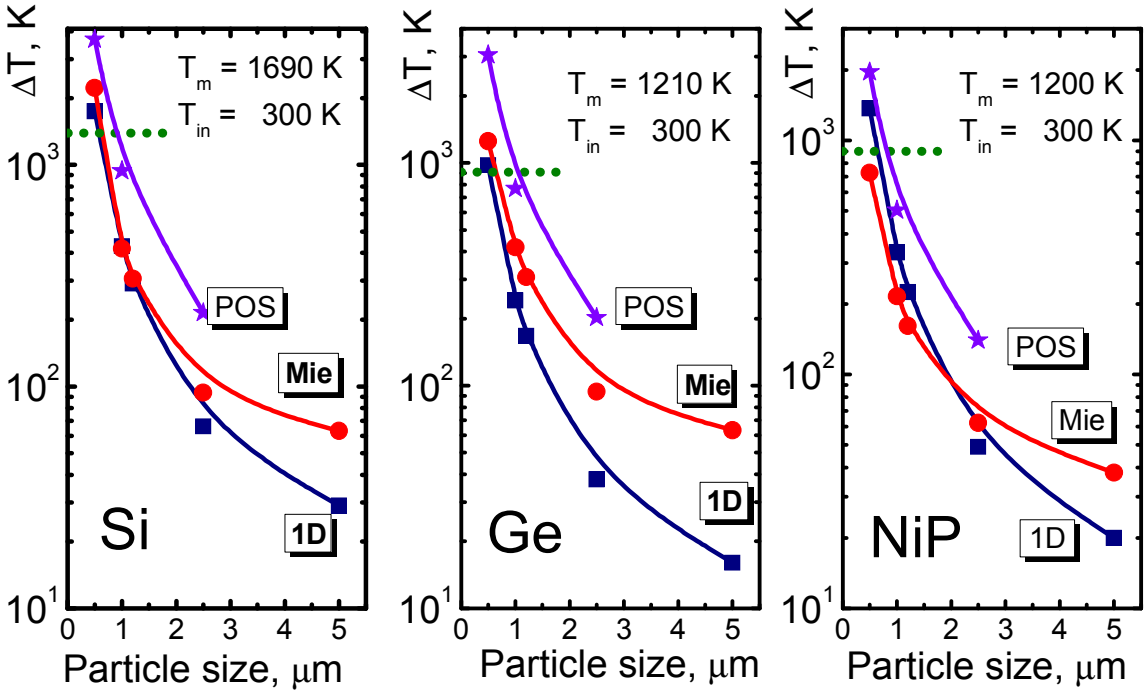

Figure 6.8. Maximal surface temperature at threshold fluences, calculated for excimer laser 248 nm, with pulse duration 23 ns. Removal of SiO_2 particles on Si, Ge and NiP substrates was investigated. Three curves in the pictures are calculated with different approximations. 1D curves present results of one-dimensional theory [129], which neglects variation of the intensity under the particle; Mie-curves show the result of calculations for the case, when near-field focusing effect is taken under the approximation of the Mie theory; POS-curves calculated on the basis of "particle on surface" theory, which takes into account the secondary scattering of radiation reflected from the surface of substrate [130, 86].

One can see that it is not possible to clean small transparent particles by dry cleaning method. The necessary temperature exceeds the melting and boiling temperatures, which leads to a change of removal mechanism; it becomes ablative cleaning [131,132]. One of the reasons for difficulties with small particles is related to small optical enhancement, for 100 nm particles enhancement is equal to one. Sub-50 nm transparent particle generally produces "shadowing effect" instead of enhancement effect under most kinds of laser irradiation.

However, one can think about significant field enhancement for metallic nanoparticles, using radiation, which excites localized surface plasmon [88]. Typical enhancement of the field in the vicinity of the particle varied from several to several tens times depending on the particle properties. There are three effects which one can expect in the discussed problems: 1) Absorption of the particle by itself may play an important role; 2) Intensity on the substrate surface can enhance substrate heating due to coupling of surface plasmon; 3) Pronounced angular effect of the radiation incidence may play an important role.

In Fig. 6.9(a), we show the extinction, scattering and absorption cross sections for Au particle of 20 nm radius sphere as a function of the wavelength λ. One can see plasmon resonance at $\lambda = 498$ nm. This resonance corresponds to dipole excitation that can be seen clearly from the field distribution in Fig. 6.9(b). The left peak at $\lambda = 207$ nm is also dipole Mie resonance but without the formation of localized plasmon, because of condition $\mathrm{Re}\,\varepsilon > 0$. For the case of particles with weak dissipation, one can see quadrupole and octopole plasmon resonances [122].

From Fig. 6.9(b), one can see that the highest field enhancement arises on the particle "equator", while for laser cleaning, one needs enhancement under the particle. The natural way to increase enhancement under the particle is the usage of incident radiation. To illustrate this effect, we performed calculations with particle on surface problem. The results of these calculations are shown in Fig. 6.10. One can see that the field enhancement under the particle with $\alpha = 45^{o}$ is about two times higher than that for $\alpha = 0^{o}$ due to a more efficient coupling.

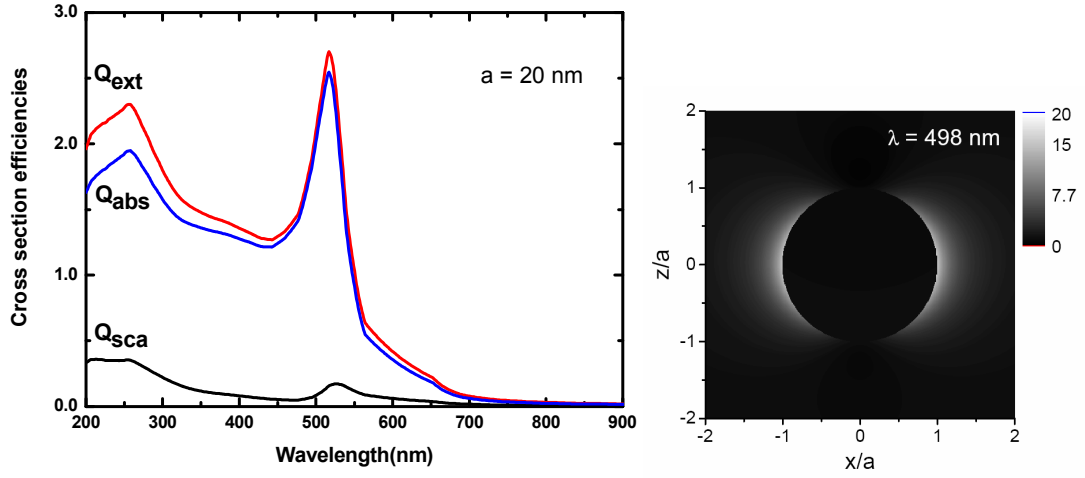

Figure 6.9. The extinction, scattering and absorption cross-sections for a gold particle of 20 nm radius sphere as a function of laser wavelength λ (a). The distributions of field $|E|^2$ around the Au particle at an exact dipole resonance with $\lambda = 498$ nm (b).

It was the basic idea to enhance the efficiency of laser cleaning with surface plasmon excitation and inclined laser radiation. We performed an experimental study of laser cleaning of sub-50 nm gold particles from Si substrate by 7 ns laser pulse of 532 nm radiation and found that these nanoparticles can be efficiently removed.

In the experiment, an n-type polished silicon wafer was used as the substrate. The sample was cleaned with acetone in an ultrasonic bath for 5 min. After that, the sample was rinsed with DI water and dried with N_2. The used suspension of 40 nm gold spherical particle with 5% size deviation. The particles were applied to Si surface by a small dispenser. The solvent was dried due to evaporation and consequently the self-assembled particles were left on the surface. Q-switched 2nd harmonic Nd:YAG laser (BMI industry Series 500) was used as the laser source. The wavelength was 532 nm with pulse duration of 7 ns. The laser spot size is about 6 mm. The repetition rate varies from 1 to 10 Hz. The output laser beam is linearly polarized.

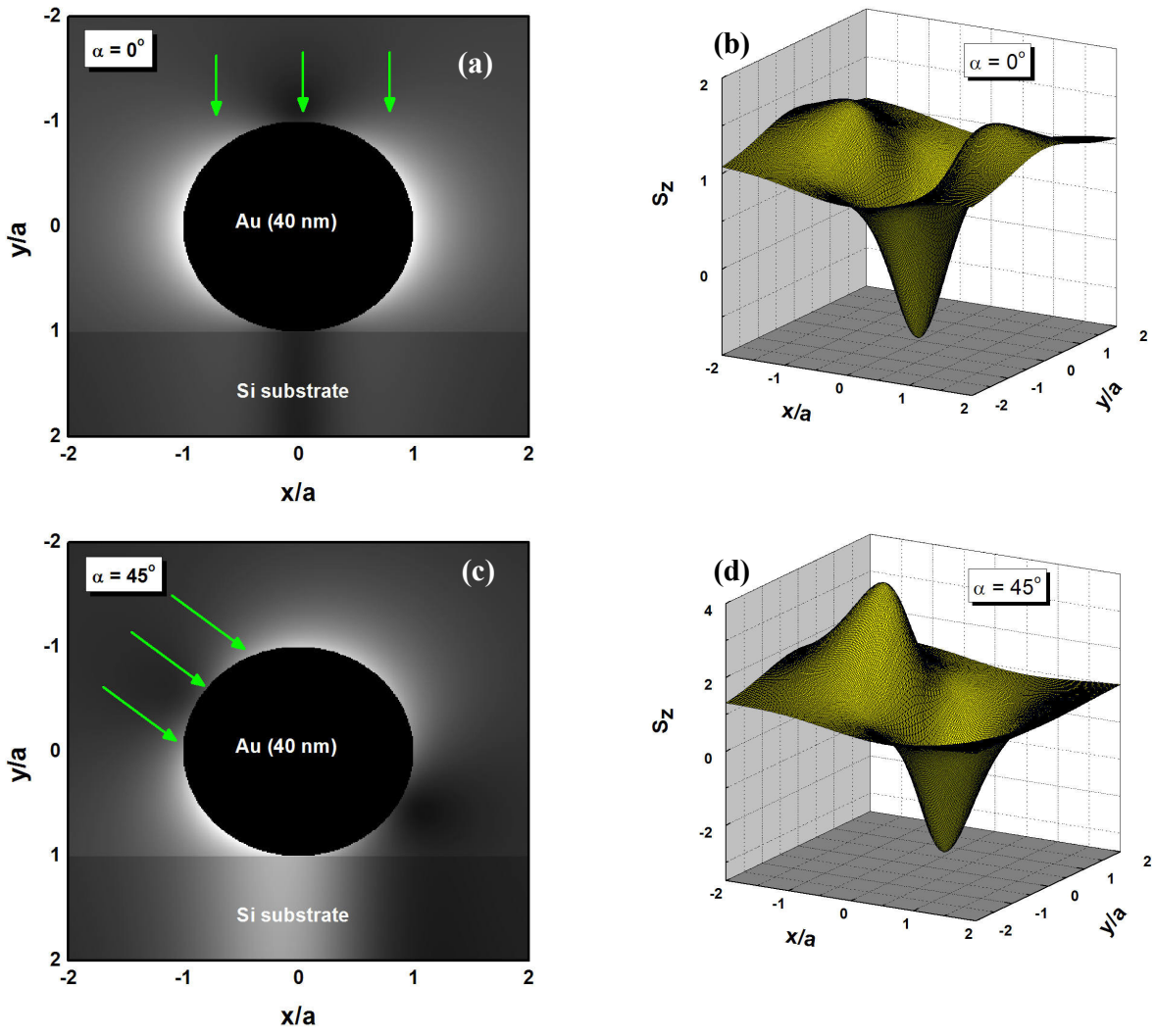

Figure 6.10. Contour plots for intensity distribution in *xz*-plane (a, c) and normalized intensity (z-component of the Poynting vector) under the 40-nm gold particle on n-Si surface (b, d) at different incidence angles: $\alpha = 0^{o}$ (a, b) and $\alpha = 45^{o}$ (c, d).

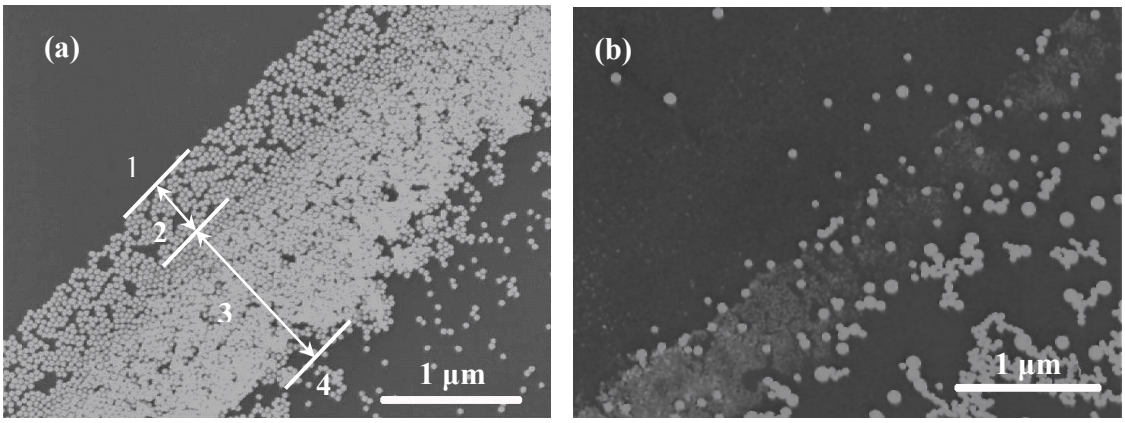

Figure 6.11. SEM images of 40 nm gold nanoparticles on the n-Si substrate surface before (a) and after (b) 300 pulses (532 nm, 7 ns) at a laser fluence of 50 mJ/cm^2 and an incidence angle of 45^o.

Figure 6.11 shows the SEM images of 40-nm gold nanoparticles left on the Si substrate surface before (a) and after (b) 300 laser pulses irradiation at a laser fluence of 50 mJ/cm^2 and an incident angle of 45^o. It can be seen from Fig. 6.11(a) that as-deposited mask of gold nanoparticles on Si surface has arranged in different forms: region 1 is free from the particles; in region 2 particles form monolayer, in region 3 particles form multi-layer and in region 4 one can see isolated particles.

After laser cleaning, one can see from Fig. 6.11(b) that the majority of gold nanoparticles were removed from the surface; the total cleaning efficiency was estimated to be 80% in this case. One part of removed particles from regions 2 and 3 was found to be re-deposited in regions 1 and 4. These re-deposited particles mainly stay in region 4 instead of region 1.

Gold particle is highly absorbing for radiation of 532 nm (Q_{abs} = 0.43). It means that

the free particle can be heated efficiently. The corresponding temperature rise can be estimated from the energy balance

$$T = \frac{3}{4}\frac{Q_{abs}\Phi}{c\rho a} \tag{6.8}$$

where Φ is the (homogeneous) laser fluence. For example for Φ = 50 mJ/cm^2 Eq. (6.8) yields a high temperature above 6000 K for a 40 nm (a = 20 nm) gold particle. Although this temperature cannot be reached for the particle on the surface due to heat conductivity of the substrate, it is clear that effects related to the direct heating of the particle may play an important role. Heating of the substrate arises due to radiation enhancement under the particle and due to thermal contact of the particle and substrate.

One can see another phenomenon from Fig. 6.11(b): the appearance of big gold nanoparticles after laser irradiation. The upper limit size of 200 nm (aggregated by 5 nanoparticles) nanoparticle has been observed in our experiment. As we mentioned above, it can be due to considerable heating of particles up to the melting temperature. Nanoparticles have a lower melting temperature as compared to the bulk material. The low melting temperature of nanoparticles is due to the large ratio of surface atoms to inner atoms, in which the surface energy of the surface atoms is reduced. The melting point of bulk gold is about 1064 °C while it is 600 – 800 °C for several tens nanometer size gold nanoparticles [133]. In experiments, it was found that multi-layer gold nanoparticles (particles in region 3) are more readily to be melted to form a bigger size nanoparticle than monolayer particles (particles in region 2).

Figure 6.12 presents the cleaning efficiency as a function of incidence angles for gold particles. As it can be seen, the cleaning efficiency increases smoothly with incidence angles. This tendency is quite different from that in laser cleaning of transparent particles on the surface, in which a steep decline of cleaning efficiency appears with increasing incidence angles [134]. Effective removal of metallic particles (Cu) by angular laser cleaning was previously discussed in [135]. However the authors demonstrated this effect for sufficiently big particles (diameter about 10 μm) and they suggested a different mechanism in efficiency increasing.

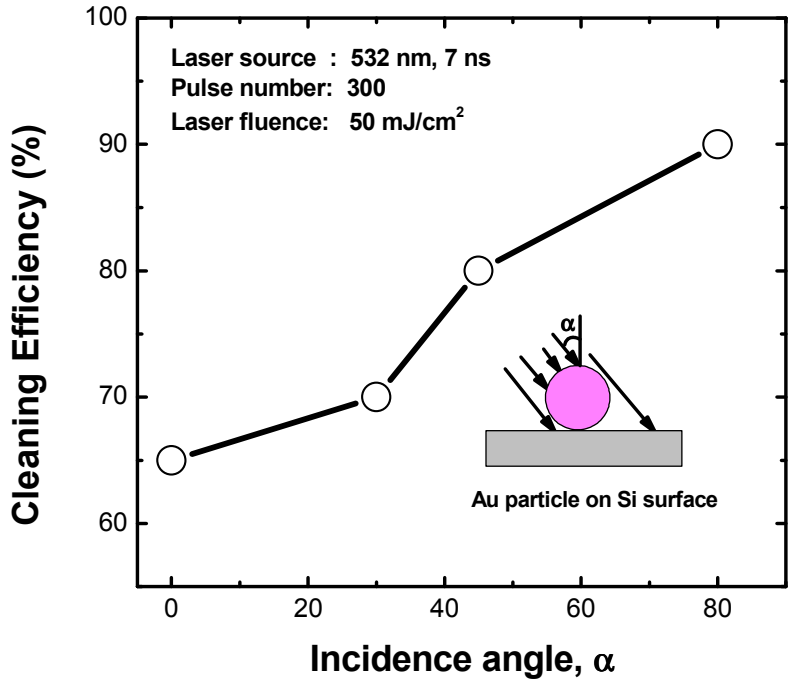

Figure 6.12. Cleaning efficiency as a function of incidence angle.

Chapter 7 Conclusions and future work

7.1 Conclusions

Optical near-field scattering by micro/nano-particles was studied in the thesis. The scattering by transparent silica microparticles and 40 nm Au nanoparticles was studied experimentally and theoretically. Numerical calculations based on Mie theory showed a good agreement with experiments. The conclusions can be summarized as follows:

1. Surface nanostructuring beyond optical diffraction limit is feasible by using : (1) nonlinear multi-photon absorption effect from femtosecond laser, and (2) optical near-field enhancement. Sub-wavelength (250 nm) nano-craters were created on the glass surface by 800 nm / 100 fs femtosecond laser irradiation of self-assembled 1 μm silica particles mask. No cracks were found at edges of produced nanostructures on the glass surface due to two-temperature non-equilibrium state. Nanobumps can also be fabricated on glass surface without cracks by single pulse femtosecond laser irradiation.
2. The difference of microparticles size significantly influences the nano-structure sizes through the near field enhancement. According to the theory, even 10% of size deviation for 1 μm diameter particles in the research would change enhancement from 10 to 15 and result in a broad range of nano-structure size on the substrate in the experiments.
3. At a low fluence, the feature sizes were found from 200 to 300 nm with the average depth of 150 nm. Tri-hole structure was novelly found when laser fluence

is higher than 43.8 J/cm^2 due to the polarized femtosecond laser irradiation. While more debris was formed at a high fluence.

4. Mie theory calculation shows that the focusing point will move outside of the particle by increasing the size. Experimentally using 6.84 μm particles, these particles are in their integrity that verifies that the position of focusing point depends on the particle size.
5. Besides normal laser irradiation, microparticles irradiated by oblique incident light show a dislocation that nano-dent does not locate in the center but around 1 μm off the center. Mie theory calculation proved that the under the particle, the "hot point" on glass surface had a displacement of 30% of particle radius, where this radius is 3.4 μm. It is a very good agreement between experiments and theory.
6. As for absorptive substrate, Si in the research, the threshold laser energy is significantly lower than that for glass substrate. Using 2.5 mW femtosecond laser power, similar nano-craters were found on Si surface. Then it can conclude that transparent microparticles can be used to generate ordered nano-craters. Through spherical micro-lens array, even bigger size spherical lens can be employed to fabricate sub-micron feature size structure on transparent materials.
7. Photoresist was utilized to record scattering patterns by self-assembly 40 nm Au particles under the irradiation of 325 nm laser. The propagation length of scattering wave by gold nanoparticle was found to be ~ 8 μm due to plasmonic effect.
8. The mechanism of Au nano-structures jumping off substrate surface was thought to be dewetting previously. While, Au nano-structures could jump both with

and without melting due to plasmonic enhanced absorption, which proves that melting by itself is insufficient for nano-structures removal. It is clear that plasmonic enhanced absorption also played an important role.

9. Calculations of the cross section efficiencies of 40 nm Au nanoparticles were verified experimentally. At the resonance frequency, 532 nm for Au, the absorption is the strongest as 2.5. Discussion about nondissipative nanoparticles shows that only a very small difference of particle size parameter changes the scattering from forward to backward.
10. In the dry laser cleaning process, near-field enhancement plays a major role. For transparent particle and normal incidence of radiation, the near-field focusing field near the centre produces a cylindrical convergent surface acoustic wave, which can enhance the particle removal for sufficiently "big" particles (above 2 μm).
11. The plasmonic effect permits to clean metallic nanoparticles by using laser at plasmonic resonance frequency. We demonstrated experimentally the ability to clean 40 nm gold particles from the Si substrate. For metallic nanoparticles, the laser intensity under the particle typically diminishes, in contrast to the transparent particle, which acts as a near-field lens. Nevertheless, using radiation frequencies near surface plasmon resonance, the conditions for the efficient coupling of radiation with metallic surface can be provided.

7.2 Future work

1. Non-contacting particle-mask for repeatable nanopatterning. A key drawback to

use the direct-contacting particle mask is that the mask can be only used for one time. A well-designed non-contacting mask could allow one to pattern substrate repeatedly. However, high resolution positioning and monitoring schemes should be developed.

2. Theoretical modelling of optical near-field for aggregated particles. For metal particles, the interaction between adjacent particles is a dominant effect.
3. Optical resonance and near-field effects of nanoshell spheres in which "sphere cavity resonance" (SCR) mode and "plasmon resonance" (PR) mode are both supported by the spheres. It is thus of great importance for nanoengineering in optical near field.
4. So far, the work is focused on femtosecond laser illumination of transparent particle and laser dry cleaning. To get sub-100 nm feature size patterns, nonlinear localised plasmonic has to be applied.

Bibliography

(1) E. D. Palik. Handbook of optical constants of solids, New York:Academic Press 1985.

(2) U. Kreibig, M. Vollmer. Optical Properties of Metal Clusters, Springer-Verlag, Berlin, Heidelberg. 1995.

(3) C. Girard and A. Dereux. Near-field optics theories, Rep. Prog. Phys., *59*, pp.657-699. 1996.

(4) C. F. Bohern, D. R. Huffman. Absorption and Scattering of Light by Small Particles. New York: Wiley. 1998.

(5) Diao J. J., Chen G. D., Xi C., Fan Z. Y., and Yuan J. S. Optical resonance of metal-coated nanoshell, Chin. Phys., *12* pp.100. 2003.

(6) Mie G. Beiträge zur Optik trüber Medien, speziell kolloidaler Metallösungen, Ann. Phys.(Leipzig), *25* pp.377-445. 1908.

(7) M. Kerker. The scattering of light and other electromagnetic radiation. New York: Academic Press. 1969.

(8) N. A. Logan. Survey of some early studies of the scattering of plane waves by a sphere. Proc. IEEE pp.773–785. 1965.

(9) M. Born and E. Wolf, Principles of optics, 7 ed., UK: Cambridge University Press. 1999.

(10) P.Chylek, J. T. Kiehl, and M.K.W.Ko. Optical levitation and partial-wave resonances, Phys. Rev. A, *18*, pp.2229. 1978.

(11) A. Ashkin and J. M. Dziedzic. Observation of optical resonances of dielectric spheres by light scattering, Appl. Opt., *20*, pp.1803. 1981.

(12) S. Kawata (ed). Near-field optics and Surface Plasmon Polaritions, 1 ed., Berlin, Heidelberg, New York: Springer-Verlag, 2001.

(13) N. N. Nedyalkov, H. Takada and M. Obara. Nanostructuring of silicon surface by femtosecond laser pulse mediated with enhanced near-field of gold nanoparticles, Appl. Phys. A, *85*, pp.163. 2006.

(14) Y. Lu and S. C. Chen. Nanopattering of silicon surface by near-field enhanced laser irradiation, Nanotechnology, *14*, pp.505. 2003.

(15) B. S. Luk'yanchuck, A. Blanco and V. Orofino. Physical Modeling of the interstellar Dust, Proc. SPIE, *4070*, pp.154. 2000.

(16) F. Burmeister, C. Schafle, B. Keilhofer, C. Bechinger, J. Boneberg and P. Leiderer. From Mesoscopic to Nanoscopic Surface Structures: Lithography with Colloid Monolayers, Advanced Materials, *10*, pp.495. 1998.

(17) H. M. Nussenzveig. Diffraction Effects in Semiclassical Scattering, Cambridge: Cambridge University Press. 1992.

(18) U. Ch. Fischer, D. W. Pohl. Observation of Single-Particle Plasmons by Near-Field Optical Microscopy, Phys. Rev. Lett., *62*, pp.458. 1989.

(19) W. Denk, D. W. Pohl. Near-field optics: Microscopy with nanometer-size fields, J. Vac. Sci. Tech. B, *9*, pp.510. 1991.

(20) P. Debye. Der Lichtdruck auf Kugeln von beliebigem Material, Ann. d. Physik., *335*, pp.57. 1909.

(21) T. J. I'A. Bromwich. The scattering of plane electric waves by a sphere, Phil. Trans. Roy. Soc., A, *220*, pp.175. 1920

(22) H. C. van de Hulst. Rech. Astron. Observ. Utrecht, XI, Pt.1. 1946.

(23) K. C. Toussaint, Jr., M. Liu, M. Pelton, J. Pesic, M. J. Guffey, P.Guyot-sionnest, and N. F. Schererer. Plasmon resonance based optical trapping of single and multiple Au nanoparticles, Optics Express, *15* pp.12017. 2007

(24) R. Ruppin. Surface modes and optical absorption of a small sphere above a substrate, Surf. Sci., *127*, pp.108. 1983

(25) O. B. Toon, T. P. Ackerman. Algorithms for the Calculation of Scattering by Stratified Spheres, Appl. Opt., *2*, pp.3657–3660. 1981.

(26) T. Kaiser, G. Schweiger. Stable algorithm for the computation of Mie coefficients for scattered and transmitted fields of a coated sphere, Comput. Phys., *7*, pp.682. 1993

(27) D. Bhanti, S. Manickavasagam, M. P. Menguc. Identification of nonhomogeneous spherical particles from their scattering matrix elements, J. Quant. Spectrosc. Radiat. Transfer, *56*, pp. 561–608. 1996.

(28) A. B. Evlyukhin, G. Brucoli, L. Martin-Moreno, S. I. Bozhevolnyi, and F. J. Garcia-Vidal. Surface plasmon polaiton scattering by finite size nanoparticles, Phys. Rev. B, *76*, 075426. 2007

(29) M. Kerker, D.-S. Wang, C. L. Giles. Electromagnetic scattering by magnetic spheres, J. Opt. Soc. Am., *73,* pp.765–767. 1983.

(30) R. W. Hart and E. W. Montroll. On the Scattering of Plane Waves by Soft Obstacles. I. Spherical Obstacles, J. Appl. Phys., *22*, pp.376. 1951

(31) E. W. Montroll and J. M. Greenberg. Scattering of Plane Waves by Soft Obstacles:

III. Scattering by Obstacles with Spherical and Circular Cylindrical Symmetry, Phys. Rev., *86*, pp.889. 1952

(32) C. J. Bouwkamp. Diffraction theory, Rep. Progr. Phys., *17*, pp.35-100. 1954

(33) R. Gans. Über die Form ultramikroskopischer Goldteilchen, Ann. d. Physik., *342*, pp.881. 1912

(34) F. Moglich, Ann. d. Physik., *342*, pp.609. 1927

(35) W. Seitz. Die Wirkung eines unendlich langen Metallzylinders auf Hertzsche Wellen, Ann. d. Physik.,*321*, pp.746. 1905

(36) W. V. Ignatowsky. Reflexion elektromagnetisches Wellen an einem Draht, Ann. d. Physik., *323*, pp.495. 1905

(37) R. J. Martin. Mie scattering formulae for non-spherical particles, J. Modern Opt. *40*, pp.2467–2494. 1993.

(38) D. K. Hahn, S. R. Aragon. Mie scattering from anisotropic thick spherical shells, J. Chem. Phys. *101*. pp.8409–8417. 1994.

(39) G. Jobst. Zur Farbentheorie kolloidaler Metallsuspensionen, Ann. d. Physik, *381*, pp.863. 1925

(40) H. C. van de Hulst. Rech. Astr. Observ. Utrecht, *11*, Part 2, pp.27. 1949

(41) O. J. F. Martin, Ch. Girard. Controlling and tuning strong optical field gradients at a local probe microscope tip apex, Appl. Phys. Lett., *70*, pp.705. 1997

(42) A. Madrazo, M. Nieto-Vespermas. Model near field calculations for optical data storage readout, Appl. Phys. Lett., *70*, pp.31. 1997

(43) J. S. Jaffe. A tomographic approach to inverse Mie particle characterization from

scattered light, Optics Express, *15*, pp.12217. 2007

(44) M. D. Barnes and V. K. La Mer. Monodispersed hydrophobic colloidal dispersions and light scattering properties, J. Col. Sci., *1*, pp.79. 1946.

(45) I. Johnson and V. K. La Mer. The determination of the particle. size of monodispersed systems by the scattering of light, J. Amer. Chem. Soc., 69, pp.1184. 1947

(46) J. C. Maxwell Garnett. Colours in metal glasses and metal films, Phil. Trans. Roy. Soc., A, *203*, pp.385-420. 1904

(47) T. Klaus, R. Joerger, E. Olsson, and C. G. Granqvist. Silver-based crystalline nanoparticles, microbially frabricated, Proc. Nat, Acad, Sci, USA, *9*6, pp.13611-13614, 1999.

(48) G. Peleg, A. Lweis, O. Bouevitch, L. Loew, D. Parnas, and M. Cinial. Gigantic optical non-linearities from nanoparticle-enhanced molecule probes with potential for selectively imaging the structure and physiology of nanometric regions in cellular system, Bioimaging, *4*, pp.215-224. 1996.

(49) C. P. Gibson. Systhesis and characterization of anisometric cobalt nanoclusters, Science, *267*, pp.1338-1340. 1995

(50) Y. K. Gunko, S. C. Pillai, and D. McInerney. Magnetic nanoparticles and nanoparticle assemblies from metallorganic precursors, J. Mater. Sci.—Mater. Electron, *12*, pp.229-302. 2001.

(51) M. Fleischmann et al., J. Raman Spectrosc. 4, 269 (1974)

(52) D. J. Jeanmaire, R. P. VanDuyne. Surface raman spectroelectrochemistry: Part I.

Heterocyclic, aromatic, and aliphatic amines adsorbed on the anodized silver electrode, J. Electroanal. Chem., *84*, pp.1. 1977

(53) J. Gersten. Electromagnetic theory of enhanced Raman scattering by molecules adsorbed on rough surfaces, J. Chem. Phys., *73*, pp.3023. 1980

(54) R. Ruppin. Electric field enhancement near a surface bump, Sol. State Commun., *39*, pp.903. 1981

(55) J. Gersten, A. Nitzan. Spectroscopic properties of molecules interacting with small dielectric particles, J. Chem. Phys., *75*, pp.1139. 1981

(56) D. van Labeke, Ph. Grossel, J. M. Vigoureux. Decay of. an excited molecule near small roughness, Proc. SPIE 1139, 73. 1989

(57) A. Leitner, M. E. Lippitsch, M. Riegler, F. R. Aussenegg, Adv. Phys. B, *36*, pp.105. 1995

(58) H. Ditlbacher, J. R. Krenn, G. Schider, A> Leitner, and F. R. Aussenegg. Two-dimensional optics with surface plasmon polaritons, Appl. Phys. Lett., *81*, pp.1762. 2002

(59) A. L. Stepanov, J. R. Krenn, H. Ditlbacher, A. Hohenau, A. Drezer, B. Steinberger, A. Leitner, and F. R. Aussenegg. Quantitative analysis of surface plasmon interaction with silver nanoparticles, Opt. Lett., *30*, pp.1524. 2005

(60) T. Sondergaard and S. I. Bozhevolnyi. Vectorial model for multiple scattering by surface nanoparticles via surface polariton-to-polariton interactions, Phys. Rev. B., *67*, 165405. 2003

(61) S. I. Bozhevolnyi, J. Erland, K. Leosson, P. M. W. Skovgaard, and J. M. Hvam.

Waveguiding in Surface Plasmon Polariton Band Gap Structures, Phys. Rev. Lett., *86*, pp.3008. 2001

(62) T. Sondergaard and S. I. Bozhevolnyi. Theoretical analysis of finite-size surface plasmon polariton band-gap structures, Phys. Rev. B., *71*, 125429. 2005

(63) A. –L. Baudrion, J. –C. Weeber, A. Dereux, G. Lecamp, P. Lalanne, and S. I. Bozhevolnyi. Influence of the filling factor on the spectral properties of plasmonic crystals, Phys. Rev. B., *74*, 125406. 2006

(64) M. C. Buncick, R. J. Warmak, T. L. Ferrell. Optical absorbance of silver ellipsoidal particles, J. Opt. Soc. Am. B, *4*, pp.927. 1987

(65) M. J. Bloemer, T. L. Ferrell, M. C. Buncick, R. J. Warmak. Optical properties of submicrometer-size silver needles, Phys. Rev. B., *37*, pp.8015. 1988

(66) T. Kume, S. Hayashi, K. Yamamoto. Light emission from surface plasmon polaritons mediated by metallic fine particles, Phys. Rev. B., *55*, pp.4774. 1997

(67) Betzig E, Trautman J K, Wolfe R, Gyorgy E M, Finn P L, Kryder M H and Change C H. Near-field magneto-optics and high density data storage, Appl. Phys. Lett. *61*, pp.142. 1992

(68) Watanabe O, Ikawa T, Hasegawa M, Tsuchimori M and Kawata. Nanofabrication induced by near-field exposure from a nanosecond laser pulse, Appl. Phys. Lett., *79*, pp.1366. 2001

(69) Piglmayer K, Denk R and Bauerle D. Laser-induced surface patterning by means of microspheres, Appl. Phys. Lett., *80,* pp. 4693. 2002

(70) Lu Y, Theppakuttai S and Chen S C. Marangoni effect in nanosphere-enhanced

laser nanopatterning of silicon, Appl. Phys. Lett., *82*, pp.4143. 2003

(71) W. Cai and R. Piestun. Patterning of silica microsphere monolyers with focused femtosecond laser pulses, Appl. Phys. Lett., 88, 111112. 2006

(72) S. Theppakuttai and S. Chen. Nanoscale surface modification of glass using a 1064 nm pulsed laser, Appl. Phys. Lett., *83*, pp.758. 2003

(73) S. Lewis, R. Wheeler-Jones, V. Haynes, and R. Perks. High density self assembled nanoparticle film with temperature-controllable interparticle spacing for deep sub-wavelength nanolithography using localized surface plasmon modes on planar silver nanoparticles tunable grating, Microelectron. Eng., doi:10.1016/j.mee.2007.09.005. 2007

(74) V. Santhanan, J. Liu, R. Agarwal, and R. P. Andres. Self-Assembly of Uniform Monolayer Arrays of Nanoparticles, Langmuir, *19*, pp.7881. 2003

(75) C. M. Zhou and D. Gall. Surface patterning by nanosphere lithography for layer growth with ordered pores, Thin Solid Films, doi:10.1016/j.tsf.2007.05.069. 2007

(76) K. Piglmayer, R. Denk, and D. Bauerle. Laser-induced surface patterning by means of microspheres, Appl. Phys. Lett., *80*, pp.4693. 2002.

(77) G. Langer, D. Brodoceanu, and D. Bauerle. Femtosecond laser fabrication of apertures on two-dimensional microlens arrays, Appl. Phys. Lett., *89*, 261104. 2006.

(78) A. Pikulin, N. Bityurin, G. Langer, D. Brodoceanu and D. Bauerle. Hexagonal structures on metal-coated two-dimensional microlens arrays, Appl. Phys. Lett., *91*,191106. 2007

(79) S. Calixto, V. P. Minkovich, and I. T. Gomez. Microlenses in the end of capillary tubes and their application to photonic crystal fibers, Applied Optics, *45*, pp.6463. 2006.

(80) C. S. Lim, M. H. Hong, Y. Lin, Q. Xie, A. S. Kumar, M. Rahman and S. Z. Lee. Microlens arrays fabrication by laser interference lithography for super resolution Surface nanopatterning, Appl. Phys. Lett., *89*, 191125. 2006.

(81) R. Ruppin, Surf. Sci. 58, 530 (1976)

(82) P. Royer, J. P. Goudonnet, R. J. Warmack, T. L. Ferrell. Substrate effects on surface-plasmon spectra in metal-island films, Phys. Rev. B., *35*, pp.3753. 1987

(83) J. A. Stratton. Electromagnetic Theory. New York: McGraw-Hill. 1941.

(84) C. J. Bouwkamp and H. B. G. Casimir. On multipole expansions in the theory of electromagnetic radiation, Physica, *20*, pp.539. 1954.

(85) K. Schwarzschild, Munch. Akad., Math-phys. Kl., 31 (1901), 293

(86) Luk`yanchuk B S, Zheng Y W and Lu Y F. Laser cleaning of solid surface: optical resonance and near-field effects, Proc. SPIE. 4065, 576. 2000

(87) Kik P G, Maier S A and Atwater H A. Plasmon printing - a new approach to near-field lithography, Mat. Res.Soc.Symp.Proc, *705*, pp.Y3.6. 2002

(88) Zayats AV and Smolyaninov I I. Near-field photonics: surface plasmon polaritons and localized surface plasmons, J. Opt. A: Pure Appl. Opt. *4*, pp.S16. 2003

(89) C. F. Bohren. How can a particle absorb more than the light incident on it?, Am. J. Phys., *51*, pp.323-327. 1983.

(90) V. M. Agranovich and V. L. Ginzburg. Crystal Optics with Spatial Dispersion,

and Excitons, Berlin: Springer. 1984.

(91) R. S. Decca, H. D. Drew, and K. L. Empson. Investigation of the electric-field distribution at the subwavelength aperture of a near-field scanning optical microscope, Appl. Phys. Lett., *70*, pp.1932-1934. 1997.

(92) S. Davy and M. Spajer, Near field optics: Snapshot of the field emitted by a nanosource using a photosensitive polymer, Appl. Phys. Lett., *69*, pp.3306-3308. 1996.

(93) H.-J. Munzer, M. Mosbacher, M. Bertsch, O. Dubbers, F. Burmeister, A. Pack, R. Wannemacher, B.-U. Runger, D. Bauerle, J. Boneberg, and P. Leiderer, Proc. SPIE, *4426*, pp.180. 2001.

(94) R. Micheletto, H. Fukuda, and M. Ohtsu. A Simple Method for the Production of a Two-Dimensional, Ordered Array of Small Latex Particles, Langmuir, *11*, pp.3333-3336. 1995.

(95) S. Rakers, L. F. Chi, and H. Fuchs. Influence of the Evaporation Rate on the Packing Order of Polydisperse Latex Monofilms, Langmuir, *13*, pp. 7121-7124. 1997.

(96) Z. B. Wang, M. H. Hong, Y. F. Lu, D. J. Wu, B. Lan, and T. C. Chong. Femtosecond laser ablation of polytetrafluoroethylene(Teflon) in ambient air, J. Appl. Phys., 93, pp.6375-6380. 2003.

(97) R. A. Bowling, Particles on Surfaces 1, pp.129, New York: Plenum Press, 1988.

(98) A. C. Tam, W. P. Leung, W. Zapka, and W. Ziemlich. Laser-Cleaning Techniques for Removal of Surface Particulates, J. Appl. Phys., 71, pp.3515-3523. 1992.

(99) Y. Kanemitsu and Y. Tanaka. Mechanism of crack formation in glass after high-power laser pulse irradiation, J. Appl. Phys., *62*, pp.1208. 1987.

(100) S. M. Huang, Z. Sun and B. S. Luk'yanchuk. Nanobump arrays fabricated by laser irradiation of polystyrene particle layers on silicon, Appl. Phys. Lett., *86*, 161911. 2005.

(101) Mosbacher M, Munzer H J, Zimmermman J, Solis J, Boneberg J and Oeiderer P. Optical field enhancement effects in laser-assisted particle removal, Appl. Phys.A., *72*, pp.41. 2001

(102) X. Liu, D. Du and G. Mourou, IEEE J. Quant. Electron. *33*, pp.1706. 1997.

(103) S. I. Anisimov and B. S. Luk`yanchuk. Selected problems of laser ablation theory, Physics - Uspekhi, *45*, pp.293. 2002.

(104) K. Piglmayer, R. Denk and D. Bäuerle. Laser-induced surface patterning by means of microspheres, Appl. Phys. Lett., *80*, pp.4693. 2002.

(105) S. Singh and L. T. Bradley. Three-Photon Absorption in Napthalene Crystals by Laser Excitation, Phys. Rev. Lett, *12,* pp.612. 1964

(106) L. Dhar, J. A. Rogers, and K. A. Nelson. Time-resolved vibrational spectroscopy in the impulsive limit, Chemical Reviews, *94*, pp.157-193. 1994.

(107) K. H. Davis, K. Miura, N. Sugimoto, and K. Hirao. Writing waveguides in glass with a femtosecond laser, Opt. Lett., *21*, pp.1729. 1996.

(108) B. S. Luk`yanchuk, N. Arnold, S. M. Huang, Z. B. Wang, M. H. Hong. Three-dimensional effects in dry laser cleaning, Appl. Phys. A, *77*, pp.209. 2003.

(109) H. Blumer. Strahlungsdiagramme kleiner dielectrischer Kugeln. II, Z. Phys., *38*,

pp.304-328. 1926

(110) M. A. Schirmann, Ann. d. Physik, *364*, pp.493. 1919

(111) B. S. Luk`yanchuk, Z. B. Wang, W. D. Song, M. H. Hong. Particle on surface: 3D-effects in dry laser cleaning, Appl. Phys. A, *79*, pp.747. 2004

(112) Z. B. Wang, M. H. Hong, B. S. Luk'yanchuk, Y. Lin, O. F. Wang and T. C. Chong. Angle effect in laser nanopatterning with particle-mask, J. Appl. Phys., *96*, pp.6845. 2004.

(113) B. S. Luk'yanchuk, Y. W. Zheng, and Y. F. Lu. Laser cleaning of solid surface: Optical resonance and near-field effects, Proc. SPIE, *4065*, pp.576-587. 2000.

(114) P. A. Bobbert, J. Vlieger, and R.Greef. Light reflection from a substrate sparsely seeded with spheres - comparison with an ellipsometric experiment, Physica, A, *137*, pp.243-257. 1986.

(115) P. A. Bobbert and J. Vlieger, Light scattering by a sphere on a substrate, Physica, A, *137*, pp.209-242. 1986

(116) G. L. Wojcik, D. K. Vaughan, and L. K. Galbraith. Lasers in Microlithography, Proc. SPIE, 777, pp.21. 1987.

(117) M. I. Mishenko, J. W. Hovenier, and L. D. Travis. Light Scattering by Nonspherical Particles, San Diego: Academic Press, 2000.

(118) A. Habenicht, M. Olapinski, F. Burmeister, P. Leiderer and J. Boneberg. Jumping Nanodroplets, Science, *309*, pp.2043. 2005.

(119) R. Fuchs, K. L. Kliewer. J. Opt. Soc. Am., 58, 319. 1968

(120) M. I. Tribelsky, Sov. Phys. JETP, 59, 534. 1984

(121) M. I. Tribelsky, B. S. Luk'yanchuk. Anomalous Light Scattering by Small Particles, Phys. Rev. Lett., *97*, 263902. 2006

(122) B.S. Luk'yanchuk, M. I. Tribelsky. Anomalous Light Scattering by Small Particles and inverse hierarchy of optical resonances. In: Collection of papers devoted to memory of Prof M. N. Libenson, P.101 (St. –Petersburg Union of the Scientists Russia. 2005.

(123) E. D. Palik. Handbook of optical constants of solids, New York:Academic Press 1985.

(124) U. Kreibig, M. Vollmer. Optical Properties of Metal Clusters, Springer-Verlag, Berlin, Heidelberg. 1995.

(125) L. H. Lee (ed). Fundamentals of Adhesion, New York: Plenum Press. 1990.

(126) R. A. Bowling, Particles on Surfaces 1, pp.129, New York: Plenum Press, 1988.

(127) L. J. Frink and F. V. Swol. A molecular theory for surface forces adhesion measurements, J. Chem. Phys., *106*, pp.3782. 1997.

(128) D. Bäuerle, Laser Processing and Chemistry, 3^{d} ed., Berlin:Springer. 2000.

(129) N. Arnold, In: Laser Cleaning, Ed. by B. S. Luk`yanchuk. World Scientific, New Jersey, London, Singapore, Hong Kong, pp. 51-102. 2002

(130) P. A. Bobbert, J. Vlieger. Light scattering by a sphere on a substrate, Physica A, *137*, pp.209. 1986.

(131) H.-J. Münzer, M. Mosbacher, M. Bertsch, O. Dubbers, F. Burmeister, A. Pack, R. Wannemacher, B.-U. Runge, D. Bäuerle, J. Boneberg, P. Leiderer, Proc. SPIE, *4426*, pp.180. 2002.

(132) N. Arnold, G. Schrems, D. Bäuerle, Appl. Phys. A 79, 729 (2004).

(133) P. Buffat, J. P. Borel. Size effect on the melting temperature of gold particles, Phys. Rev. A, *13*, pp.2287. 1975

(134) Y. W. Zheng, B. S. Luk'yanchuk, Y. F. Lu, W. D. Song, Z. H. Mai. Dry laser cleaning of particles from solid substrates: Experiments and theory, J. Appl. Phys., *90*, pp.2135. 2001.

(135) J. M. Lee, K. G. Watkins, W. M. Steen. Angular laser cleaning for effective removal of particles. from a solid surface, Appl. Phys. A, *71*, pp.671. 2000.

List of Publication

Journal papers:

(1) Y. Zhou, M. H. Hong, J. Y. H. Fuh, L. Lu, B. S. Luk'yanchuk, Z. B. Wang, L. P. Shi and T. C. Chong, Direct femtosecond laser nanopatterning of glass substrate by particle-assisted near-field enhancement, *Appl. Phys. Lett.*, **88** 023110. 2006

(2) Y. Zhou, M. H. Hong, J. Y. H Fuh, L. Lu, B. S. Lukyanchuk, C. S. Lim, and Z. B. Wang, Nanopatterning mask fabrication by femtosecond laser irradiation, *Journal of Materials Processing Technology*, **192**, pp.212-217. 2007

(3) Zhou Yi, Hong Ming-Hui, Fuh Ying-Hsi Jerry, Lu Li, Tan Leng Seow and Luk`yanchuk Boris, Light irradiation through small particles and its applications for surface nanostructuring in near field, *Chinese Phys. Lett.*, **24** (10), pp.2947-2950. 2007

(4) Y Zhou, M H Hong, J Y H Fuh, L. Lu , and B S Lukiyanchuk, Evanescent wave interference lithography for surface nanostructuring, *Phys. Scr.,* **T129**, pp.35-37. 2007

(5) Zhou Yi, Hong Minghui, Fuh Ying Hsi, Lu Li , Boris Lukyanchuk and Wang Zengbo, Near-field enhanced femtosecond laser nano-drilling of glass substrate, *J. Alloys and Compounds*, **449**, pp.246-249. 2008

(6) B. S. Luk`yanchuk, M. I. Tribelsky, Z. B. Wang, Y. Zhou, M. H. Hong, L. P. Shi, and T. C. Chong, Extraordinary scattering diagram for nanoparticles near plasmon resonance frequencies, *Applied Physics A*, **89**, pp.259-264. 2007

Conference proceeding:

(7) Y. Zhou, M. H. Hong, J. Y. H. Fuh and L. Lu, Particle lens nanolithography: from micro transparent particles to nano metal particle, *International Symposium on Nano Science and Technology*, Tainan, Taiwan, 9-10 November, 2006. pp.105-110

(8) Wang Zengbo, Boris Lukyanchuk, Zhou Yi , Hong Minghui and Song Wendong, Plasmonic effect in laser cleaning of small metal particles in sub-50 nm size region, *The 1st International Symposium on Functional Materials* , Kuala Lumpur Malaysia, December, 2005. pp.422-428

(9) D.K.T.Ng, M.H.Hong, L.S.Tan, Y. Zhou and G.X.Chen, Nanopatterning of gallium nitride nanowires grown by pulsed laser ablation, *The 1st International Symposium on Functional Materials ,* Kuala Lumpur Malaysia, December, 2005. pp.429-434

(10) C. H. Liu, M. H. Hong, Y. Zhou, G. X. Chen and A. T. S. Hor, Formation and characterization of Ag deposited TiO2 nanoparticles by laser ablation, *2nd International Symposium on Function Materials*, 16-19 May, 2007, Hangzhou, China. pp.87

(11) B. Luk`yanchuk, M. Tribelsky, Z. B. Wang, Y. Zhou, M. H. Hong, L. P. Shi and T. C. Chong, Propagating and localized plasmons in weakly dissipating materials, *9th Conference on Laser Ablation,* Tenerife, Spain, 24 – 28 September, 2007, pp.26

(12) Z.Q. Huang, M.H Hong, Y. Zhou, L.P. Shi adn T. C. Chong, $CuSO_4$ ASSISTED LASER ETCHING OF GLASS SUBSTRATE WITH 1064 nm LASER IRRADIATION，*9th Conference on Laser Ablation,* Tenerife, Spain,

24 – 28 September, 2007， pp.31

Book Chapter

(13) B. S. Luk`yanchuk, Z. B. Wang, Y. Zhou, M. H. Hong, W. D. Song and T. C. Chong, Particle on surface: about possible acoustic and plasmonics effects in dry laser cleaning, in "*Laser Cleaning II*", Ed. D. M. Kane, World Scientific, New Jersey, London, Singapore, Hong Kong, pp.79-113. 2006.